Nikbakhtnasrabadi, Fatemeh (2022) *Antenna sensing for wearable applications.* PhD thesis.

http://theses.gla.ac.uk/83010/

Antenna Sensing for Wearable Applications

Fatemeh Nikbakhtnasrabadi

A thesis submitted in fulfilment for the degree of
Doctor of Philosophy

James Watt School of Engineering
University of Glasgow

January 2022

Abstract

As wearable technologies are growing fast, there is emerging trend to increase functionality of the devices. Antennas which are primarily component in communication systems can offer attractive route forward to minimize the number of components functioning as a sensing element for wearable and flexible electronics. Toward development of flexible antenna as sensing element, this thesis investigates the development of the flexible and printed sensing NFC RFID tag. In this approach, the sensor measurement is supported by the internal sensor and analog-to-digital convertor (ADC) of the NFC transponder. Design optimisation, fabrication and characterization of the printed antenna are described. Besides, the printed antenna, NFC transponder and two simple resistive sensors are integrated to form a fully flexible sensing RFID tag demonstrating applicability in food and health monitoring.

This thesis also presents development of two antenna sensors by using functional materials: (i) An inductor-capacitor (LC) resonant tank based wireless pressure sensor on electrospun Poly-L-lactide (PLLA) nanofibers-based substrate. The screen-printed resonant tank (resonant frequency of ~13.56 MHz) consists of a planar inductor connected in parallel with an interdigitated capacitor. Since the substrates is piezoelectric, the capacitance of the interdigitated capacitor varies in response to the applied pressure. To demonstrate a potential application of developed pressure sensor, it was integrated on a compression bandage to monitor sub-bandage pressure. (ii) To investigate the realization of sensing antenna as temperature sensor simple loop antenna is designed and in this study unlike the first study that the sensing element was the substrate, the conductive body of the antenna itself is considered as a functional material. In this case, a small part of a loop antenna which originally was printed using silver paste is replaced by Poly(3,4-ethylenedioxythiophene): polystyrene (PEDOT: PSS). The sensing mechanism is based on the resonant frequency shift by varying temperature.

While using functional materials is useful for realization of antenna sensor, another approach also is presented by developing stretchable textile-based microstrip antennas on deformable substrate which can measure joint angles of a human limb. The EM characteristics of the meshed patch antenna were compared with its metallic counterpart fabricated with lithography technique. Moreover, the concept of stretchable UHF RFID-based strain sensor is touched in the final part of this thesis.

Acknowledgements

First, I would like to express my sincere gratitude to my supervisor Prof. Ravinder Dahiya for his continues support throughout this journey. Also, I would like to acknowledge European Union's INTERREG VA Programme (H2020- Intereg-IVA5055) for their financial support.

Furthermore, I would also like to thank all members of Bendable Electronics and Sensing Technologies group. Special thanks to Dr Hatem El Matbouly, Dr Pablo Escobedo, Dr Mitradip Bhattacharjee, who have provided valuable contribution to this research. A great thanks to Dr Ensieh Hosseini, Dr Martina Aurora Costa Angeli, Dr Moupali Chakraborty, Dr Saoirse Dervin, Markellos Ntagios, and Dr Dhayalan Shakthivel for their contribution to shape this research. Thanks to Dr Afesomeh Ofiare for helping me with antenna characterization in the anechoic chamber.

Further, I would like to thank the James Watt Nanofabrication Centre (JWNC) and electronic workshop staffs for all the trainings and support.

I would like to thank my friend Dr Houra Haghpanahan for her advice and encouragement during last four years.

Finally, I would like to thank my parents for their love and support throughout my life. Special thanks to my husband, Jafar, for his amazing support. Without his support, I would have stopped this study at early stage.

Author's Declaration

I hereby declare that this thesis was composed and originated entirely by myself in the School of Engineering at The University of Glasgow except where explicitly stated otherwise in the text, and that this work has not been submitted for any other degree or professional qualifications.

Fatemeh Nikbakhtnasrabadi

Abbreviation and Acronym

WSN	wireless sensor networks
BSN	body sensor networks
RFID	Radiofrequency Identification
SRR	split ring resonator
PVA	polyvinyl alcohol
PEDOT: PSS	poly-3,4-ethylene-dioxythiophene
PVC	polyvinyl chloride
IC	integrated circuit
UHF	ultrahigh frequency
NFC	near field communication
RSSI	received signal strength indicator
EM	electromagnetic
ISO	International Organization for Standardization
PDMS	Polydimethylsiloxane
PI	polyimide
DoD	drop-on-demand
UWB	ultra-wide band
IoT	Internet of Things
SMT	surface-mount technology
VQFN	Very thin Quad-Flat No-leads
ADC	analog-to-digital converter
SFE	Sensor Front End
PLLA	Poly l-lactic acid
IDC	interdigitated capacitive
PPC	parallel plate capacitors

SEM	scanning electron microscope
VSWR	Voltage Standing Wave Ratio
VNA	vector network analyser
TPU	Thermoplastic polyurethane
HB	Harmonic-Balance

Publications

Journal Articles

1- **Nikbakhtnasrabadi, F.,** El Matbouly, H., Ntagios, M. and Dahiya, R., 2021. “Textile-Based Stretchable Microstrip Antenna with Intrinsic Strain Sensing.” *ACS Applied Electronic Materials*, *3*(5), pp.2233-2246. DOI: 10.1021/acsaelm.1c00179.

2- **Nikbakhtnasrabadi, F.,** S. Hosseini, E., Dervin S., Shakthivel D. and Dahiya R., “Smart Bandage with Inductor-Capacitor Resonant Tank based Printed Wireless Pressure Sensor on Electrospun Poly-L-lactide nanofibers.” *Advanced Electronic Materials,* 2101348, 2022. DOI: 10.1002/aelm.202101348.

3- Bhattacharjee, M., **Nikbakhtnasrabadi F.** and Dahiya R. “Printed Chipless Antenna as Flexible Temperature Sensor”. *IEEE Internet of Things Journal*, vol. 8, no. 6, pp. 5101-5110, 2021. DOI: 10.1109/JIOT.2021.3051467.

4- Escobedo, P., Bhattacharjee M., **Nikbakhtnasrabadi, F.** and R. Dahiya. "Flexible Strain and Temperature Sensing NFC Tag for Smart Food Packaging Applications." *IEEE Sensors Journal*, vol. 21, no. 23, pp. 26406-26414, 2021. DOI: 10.1109/JSEN.2021.3100876.

5- Escobedo, P., Bhattacharjee, M., **Nikbakhtnasrabadi, F.,** and Dahiya, R. Smart “Bandage with Wireless Strain and Temperature Sensors and Battery-less NFC Tag.” *IEEE Internet of Things Journal*, vol. 8, no. 6, pp. 5093-5100, 2021. DOI: 10.1109/JIOT.2020.3048282.

6- **Nikbakhtnasrabadi, F.*,** Chakraborty, M.*, and Dahiya, R. “Hybrid Integration of Screen-Printed RFID Tags and Rigid Microchip on Paper.” *IEEE Journal on Flexible Electronics*, 2022. DOI: 10.1109/JFLEX.2022.3165515.

Journal Articles under preparation

7- **Nikbakhtnasrabadi, F.,** Panunzio N., Marrocco G., and Dahiya, R. Antenna Sensor: Smart Materials, Mechanisms and Applications

Book Chapter

El Matbouly, H., **Nikbakhtnasrabadi, F.,** and Dahiya, R. RFID Near-Field Communication (NFC)-based sensing technology in food quality control (*In press- Springer Nature*)

Conference Proceedings

1- **Nikbakhtnasrabadi, F.,** Hosseini, E. S., & Dahiya, R. (2021, June). Flexible Strain Sensor based on Printed LC Tank on Electrospun Piezoelectric Nanofibers. In *2021 IEEE International Conference on Flexible and Printable Sensors and Systems (FLEPS)* (pp. 1-4). IEEE.

2- Bhattacharjee, M., **Nikbakhtnasrabadi, F.,** & Dahiya, R. (2021). Chipless Sensing Antenna and an NFC Smart-Tag for Temperature Measurement. In *2021 XXXIIIrd General Assembly and Scientific Symposium of the International Union of Radio Science* (pp. 1-4). IEEE.

3- Bhattacharjee, M., Escobedo, P., **Nikbakhtnasrabadi, F.,** & Dahiya, R. (2020, August). Printed Flexible Temperature Sensor with NFC Interface. In *2020 IEEE International Conference on Flexible and Printable Sensors and Systems (FLEPS)* (pp. 1-4). IEEE.

4- Escobedo, P., Bhattacharjee, M., **Nikbakhtnasrabadi, F.,** & Dahiya, R. (2020, August). Flexible strain sensor with NFC tag for food packaging. In *2020 IEEE International Conference on Flexible and Printable Sensors and Systems (FLEPS)* (pp. 1-4). IEEE.

5- Bhattacharjee, M., Escobedo, P., **Nikbakhtnasrabadi, F.,** & Dahiya, R. (2020). NFC based Polymer Strain Sensor for Smart Packaging. In *2020 XXXIIIrd General Assembly and Scientific Symposium of the International Union of Radio Science* (pp. 1-4). IEEE.

Conference Proceedings (not related to this thesis)

6- Angeli, M. A. C., **Nikbakhtnasrabadi, F.,** Vena, P., & Dahiya, R. (2019, July). Geometry dependent application of stretchable printed antenna. In *2019 IEEE International Conference on Flexible and Printable Sensors and Systems (FLEPS)* (pp. 1-3). IEEE.

7- Manjakkal, L., **Nikbakhtnasrabadi, F**., & Dahiya, R. (2018, October). Energy Autonomous Sensors for Water Quality Monitoring. In *2018 IEEE SENSORS* (pp. 1-4). IEEE.

Table of Contents

List of Figures

List of Tables

Chapter 1. Introduction

1.1 Background and motivation

With the advancement in flexible electronics over the last few years, the growing demand for wearable systems has been on the rise (1-3). The wearables consist of electronic devices and components worn on the surface of the skin or clothing for detecting, analysing, and transmitting information related to the body signals or its ambient (4). Wearable technology has a variety of applications including health care, epidermal electronics, entertainment, and the fashion industry. Besides, some of these wireless sensors also find application in humanoid robotics and human-machine interactions such as prosthetic limbs to make robots more intelligent (5). Moreover, the demand to add more functionalities on the same flexible substrate is increasing (6-8). The combination of multiple environmental sensors in one single node offers monitoring of multiple parameters at the same time, hence, increasing the node functionality (9-12). The integration of wireless interfaces with these sensors allows to be in line with the internet of things (IoT) concept for wireless sensor networks (WSNs) (13). This allows remotely to access, monitor, and control many flexible devices through smartphones, tablets, or laptops (14, 15).

The use of multiple sensor nodes for various monitoring imposes the requirement of huge wiring between various electronic components that may lead to interferences between parallel signals as well as time delays. Moreover, a slight wire connection failure in some parts of the device may disturb the sensor output signal. Therefore, in a system with a huge number of nodes, accurate sensing data is only obtained at the cost of additional complexity (16).

One solution to reduce this complexity for flexible electronics is to use the properties of a wireless electromagnetic component as a sensor in combination with a sensitive/functional material. By doing so, part of the electronic circuitry will not be needed as their function is transferred to the transmitter/receiver unit. This will transfer the processing of the sensing information to the transmitter/receiver instead of loading the flexible sensor node with electronic circuitry for processing the sensed information. The more functionalities are transferred out of the flexible sensor node, the simpler the wearable device becomes.

The recent innovations in engineered functional materials have paved the way of flexible electronics for wearable electronic devices which are lightweight, portable, less expensive, and environment friendly (17). With this advancement, the addition of wireless telecommunication of a wearable device was necessary. These advances have allowed connecting different type of sensors to the cyberspace for applications such as environment monitoring, wearable systems for health monitoring, and security (18). The overall expectation of a multi sensor system is that several types of sensors are used in a single sensor node for monitoring various parameters, for instance in human activity monitoring parameters such as sweat (19), temperature (20), heart rate (21), respiratory rate (22), and motion (23) to be monitored simultaneously for health or sport applications. Besides, in robotic/humanoid applications, multi sensors are very favorable for various environmental monitoring, sensory for strain (24), pH (25), radiation (26), and volatile organic compounds (27) to be installed on one robot for multipurpose sensing activities.

The current wireless sensing nodes suffer from power consumption due to the electronic circuity and circuits interfaces, in addition to complexity of interconnectivity and circuit integration due to the incorporation of different sensors and materials. Moreover, most of materials used in the current wireless sensing node are rigid which are not conformable to human body and they need to be replaced by using flexible and stretchable materials suitable for on-body applications.

However, the implementation of such broad picture of multi-sensory nodes comes at a price of increasing the complexity of the sensing node electronics. This complexity generates various problems that challenge such implementation. First, as the number of sensors connected to a single node increases the interconnections become difficult and complex resulting in signal delays or failures. The reason for this is due to the parasitic capacitances generated from the multi-layers metal wires that affect the time constant of the whole circuit. Moreover, increasing the metal interconnections will increase the need to have multiple electrical contacts which will increase the contact resistance and hence, the dissipation. The device failure can happen easily due to the complexity of interconnections, for instance, shaking or hitting the multi-sensor node will result a vibration that may break the connections or even re-establish an undesirable electrical contact. Second, the problem of sensor integration will arise due to different circuitry requirement of each sensor. Finally, the power consumption of the multi sensor node will increase as the number of components. This is true even if the sensor itself is passive, the reason is that the output of each sensor is processed by an active electronic circuit which consumes energy that increases with the number of sensors. When transferring the physical stimuli into a measurable signal, sensors convert energy from one form to another form. Sensor can be distinguished based on what kind of energy it detects or transfers to the system. Since a multi-sensor nodes can be built with different type of sensors, and different types of sensors consume various amount of energy. Some of them require a significant large amount of energy than others. For example, gas sensor requires a comparatively higher amount of energy than temperature, pressure or image sensor because it requires active heating elements (28). Image sensors also require a high amount of energy because thousands of conversions (analog to digital) are required for producing images (29).

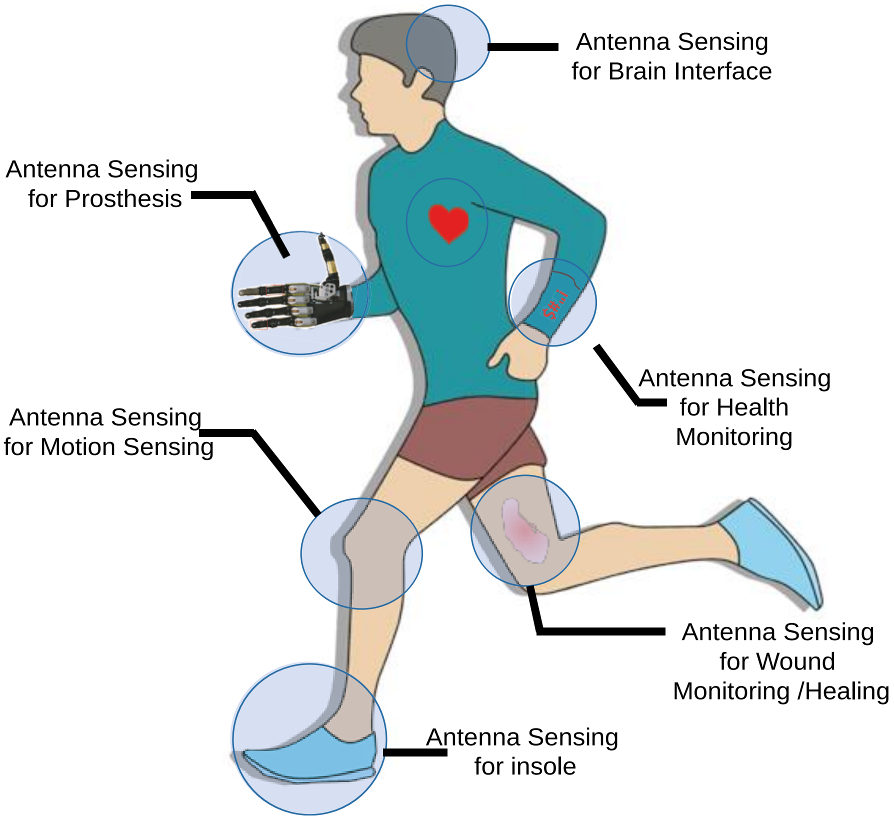

Figure 1-1 Conceptual illustration of using wireless sensors (antenna sensor) to monitor parameter of interest in wearable applications. Adopted from (30)

From the aforementioned problems associated with multi-sensor nodes, an emerging solution based on using the antenna as a sensing element in addition to its role as radiating element for telecommunications is attractive. **Figure 1-1** demonstrates the general concept of using antenna sensor to monitor parameter of interest in wearable applications. Expectations for the flexible electronics market is projected to reach 40.37 billion in revenue by 2023 (31). This multi electronics and wireless technologies integration with wearable electronics also open a new horizon of bendable/flexible devices for new application. In **Figure 1-2**, by comparing the number of publications for wearable sensors to the wearable antennas one can see that the interest in wearable antennas raised around 2011. This increase of the popularity of the wearable sensor through multisensory node has led the path to the antenna sensor as a solution to the issues arising from the demand of the wearable applications to integrate more and more sensors. From this comparison, one can project the increase in antenna sensors research in the coming years as an emerging solution for the challenges facing multi-sensory wearables. This thesis presents some approaches to design antenna as sensor in response to this demand.

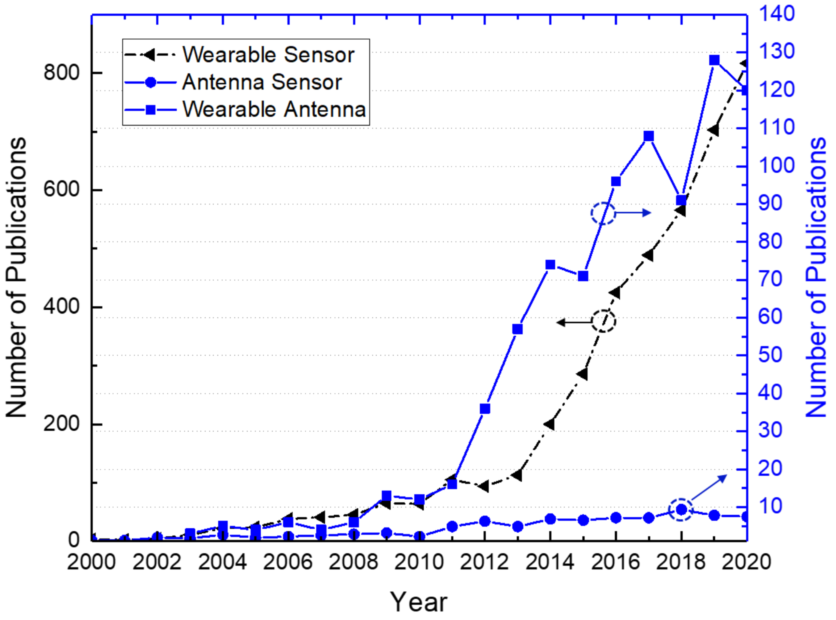

Figure 1-2 The total number of publications in the areas of wearable sensors, wearable antenna and antenna sensors in the last 20 years. Source: Web of Science, November 2021. “wearable sensor”, “wearable antenna” and “antenna sensor” were searched to conduct the comparison. (arrows denote respective y-axis).

1.2 Structure of the thesis

The organisation and content of the thesis are as follows:

Chapter 2 presents the extensive review on various mechanisms to exploit antennas as sensing elements. Besides, approaches to add sensing capabilities to RFID tags is covered. The classification and principle of operation for RFIDs also is presented trying to address challenges and opportunities in designing an antenna with flexible/stretchable materials. Besides, fabrication techniques compatible to fabricate flexible antenna sensors is covered.

Chapter 3 presents development of printed NFC based sensing tag, using the capability of commercially available NFC RFID chip to integrate external sensors. The design, characterization and fabrication of the flexible NFC tag is covered in this chapter. The designed loop antennas with various dimensions are screen-printed on paper substrate. The antenna with higher quality factor is chosen to be used in antenna sensor integration. The NFC sensor transponder which includes ADC provides the sensor reading. To demonstrate sensing capability of the tag, a thermistor was connected to the relevant pins and temperature reading was performed using the Texas Instruments firmware for the RF430FRL152H ISO/IEC 15693 sensor transponder. Two approaches were perused to demonstrate the capability of the developed system for wound and food monitoring applications.

Chapter 4 presents development of two types of antenna sensor by exploiting functional materials. In the first subsection, the design, fabrication and characterization of an inductor-capacitor resonant tank is discussed. The properties of electrospun Poly-L-lactide (PLLA) nanofibers (biocompatibility and sensitivity to pressure as this is a piezoelectric material) used as functional/sensing element is explored. The LC tank-based sensor is integrated on a compression bandage to demonstrate its potential use in the monitoring of sub-bandage pressure. In the second study, a loop antenna as a temperature sensor is designed. Unlike the first study which sensing element was the substrate, the conductive body of the antenna itself has been considered as a functional material. In this regard, a small portion of a loop antenna which originally was printed using sliver paste was replaced using conductive polymer, PEDOT: PSS. The sensing mechanism was based on study the resonant frequency of the antenna in response to temperature changes.

Chapter 5 describes development of textile-based stretchable microstrip patch with intrinsic strain sensing. Design, fabrication, characterization and potential application of the developed antenna is covered. The idea of modifying a commercial UHF RFID using the stretchable textile is examined briefly in this chapter as well.

Chapter 6 summaries the key outcome of the research work and provides future directions to take the current work forward. The major key findings of the thesis and limitations of each approach are presented in this chapter.

Chapter 2. Literature Review

This chapter reviews the concept and various mechanisms for using flexible antennas as sensing transducing element. It covers various conductive materials, the substrates and applications. Different fabrication techniques adopted to realize flexible antennas are also presented. Besides, it briefly discusses the classification and method of operation of RFID technologies.

In wireless communication, the sensor node is responsible of sending the sensed data back to the reader through the antenna after receiving a request signal from the reader for the sensed parameter. To use the antenna as a sensing element, one has to know that the design of an antenna for any wireless application depends on the environment, transmission power, and frequency range (32). Moreover, the performance of the antenna depends on the material used, the type of fabrication technique employed, and the substrate properties (33). For a flexible antenna to function as a sensor, various transducing mechanisms can be implemented to enable the antenna to react the external environmental stimuli. The following section discusses the applicable mechanisms for antenna as a sensing component.

2.1 Transducing mechanisms for antennas as a smart sensing element

The main function of an antenna in a communication system is to transmit and receive the electromagnetic radiation. Since communication systems are operated in microwave spectrum, antennas are designed for microwave communication which span the frequency range of 100 MHz to 100 GHz corresponding to waves lengths between 3 m to 3 mm (34). In addition to its transmission/reception of a signal, sensing capability can be added to the antenna itself provided that a compatible method of transduction does exist. This allows the antenna to change its properties due to the external physical stimuli and communicate it as a measurable quantity at the same time. For an antenna, the main property is its resonance frequency and one way to allow antenna sensing is by the frequency shift approach which maps the influence of an external stimuli in a resonator (35).

In general, the antenna structure is a metal on a dielectric substrate and introducing materials with intrinsic sensing properties can lead to variation of dielectric constant or magnetic permeability due the external stimuli. These functional/sensitive materials can either be the dielectric substrate as well as conductive materials serve as metal body of the antenna. One principle which is important is that the functional material should be dedicated to one parameter. For instance, using two functional materials on one antenna for transducing two stimuli will have selectivity problem. Moreover, sensitive material that has material properties (ε and μ) which vary due to more than one stimulus will cause the same problem of selectivity.

Another possibility is to take advantages of change of the size or the form of the flexible/stretchable antenna due to external deformable stimuli. In addition, another sensing mechanism can be added which does not involve material perturbation. This mechanism involves the modification of the input impedance of the antenna by the external stimuli which requires connecting the antenna to a sensitive input load and by varying its impedance the transduction is achieved through the variation of the antenna's radiated power (36). The sensitive impedance does not have to be connected directly to the antenna input, instead it can be connected to a delay line which in turn is connected to the antenna input (37). In this case the detection of external stimuli can be linked to the phase of the signal instead of the frequency shift.

For component-based transduction, one of the common type of loads for antennas is the RFID chip which modify the backscattered power level of the signal for data transmission. This happens by the variation of the input impedance of the RFID chip which impacts the reflection coefficient (Γ) and hence the backscattered power (38). Other loads can be attached to the input of the antenna which have an impedance which is sensitive to a stimulus, and indirectly the variation of input impedance (Z_a) will lead to a reflection coefficient variation. reflection coefficient is defined as:

$$\Gamma = \frac{Z_a - Z_0}{Z_a + Z_0} \qquad (2\text{-}1)$$

where Z_0 is characteristic impedance of the transmission line which is chosen as 50 Ω and Z_a is input impedance of the antenna.

2.1.1 Antenna sensing using material with intrinsic sensing capabilities

An antenna sensor can be realized either by the addition of a dielectric sensitive material on a standard antenna or by introducing a sensitive material to the main body of antenna (i.e. the metal trace) (see **Figure 2-1**). The choice of the sensitive dielectric material depends on the selected quantity to be sensed (humidity, temperature, gas, etc.) (39). The substrate can use different materials such as carbon nanotubes for gas sensing or polymer for humidity sensing or a textile material such as denim for blood glucose sensing (40-42). Variation in the effective dielectric constant (relative permittivity) of the antenna sensor transduces the physical stimuli into a resonance frequency shift. Some commercial substrates can have a sensitive dielectric constant where the sensitivity is reported in the data sheet (43). In this case antenna sensor can be realized directly on the sensitive commercial substrate without the need of the addition of sensitive material, however, this type of antenna sensor will have limited sensing application since these commercial substrates do not provide a wide range of stimuli. For example, flexible antenna sensors using sensitive commercial flexible substrates is limited to mainly humidity and temperature sensing due to the extreme limitation of commercial sensitive substrates (44, 45). This makes the option of sensitive material functionalization is a plausible solution for having a wide variety of smart flexible antenna sensors. As describes in (46) a small portion of the loop antenna can be replaced with a PEDOT:PSS to create simple antenna as temperature sensor. The effect of humidity was minimum as the antenna was coated with very thin layer of Nitrocellulose lacquer.

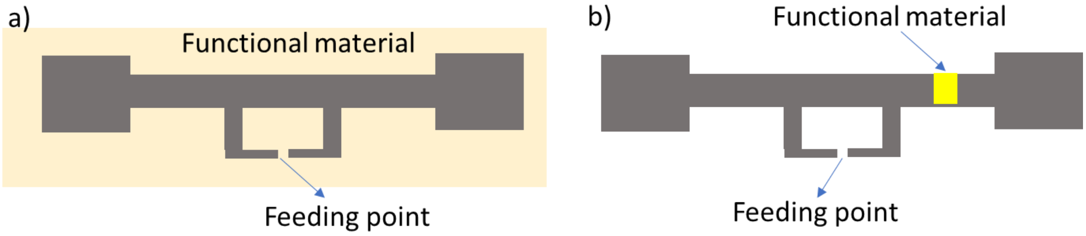

Figure 2-1 Schematic illustration of using functional/sensitive material to alter electromagnetic properties of an antenna. The sensing parameter can be Γ (S_{11}) of the sensor antenna. a) illustrates that sensing material can be a substrate for the antenna which is sensitive to temperature, moisture, etc. b) Sensing material can be loaded on the body of the antenna.

Dielectric perturbation as a sensing transduction mechanism can happen without the addition of the sensitive dielectric material. In this case, the antenna sensor can be realized on a non-sensitive dielectric substrate, and by placing the antenna sensor on different dielectric materials and the effective dielectric constant of the combination of the antenna substrate and the dielectric surface will change leading to a variation of the resonance frequency of the antenna. As an example, dielectric constant characterisation can be possible using a split ring resonator (SRR) structure on a non-sensitive dielectric substrate with dielectric constant ε_1, as shown in **Figure 2-2**. The SRR loop represents the inductance (L_{SRR}) and the gap represents the capacitance (C_{SRR}). The resonant frequency of the SRR is defined by

$$f_r = \frac{1}{2\pi\sqrt{L_{SRR}C_{SRR}}} \qquad (2\text{-}2)$$

This gives the resonance signature in the frequency spectrum which is represented by the black curve. When the structure is placed on another dielectric with a different dielectric constant of ε_2, a dielectric perturbation occurs due to the combination of the two dielectric materials resulting in a new dielectric constant which is a combination of ε_1 and ε_2. These mixed dielectrics alter the resonance frequency to a new value which is presented in **Figure 2-2** by the red curve.

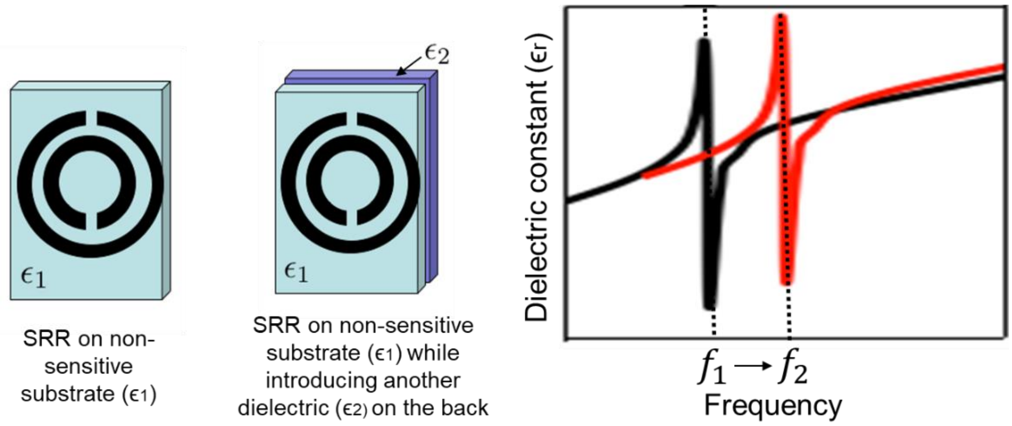

Figure 2-2 The dielectric perturbation of an SRR structure on a non-sensitive substrate by the addition of an external dielectric surface with different dielectric constant.

Since an antenna sensor needs to be able to detect its surrounding without a sensor device, it is required in some occasions the addition of a sensitive material either to improve the sensitivity of the antenna towards a physical parameter or to make the antenna itself sensitive. Functional materials are often used relating to the RFID tags or a metasurfaces for wireless sensing applications. These materials exhibit large and sharp physical and/or chemical changes to external environmental stimuli, such as humidity, pressure, temperature, gas, and electric fields, and hence are suitable for sensing applications. In chapter 4 two types of antenna sensors developed based on this mechanism are presented.

Various smart/functional materials that exhibit a noticeable response against a temperature, relative humidity, pH, etc. are summarized below, each can be used in antenna sensors using intrinsic sensing capabilities of these materials. Since the antenna is made of metal layer on a dielectric substrate then for compatibility with the antenna structure the functional material need to be of the same nature. Semiconductor materials such as indium tin oxide (ITO), silver flakes, and silver nanoparticles, conducting polymers such as poly-3,4-ethylene-dioxythiophene (PEDOT:PSS) (47), polyaniline (PANI) (48), and dielectric materials such as Kapton, polyvinyl chloride (PVC) (49), and polyvinyl alcohol (PVA) (50) can be introduced as sensing materials that change responses of antennas under the influence of varying physical parameters when integrated in RF sensing applications. In the following, a discussion on the properties of each material and the suitability for flexible antenna sensing applications is explained.

2.1.1.1 Smart sensing material for temperature

Phenanthrene: The dielectric constant of this material increases drastically after its transition temperature. This effect is not reversible and hence this dielectric material can be used as a transducing material for temperature threshold antenna sensing. This irreversibility can be used in antenna trigger applications where at the transition temperature the antenna works as an actuator for certain temperature value in real-time monitoring. In addition, the irreversibility of the temperature sensed value serves as a memory to the temperature threshold value attained (51, 52).

Ionic Plastic Crystal: This material exhibits an impedance variation due to temperature. The conductivity at each temperature is measured for temperatures ranging from −10 to +80 ∘C showing an electrical conductivity increase with increasing temperature within the temperature range. Contrary to phenanthrene this material has reversible temperature dependency and can be used to monitor real-time temperatures within −10 to +80 ∘C. Antenna temperature sensing can be achieved using this material by antenna input impedance transduction which is reflected in the reflection coefficient of transmitted (53).

Nanostructured Metal Oxide: Metal oxides are wide band gap materials that have been investigated for sensing applications. For instance, indium tin oxide (ITO) and zinc oxide (ZnO) are metal oxide materials which are sensitive to external environmental changes, such as pressure, temperature, and electric field. Results suggest that ZnO thin film is an excellent sensing material for temperature sensing and has a high melting point (2248 K) and good thermal stability which is essential for robustness in sensing applications for real environments conditions (54-57).

2.1.1.2 Smart sensing material for humidity

Polyamide: This polyamide is a hydrophobic organic material. It has a linear dielectric response while it absorbs water as the weight is proportional to relative humidity (RH). Polyamide film has a relative permittivity of 3.25 at 25% humidity and a room temperature of 23 ∘C and increases linearly with RH which can be used a capacitive humidity transducing material (58-60). This property suggest that Polyamide can be introduced as a dielectric humidity sensitive layer for antenna where the humidity is transduced by dielectric variation of Polyamide into resonance frequency shift. Moreover, Polyamide film is a flexible, low loss, and durable Polyimide film dielectric for flexible smart antenna sensing (61).

Polyvinyl Alcohol (PVA): The dielectric behaviour shows that as the PVA concentration in water increases the real part of permittivity ε_r' decreases at any frequency (0.2–20 GHz). On the other hand, at high frequency (>5 GHz) the imaginary ε_r'' increases with the increase in water content (62, 63). This shows that the PVA has twofold electric properties due humidity. With humidity change, PVA shows both dielectric and conductive sensitivities.

2.1.1.3 Smart sensing material for pH

A number of polymer materials exhibit sensitivity to pH variation among which organic conducting polymers have conductivity variation as a function of pH. The advantage of these conducting polymer is their process ability. However, the drawback is their instability toward environmental influences and the difficulty to achieve device-level performance. On the other hand, PEDOT which is conductive polymer shows robustness for practical applications (46). The conductivity of PEDOT depends on the pH level, with the highest conductivities at low pH, but the change is not dramatic except for pH value exceeding 11 (64). The conductivity variation of PEDOT is reversible over a wide pH range. Since pH is usually measured in aqueous medium, a special design arrangement needs to be taken in consideration when pH sensitive material is used in antenna sensing because radio frequencies do not propagate in liquids.

2.1.1.4 Smart sensing material for gases

Different nanostructures and organic materials exhibit sensitivity to certain gases. For instance, the electrical response of single- and multi walled carbon nanotube (CNT) films varies in the presence of ammonia gas (65), (66). In addition, carbon nanotubes and polymethylmethacrylate were incorporated in copolymer thin films to develop a wireless sensor for hazardous biological materials and vapours. The advantage of SW-CNTs is that they can be incorporated in porous flexible material such as paper creating an active sensing layer with a paper thickness (67). Integrating these types of active nanomaterials into a flexible porous matrix opens up opportunities for flexible antenna sensors.

Other nanomaterials for sensing have been investigated. Nanostructure metal oxides showed sensitivity toward different gases, for example, a hydrogen gas sensor based on zinc oxide (ZnO) nanorods has been reported in (68, 69). Moreover, carbon dioxide, oxygen, and ammonia gas sensors based on carbon nanotube–silicon dioxide composites are presented. Other metal oxides such as titanium oxide TiO2 showed (70) sensitivity towards ethylene gas which can be readout capacitively by integrating TiO2 in a capacitive RF sensor.

2.1.1.5 Smart sensing material for mechanical properties

Piezoelectric materials as substrates could offer new capability to measure the dynamic pressure to monitor the biological signals (71, 72). In relation with wearable systems, the piezoelectric polymers such as Polyvinylidene fluoride (PDVF) and Poly l-lactic acid (PLLA) are attractive due to their high chemical stability, flexibility, and biocompatibility. In fact, PLLA has an advantage for pressure sensing as unlike PVDF it does not exhibit pyroelectricity and hence there is no interference due to temperature variation. Further, the biodegradability of PLLA makes it attractive for both in vitro and in vivo implantable applications (73). Considering such attractive features in the section (4.1) we have used PLLA nanofibers-based substrate to develop LC (Inductor-Capacitor) resonant tank. In this work, an interdigitated capacitive (IDC) sensor is developed on electrospun PLLA nanofibers-based substrate and connected in parallel with a planar inductor forming a LC circuit to realise wireless pressure sensor. The LC circuits is designed to resonate at about 13.56 MHz. The PLLA nanofibers-based substrate used here, to realise the IDC capacitive sensors, offers better conformal contact with the skin and improves sensitivity under the pressure due to its piezoelectric property. It provides a direct interaction between the sensing elements and environment (74). Moreover, due to the uni-polarization of PLLA nanofibers during electrospinning, change in the permittivity of the dielectric layer is expected in response to applied pressure, which allows linear responses of capacitive response over a wide range of 0-16 kPa. This pressure range is of the same order as one used in commercial bandages for compression therapy and therefore, we have integrated the presented LC tank-based sensor on a compression bandage to demonstrate its potential use in the online monitoring of sub-bandage pressure. The wireless mechanism of presented sensor is based on inductive coupling in near field region. The applied pressure leads to changes in the capacitance of IDC on PLLA substrates, and thus the resonant frequency of the LC circuit is altered as a function of applied pressure. The applied pressure on the sensing capacitor can be transmitted wirelessly through inductive coupling. The resonant frequency of the LC tank is given by

$$f_{res} = \frac{1}{2\pi}\sqrt{\frac{1}{LC} - (\frac{R}{L})^2} \tag{2-3}$$

where R represents the resistance of the printed coil antenna, and L and C represent the inductance and capacitance of the planar antenna coil and the interdigitated capacitor respectively. It may be noted that the unlike conventional coils (made of copper) the total resistance of the current work, which is screen printed silver paste, is not negligible. The self-resonant frequency is much higher than the working frequency, so the parasitic capacitance of the coil antenna does not lower the accuracy of the resonant frequency of the LC tank. The LC circuit impedance is given by

$$Z_{LC} = R_{LC} + jX_{LC} = R + j\left(\omega L - \frac{1}{\omega C}\right) \tag{2-4}$$

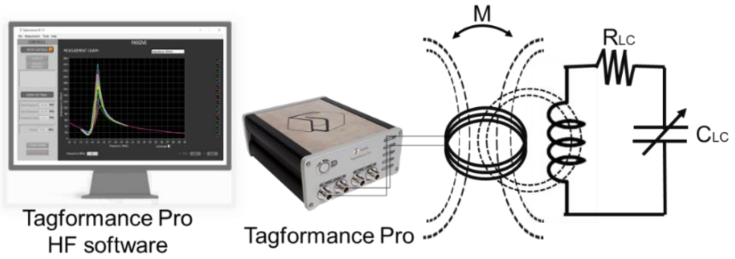

Figure 2-3 Schematic of the setup for near-field communication and power transfer mechanisms for RFID tags at HF frequency using Tagformance Pro.

The wireless response of the LC tags is tested with the applied pressure on IDC capacitor using the load cell set-up. The IDC capacitor is connected in parallel to the coil antenna as shown in **Figure 2-3**. The reader antenna (C60) was used to wirelessly measure the resonant frequency and change of reflected impedance of reader coil. The impedance measured at the reader coil is equivalent to resistance (R_r), inductance (L_r) and tuning capacitance (C_{tune}) of the reader antenna and the reflected impedance of sensing LC tank as described in **Equation 2-5**. M is the mutual inductance between two coupled coils.

$$Z(\omega) = R + jX = R_r + j\omega L_r + \frac{1}{j\omega C_{tune}} + \frac{(\omega M)^2}{Z_{LC}(\omega)} \tag{2-5}$$

As reference measurement has been done prior to the measurement, the impedance of the C60 antenna is subtracted in the response. So, the last term (i.e. $\frac{(\omega M)^2}{Z_{LC}(\omega,P)}$) of the above equation represents the normalized impedance change corresponding to the applied pressure. Beside piezoelectric materials, other materials such as glass microfiber-reinforced polytetrafluoroethylene (PTFE) composite, polyester-based stretchable fabric, Nickel–Titanium (Nitinol) alloy can be used as strain and crack sensors for structural health monitoring (75). PTFE-based sensor has a relatively large resonance frequency change due to its large dielectric constant variation under temperature fluctuation. While PTFE has very good electrical properties, other properties need to be well understood for several considerations.

2.1.2 Antenna sensing through geometry changes

Mechanical stimuli can be used in antenna sensing to detect bending and mechanical stress by effecting antenna geometry (76). These geometrical modifications influence the performance of the antenna sensor, and they also lead to changes in the electromagnetic properties of antenna structure (77-79). The elongation and the bending of the dielectric substrate affect their thickness and their effective permittivity, which influences the resonance frequency of the antenna sensor. Hence, the geometric change can be used for strain antenna sensor. In chapter 5, the textile-based stretchable microstrip antenna is presented as strain sensor. A microstrip patch antenna consists of a radiating metallic patch layer placed on one side of a non-conductive substrate and a ground plane on the other side as shown in **Figure 2-4**. Ideally, an infinite ground plane has a significant role to eliminate back radiations, but finite ground planes are widely used in real applications (80). These low-profile antennas can conform to various surfaces, and therefore suitable for wearable applications. To design patch antenna for a specific frequency a practical width of the radiating element which leads to good efficiency could calculated by

$$\mathrm{W} = \frac{1}{2f_r\sqrt{\mu_0\varepsilon_0}}\sqrt{\frac{2}{\varepsilon_r+1}} \tag{2-6}$$

where ε_r is dielectric constant of substrate and μ_0 and ε_0 are permeability and permittivity of free space respectively. Once W is realized the effective dielectric constant (ε_{reff}) could be realized by Equation 2-7. Due to fringing effects [22], electrically the patch of the microstrip antenna looks longer than its physical dimensions, where the dimensions of the patch along its length have been extended on each end by a distance ΔL.

$$\frac{\Delta L}{h} = 0.412\frac{(\varepsilon_{reff}+0.3)(\frac{W}{h}+0.264)}{(\varepsilon_{reff}-0.258)(\frac{W}{h}+0.8)} \tag{2-7}$$

Typical length of the patch varies between $L_{patch} \approx (0.47 - 0.49)\lambda_d$;that λ_d is the wavelength in dielectric. Since the length of the patch has been extended by ΔL on each side, the effective length of the patch is given by Equation (2-8) that L is actual length of the patch.

$$L_{eff} = L + 2\Delta L \tag{2-8}$$

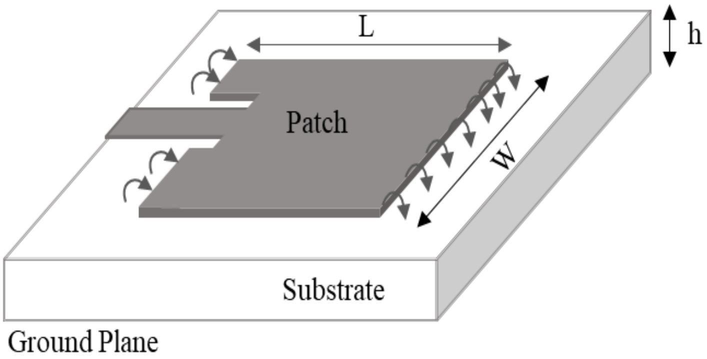

Figure 2-4 Typical configuration of microstrip antenna. The fringe effects and inset microstrip feedline also demonstrated.

To realise strain sensor by microstrip antenna, a common method in the literature is based on tracking the shift in resonant frequency to gauge the occurred deformation (81). As an example, in (82) applying tensile strain along the feeding direction of a stretchable microstrip antenna can cause a downshift in the resonant frequency. However, the maximum applied strain was 15% due to the limited stretchability of the antenna. To increase the range of applied strain, different geometries can be implemented. **Table 2-1** shows a comparison of stretchable microstrip patch antennas that can be found in the literature in terms of stretchability and sensitivity to strain.

Table 2-1 Performance comparison of our proposed textile stretchable microstrip antennas with other stretchable antennas reported in the literature.

Stretchable unit cell	**Conductive material**	**Fabrication method**	**Stretchability**	**Sensitivity (MHz/mm)**	**Reference**
Hierarchical triangular lattice	Copper foil	Cutting with programmable desktop cutter machine	15%	0.82	19
N/A	AgNWs	Drop casting the AgNWs on PDMS	15%	0.245	22
Rectangular mesh	Liquid metal alloy	Injecting liquid metal into micro-channels	20%	0.552@15 % strain	28
Serpentine rectangular meshed patch over solid ground plane	Conductive textile	Cutting with laser cutter	40%	0.20 (avg.)	This work (patch is meshed)
Serpentine rectangular meshed in both patch and ground planes	Conductive textile	Cutting with laser cutter	100%	0.25 (avg.)	This work (both patch and ground plane are meshed)

2.1.3 Antenna sensing using components

Instead of using sensitive material to functionalize the antenna or using deformable substrates to take advantage of geometric deformation for mechanical sensing, one can use a non-sensitive substrate to realize the antenna while using the antenna input to be connected to a sensor. In this case, the transduction is done through an impedance variation which varies the input impedance of the antenna (83). This modifies the reflection coefficient of the antenna and hence, the reflected power. For instance, a dipole antenna sensor can be achieved by placing a sensitive material such as Carbon Nanotubes (CNTs) on its input which connects the two antenna poles as shown in **Figure 2-5 (a) (84)**. The impedance variations of the CNTs due to the external stimuli such as gases will be transduced as a variation of the antenna reflection coefficient and hence, the reflected power. This reflected power variation at the receiver will be the sensing indication of the presence of a gas (85). The input antenna terminals can be loaded by a sensor for realisation of antenna sensor using a component (sensor). For example, the antenna can function as a temperature sensor by connected its input to a thermistor as shown in **Figure 2-5 (b)**. Since the thermistor translates the temperature into a change of its impedance, the variation of the impedance of the thermistor due to the temperature will affect the reflection coefficient of the antenna as mentioned above (86, 87). The chapter 3 focuses on this concept, designing NFC RFID sensor tag in which the RFID chip (RF430FRL152H) includes a built-in temperature sensor as well as capability to integrate to external sensors.

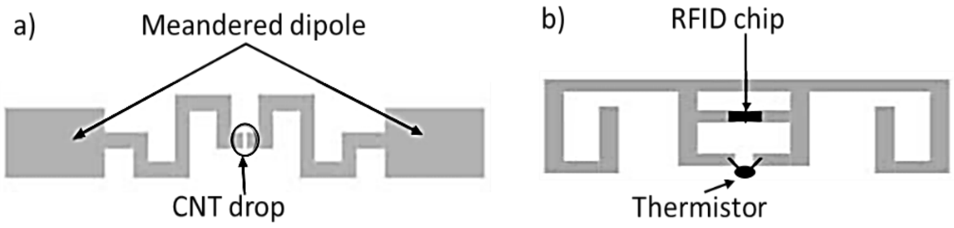

Figure 2-5 (a) antenna sensor (chipless) with input connected to carbon nanotubes (CNT) that vary impedance with the introduction of a gas (88). (b) antenna sensor connected to a variable resistance (thermistor) with chip for temperature sensing. Adapted from (87)

2.2 Antenna sensor implementations using RFID technology

The development of RFID has started a new direction in the wireless technologies. An RFID system consists of a radio frequency tag and a reader. The reader is responsible for generating and transmitting the interrogation signal to the tag and then decodes the tag's backscatter signal. The tag collect data from the reader and then transmits that data through radio waves using a RFID standard telecommunication protocol.

2.2.1 RFID classification

There are two broad types of RFID: an active and passive. An active tag has an internal source power such as battery which operate generally in much higher interrogation range and has larger memory for storing data. For the passive type, power is drawn from the reader through inducing electromagnetic current in the antenna of the tag. In addition to the aforementioned two categories, there is also a semi-passive configuration where a passive tag can be enhanced with a battery allowing to power additional sensors or to increase the tag read range (89).

For passive RFID systems, the RFID tag has no on-board power source, however, it is activated by using the power emitted from the reader. This power is needed to turn on the integrated circuit (IC). The passive RFID tags modulate the backscattered signal to transmit the stored information back to the reader. Passive RFID tags have the advantage of being simpler in structure, lighter in weight, and less expensive while offering an effectively long operational lifetime. Passive tags have the disadvantage of having short read range (5-6 m) compared to the active tags, also they have limited storage capacity for information and poor performance in a noisy environment (90).

For active RFID systems, tags have their on-power source as well as internal electronic circuitry for performing various operations (91). In this category, the on-board power source supplies the microchip operation and transmits data to the reader. The on-board electronics incorporate microprocessors, sensors, and input/output ports, etc. In an active RFID system, the tag always communicates first, followed by the reader. As the presence of a reader is unnecessary for the data transmission, an active tag can broadcast its information to surroundings even in the absence of a reader. This type of active tag, which continuously transmits data with or without the presence of a reader, is also called a transmitter. Another type of active tag enters a sleep or low-power state in the absence of interrogation by the reader. The reader wakes up the tag from its sleep state by issuing an appropriate command. The ability to enter a sleep state conserves battery power, and consequently, this type of tag generally has a longer battery life than an active transmitter tag. This type of active tag is called a transmitter/receiver (92).

In between passive and active tags, there is the category of semi-passive tags. They have their own power sources; however, they do not have a radiofrequency transmitter; instead, they are based on the principle of backscattering modulation to transmit their information to readers. The advantage of semi-passive tags is that they are cost-effective compared to active tags (93).

In terms of frequency range of operation, RFID systems can be classified as: low frequency (LF), high frequency (HF), and ultra-high frequency (UHF) systems. Among them, UHF RFID systems (860 – 960 MHz) have the greatest read range (3 – 15 m) and the highest reading speed, but they require the use of specialised equipment and reader antennas (94). HF systems (3 – 30 MHz) usually have a read range of a few centimeters up to about a meter and make use of magnetic coupling to communicate between the HF tag and the RFID reader. A specialized subset of HF band is the NFC, which operates at a single frequency (13.56 MHz) and is a global communication protocol approved by the International Organization of Standardization (ISO). It mainly focuses on secure identification applications (95). This is achieved by harvesting energy from the electromagnetic field induced by an external RFID reader, which in our case can be any NFC-enabled smartphone. A key advantage of NFC tags over other RFID systems lies in their ability to be read by NFC-enabled smartphones, making this technology within the reach of any individual user (96, 97). For this reason, NFC sensing tags have gained widespread popularity in countless applications such as wearable smart bandage, smart packaging, and modified atmosphere packaging (MAP) for food monitoring (98-100). Lightweight, flexibility, security, and low-power consumption are desired properties for these smart tags and printing technologies appears to be promising method for fabrication of such tags.

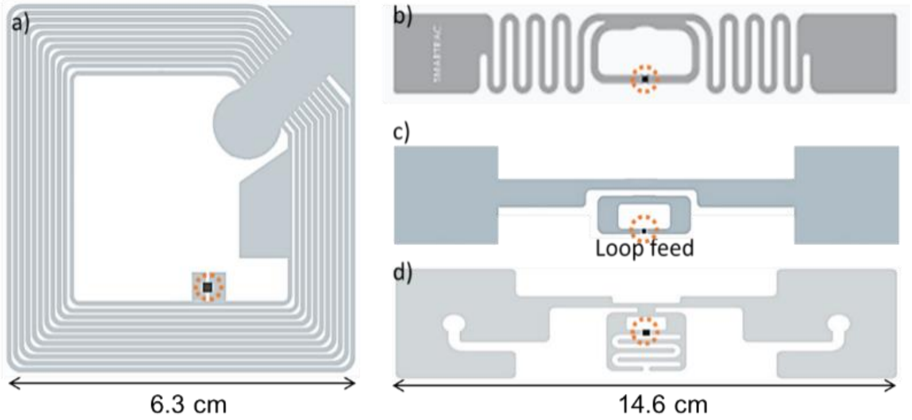

Figure 2-6 Example of RFID tags consisting of a chip connected to an antenna. a) Typical NFC RFID tag. b) meander lined RFID tag from Smartrac. c) Loop fed inductive UHF RFID. d) Moisture sensing UHF RFID tag from Smartrac. The RFID chips are highlighted using a red dotted circles.

Figure 2-6 shows various commercially available RFID tags. **Figure 2-6 (a)** is an example of NFC tag. The tag consists of an antenna which is an inductive coil L, an electronic chip that performs the communication operations as well as contains the tag identifier, and finally a capacitance C which is used to adjust the resonance frequency of the tag LC circuit. The communication between the RFID tag and the reader is achieved by magnetic coupling. When the near field tag is placed in the vicinity of the generated magnetic field of the reader as shown in **Figure 2-7**, an alternating voltage will appear across the inductive loop antenna of the tag (101). This voltage is first rectified in the energy harvester unit of the tag in order to power the electronics of the tag chip. The tag sends data back to the reader using load modulation (102).

Another common type of RFID tags is UHF RFID that comply with UHF Gen 2 standard covering 860 to 960 MHz (regionally defined). **Figure 2-6 (b),(c)** shows the common types of UHF RFID tags. The main advantage of this type over NFC tag is the longer reading range. Most UHF RFID tags reported so far has a reading range over 1 m. Considering the design and reader characteristics the range can reach higher than 10 m as well. The maximum reading range is calculated using Friis Equation

$$r_{max} = \frac{\lambda}{4\pi}\sqrt{\frac{EIRP_{reader} \cdot G_{tag} \cdot \tau}{P_{tag}}} \tag{2-9}$$

where the $EIRP_{reader}$ (effective isotropic radiated power) based on European state spectrum regulations is 3.28 W, G_{tag} is gain of the tag, τ is transmission loss and P_{tag} is defined for each chip. Since UHF tags can store more data and the reading range is much higher than NFC tags; these are good candidate for inventory systems as only one NFC tag can be scanned at a time.

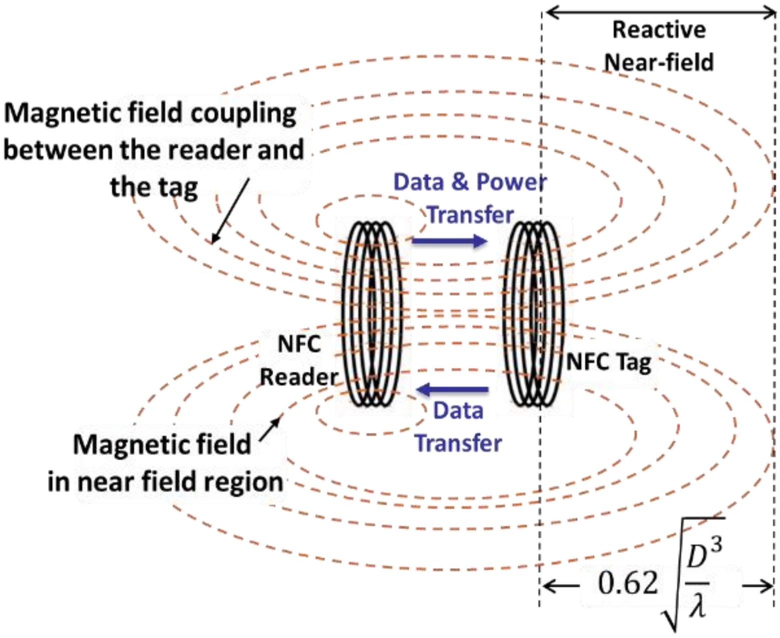

Figure 2-7 Near-field communication and power transfer mechanisms for RFID tags operating at HF frequency

Another microwave approach for sensing is using chipless RFIDs. It is a new research area for radio frequency identification and sensing which is based on RF resonant components without any electronics or discreet circuit elements. Chipless RFID tags usually are based on multi-resonant structures (103), which is compatible with low-cost manufacturing technologies. In the frequency domain approach, the information is coded in the resonance peaks or dips in the frequency spectrum. These peaks are related to the resonators in the structure of the chipless tag. Thus, the presence (or absence), or even the resonance shift at a particular frequency constitutes the coding element. Therefore, the interrogation signal required to interrogate the chipless tag have to be wide frequency band signal. **Figure 2-8 (a)** is an example of multi-resonant structure with 35 bits capacity for identification. The Transmitting antenna (T_x) is horizentally polarised UWB monopole and the receiving antenna (R_x) is vertically polarised UWB monopole antenna. 35 spiral resonators provide 35 various resonant nulls in the frequency response of the multi-resonant tag as each introduces a particular null that is used to encode data. The dimensions of the spirals define each resonance. The null in the insertion loss (S_{12}) represent "0" and shorted spiral is defined as "1" for data encoding as shown in **Figure 2-8 (b).**

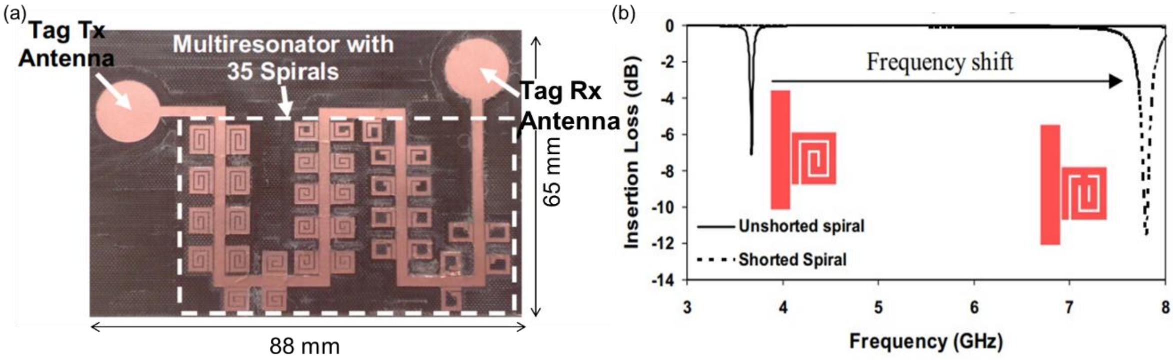

Figure 2-8 (a) Example of chipless tag with frequency signature. (b) Frequency shift of resonant frequency using shorted spiral (103)

Unlike conventional RFID technologies where an RFID chip is connected to an antenna, the chipless RFID system comprises of a tag structure (resonator or an antenna) that does not contain an electronic component and does not follow a standard communication protocol. It can be read remotely unlike the optical barcode which requires close contact. The chipless tag does not contain a memory, and the identification is based on to its geometry since it is based on resonant structures. Chipless technologies have the advantage of being passive, less expensive, and can be fabricated on a printable flexible substrate suitable for green electronic application that aim to reduce e-waste.

The principles of operation of chipless RFID tags can be classified based on how the electromagnetic signature of the tags is generated. A chipless RFID tag can be considered as a static radar target with a specific electromagnetic signature. To generate the signature, one can use either the time temporal, frequential or based on a radar imaging principle approaches where the chipless tag geometric structure provides a specific, even unique, signature. In case of the temporal signature, a plus position modulation coding is obtained by connecting a complex load to the antenna. The complex load is usually in the form of transmission line that creates reflections at certain moments (104).

In the frequency domain approach, the information is coded by the resonance peaks or dips in the frequency spectrum. These peaks are related to the resonators which consists of the structure of the chipless tag. Thus, the presence (or absence), or even the resonance shift at a particular frequency constitutes the coding element. Therefore, the interrogation signal required to interrogate the chipless tag should be wide frequency band signal.

Due to the non-conventional reader protocols or a non-standard interrogation technique such as the use of ultra-wide band RF signals which are not compliant with the RFID frequency bands regulations, there is a large gap between conventional RFID systems and the chipless systems. Recent work tried to develop a framework of a chipless wireless system for sensing in compliance with the standard international regulations (105). The chipless sensor is based on a C-scattered as the resonant structure designed to resonate in standardized frequency bands. The idea of sensing for the proposed chipless sensor is based on threshold sensing. Threshold sensing is ideal for applications that require knowing transition or approximate ranges of values rather than a precise value. A low-cost reader has been developed using Universal Software Radio Peripheral (USRP) with GNU radio interface. Other attempt to reduce the gap between the conventional RFID and chipless is proposed in (105). A compact structure formed by a single C-scattered with multiple embedded slots designed to respect the conventional radio frequency (RF) emission regulations. The sensing principle is based on the detuning of the resonance frequency peaks of the backscattered signal from the slotted scatterer due to temperature variations.

2.2.2 Self-sensing RFID

Three approaches can be implemented to integrate sensing capabilities into the RFID tags. The first approach exploits the sensitivity of the RFID tag antenna to the environmental change in its surroundings (106). The second approach is to use the behavior of the RFID chip and the variation of its electrical response as function of some external parameters such RF power, temperature, and humidity. The third approach uses the ability of the RFID chip to integrate an external sensor or in some cases using RFID chip build-in sensor (107).

In the first approach, sensing can be achieved by studying the variation in the analogue response (sensing indicator) of the tag as a result of a change in the sensed measurable data using a reader. In this sensing paradigm, the antenna can be directly considered as the sensor element without the need for additional components. This change can be observed on several communication parameters such as frequency tuning, backscattered power or received signal strength indicator (RSSI), read range, turn-on power, phase rotation, group delay, etc. as different responses of the RFID in the two modulating states (108). To this purpose, a precise calibration is needed to measure the sensing metric without the effect of orientation and distance of the reader (and other environmental parameters which can affect the electromagnetic power). In order to do calibration, a reference tag also is included and the decision is made based on the difference of the backscattered power signal between the sensing tag and the reference tag. So, the effect of undesired reflections from environment of the sensing tag can be removed (109).In the second approach, the sensing is based on exploiting RFID chip internal behavior. RFID chips perform energy harvesting tasks to generate the required DC supply voltage for its internal circuitry or for external sensor and channel diversity. Another interesting feature of some RFID chips is the auto-tuning functionality (110). The antenna of UHF RFID tag as a temperature transducer equipped with the UHF RFID chip with self-tuning is operating as a very low-power sensor with high read range and small size (111). The antenna of the tag is taking advantage of the intrinsic characteristics of the used substrate (dielectric variation) to vary its overall complex impedance according to temperature. These changes of the impedance of the antenna are leading the self-tuning internal circuit of the used RFID chip to self-tune itself to have better impedance matching between the RFID integrated circuit (IC) and the tag's antenna. This improves the reading range of the tagBased on the acquired value an estimation of the sensed temperature can be made (112). The tag ID includes an RFID identifying number (EPC code) along with sensing codes so the sensed data is available as digits in the EPC code readable using a RFID reader (110).**Figure 2-6 (d)** shows an example of commercial self-sensing tag that can measure humidity wirelessly. The third approach relies on RFID chips with integrated sensing or with external sensors interfaces (113). External components and additional circuitry can be added to the main core of an RFID tag, namely readout circuit units, analog to digital converters and external sensors to achieve a complete sensor platform. RFID chips with sensors connected through the digital side do not have any modification in the analog front-end circuit or the antenna. In this case, the external components are responsible for managing the sensing functions in the tag, while the antenna is used as a communication interface to transmit the sensor data to the user (114). **Figure 2-9** shows an example of commercial RFID tag with RFID having external sensor circuitry. The device features a pressure and temperature sensor working in 860-960 MHz band. The reading range is 2 m according to the manufacturer datasheet.

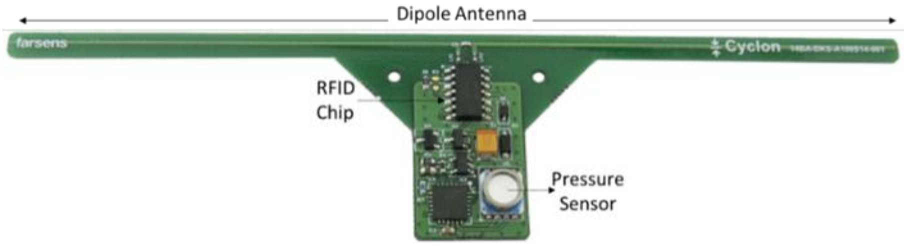

Figure 2-9 Example of a commercial RFID sensor-tag (115)

The main advantage of this solution is its compatibility with the current EPC Class 1 Gen 2 standard and its capability to interface multiple sensors, which can be of almost any kind (limited only by power consumption and response time). Additionally, the electromagnetic power transmitted by the reader can be exploited to power the tag by means of energy harvesting, including the external components and sensors (116). The main challenge to design these components is to meet the supply power and time constraints. In passive transponders, all steps of sensing, acquisition and data transmission/storage should be done before the end of communication when the energy ends. The available power to a typical UHF tag at 4.5 m of distance from reader is around 10 µW, where about 8 µW is consumed by standard tag circuitry (117). Hence, the power left to supply sensing circuitry is not greater than 2 µW which is below the consumption of standard sensors.

Recent progress in making devices on unconventional substrates that conform to surfaces shows a promising future for consumer electronics for human health (118-120) and food (86) (121, 122) and environmental quality monitoring (123, 124). In the literature, there are several attempts and examples to design RFID sensors by exploiting this concept.

2.3 Antenna sensor implementations using Metasurfaces

Besides the classes of RFID tag-based sensors, there is an emerging class of metasurfaces microwave structures that show a promising new way to sensing without the need for discrete circuit elements. In microwave spectrum, metasurfaces are broadly defined as artificially engineered planer structures that exhibit electromagnetic (EM) properties which are difficult to obtain using conventional planar microwave circuits. Unnatural properties associated with metasurfaces such as negative refractive index and super lenses have attracted a significant research interest over the last years.

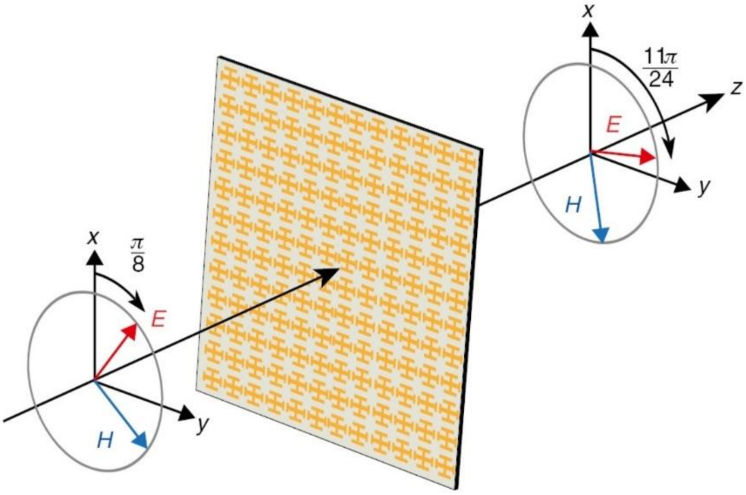

Figure 2-10 Reflection-less metasurface designed for polarization rotation (125)

Metasurfaces are constructed in terms of periodical patterned structures with a periodicity in the subwavelength of the guided wavelength. **Figure 2-10** shows an example of metasurface design for polarization rotation (125). Their interesting properties include negative or low values of permittivity (ε), permeability (μ), and refractive index (*n*), which do not exist naturally in conventional materials are achieved by modulating the behaviors of electromagnetic waves through specific boundary conditions of the meta-surface.

These properties have allowed the development of new concepts and devices and possible utilization in many novel applications (126). Demonstration of using metasurfaces in telecommunications has been presented in (127), through a direct antenna modulator (DAM) transmitter. Metasurface-based DAM is an emerging technique where a baseband signal is modulated directly onto a radio frequency (RF) carrier wave using a reconfigurable metasurface. This technique simplifies greatly the signal transmission and offers a low-cost, low-complexity solution for the Internet of Things (IoT). Metasurface structures with their unique properties can be combined with passive sensor elements such as temperature sensing elements or using the dielectric properties as a transducer. This is a promising technique for realizing microwave sensor devices with advanced properties. Implementing metasurface on a flexible substrate can open the door for flexible metasurface sensors for mechanical force detection. Different examples for metasurface inspired sensors are given. For instance, a metamaterial inspired radio frequency touchpad sensor system based on two split ring resonators (SRRs) is proposed (128). The touchpad consists of two SRRs resonating at two different frequencies. When a finger is placed on first SRR first, its resonance changes due to electromagnetic coupling between the SRR and the finger, and similarly, for the second SRR. The proposed touchpad system can detect a finger wearing a glove, in contrast to capacitive touchpads utilized in contemporary smart phones.

Metamaterial inspired multi-band planar microwave sensor for aqueous biological samples has been reported (129). The proposed sensor consists of a spoof surface whispering gallery mode (SS-WGM) resonator connected to a spoof surface plasmons polariton (SSPP) transmission line in a special arrangement. The proposed sensor can localize the electromagnetic (EM) field into a specific region due to its slow-wave propagation characteristics which enhances the interaction time of the sample under test and hence offers higher sensitivity. Due to the localization of the EM wave the metamaterial sensor can sense the small volume of the bio-samples which is essential in aqueous sample due to significant reduction of the quality factor of the sensor in large aqueous volume. A dynamic metasurface aperture has been used in indoor motion detection for smart homes. It operates based on disordered cavities for radio frequency (RF) waves where the perturbation of the fundamental sensitivity of modes of such cavities is caused by moving objects (130). This work demonstrated that the use of dynamic metasurface apertures can substantially enhance the performance of RF motion detection.

Popular metasurface sensor concepts in the microwave regime are based on the classical split-ring resonator (SRR) structures (131) where the designed antenna uses a metamaterial in the form of a split-ring resonator (SRR) loading on a radiating patch for non-invasive blood glucose monitoring. The SRR based tag is combination with dextrin-capped gold nanoparticles (d-AuNP) as labels decoded at microwave frequencies is demonstrated as a biosensor for detecting pathogenic bacteria in milk (120) suitable for food supply chain for the detection of pathogenic bacteria in the liquids.

Another approach for metasurface based sensing is using the metasurface pattern in combination with transmission line (132, 133). Combining the metasurface with transmission line adds additional transducing mechanisms for metasurface sensing (134). One approach to transmission line as a sensor is to monitor the detuning of the transmission line or line resonator properties due to an external effect. A straightforward implementation of this concept is designed in a way that the capacitive elements are highly sensitive to dielectric loading of the structure (134).

2.4 Materials and Fabrication: challenges and opportunities

2.4.1 Dielectric materials

For any antenna designed for epidermal and wearable applications the flexible substrate material used needs to have minimum dielectric loss, low relative permittivity, and low coefficient of thermal expansion, and high thermal conductivity (135). These constraints guarantee the high antenna efficiency (in different environments) where some exception is made for miniaturized antennas where the dielectric constant of the substrate needs to be high (136). Although polymer substrates show a promising solution for flexible antennas and microwave component, they have higher dielectric loss compared to the rigid substrate which leads to low efficiency. For example, polyethylene terephthalate (PET) polymer has dielectric loss ($\tan \delta=0.08$) compared to the common commercial rigid substrates such as Rogers PCB substrates which have a dielectric loss in the order of 10^{-3} or LTCC ceramic substrates which have a dielectric loss in the order of 10^{-4}. One emerging approach to improve the flexible polymer substrate dielectric loss is by introducing nanocomposites (137, 138). Dielectric improvements can be studied by, forming nanocomposite of polymer and nanoparticles/wires of low loss dielectric. This approach can improve the performance of the flexible antenna by reducing the dielectric loss as well as tailoring the value of the dielectric constant (ε_r) of the composite which is another important parameter in the realization of the antenna. Recent study showed improvement in the dielectric loss of silicon rubber based dielectric elastomer by means of nanocomposite of Barium Titanate nanoparticles (BTNPs) (139) where the surface has been modified by polyphenolic extract from walnut husks. The results show an enhancement in the mechanical performance of the dielectric composites. Dielectric property measurement showed that dielectric composites containing walnut polyphenols modified Barium Titanate particles (WNBT) had higher dielectric constants and lower dielectric losses than that of the unmodified dielectric.

Polymer materials which are using as a flexible/stretchable substrate are less chemically stable compared to rigid substrates meaning they could dissolve or swell in organic solvents. Moreover, any change in physical and chemical properties of substrate materials could fail the device performance. Material considerations are key element that define which fabrication technique is suitable for specific application and in some devices, use of hybrid patterning techniques is required.

For the fabrication of flexible antennas thin glass (140) is very common choices. Even though thin glass is bendable to some extent, it has the disadvantage of being brittle. Metal foils can sustain high temperatures and provide inorganic materials to be deposited on it, but the surface roughness and high cost of the materials limit its applications (141). This leaves the polymer materials to be the best candidates for flexible/stretchable antenna applications because of high deformability and mechanical robustness. Different polymer materials have been used as substrate. As an example, the thermoplastic semi-crystalline polymers: PET (142) and polyethylene naphtholate (PEN) (143), the thermoplastic nanocrystalline polymers: polycarbonate (PC) (144) and polyimide (PI) (145). For applications that stretchability is needed Polydimethylsiloxane (PDMS), Ecoflex, Solaris, etc. are good candidates (79). Among these transparent and hyper-elastic polymers such as Ecoflex are preferred as they show higher viscosity and hence the interfacial bonding between the substrate and the textile is very strong. Moreover, Ecoflex is an ultra-soft polymer material with Young’s modulus of 125 kPa, indicating good conformation with human skin in the case that the device is placed directly on human skin for monitoring applications (146).

2.4.2 Conductive materials

To realize stretchable antennas a wide variety of conductive materials can be explored, including Ag-PDMS composite (147) and metal nanowires (148, 149), etc. For printed antenna varoius conductive inks/pastes are available on the market. More recently, the liquid metal alloys also such as Eutectic Gallium-Indium (EGaIn) and Galinstan have been explored as they are highly deformable and can be processed at room temperature (150). Further, they could be patterned by lithographic methods (151, 152) and injection of liquid metal into microfluidic channels (153) to form a flexible and stretchable antenna. Despite the recent developments in stretchable and flexible conductive materials, poor conductivity is a bottleneck to deploy these materials in radio frequency (RF) wireless technologies. To address the challenges CNTs-composite based deformable antennas have been reported (82, 154).

In a different approach, the use of conductive textiles composed of polymer-based fabric coated with conductive materials such as copper and silver could address the above-mentioned issues. One of the advantages of using e-textile with high conductivity is reduced cost of integrating an antenna into garments. Emerging fabrication techniques also make it feasible to pattern conductive textiles into an antenna shape. For example, antennas with compound geometries can be fabricated using either computerized sewing machines or automated laser cutters. The thread size, woven pattern, and stitch density have an impact on the appearance and performance of the antenna. By using these fabrication tools, it is possible to develop textile antennas with significantly enhanced conformability compared to the traditional rigid antennas made from conventional conductive materials such as silver and copper sheets.

Patterning conductive textiles using sewing machine and laser cutter is another emerging method to fabricate antenna in order to improve conformability. The thread size, woven pattern, and stitch density have an impact on the appearance and performance of the antenna (79). Due to porosity of textiles, they have low relative permittivity which is desirable. The distance between adjacent threads should be smaller than the wavelength of the signal being transmitted through the antenna. One drawback of using conductive textiles is that they are prone to fraying over time. Instead of using commercial conductive textiles, it is possible to use conductive threads. By doing embroidery it is possible to control the direction of current on the embroidered antenna. Moreover, the size of needle and thread type are other factors which make it easier to tailor the design. The main issue with conductive threads and textiles is that the conductivity decreases in cleaning treatments using water and detergents as conductive nanoparticles can be removed during washing. This is due to poor bonding between the conductive nanoparticles and the textile yarns (155).Considering all above mentioned, it is feasible to fabricate flexible antennas (or RFID) which can be integrated to garments and other wearable devices.

2.4.3 Fabrication techniques

This section covers briefly fabrication techniques used in different stages throughout the thesis.

Photolithography is well established in microelectronic manufacturing over the past 50 years on rigid substrate, silicon and glass for instance, are adapted with soft electronics as well (156). However, patterning of flexible material by photolithography is challenging. Photolithography involves consecutive steps. **Figure 2-11(a)** shows a common three steps of lithography process. First step is mask preparation, then usually photoresist is deposited on substrate and developing photoresist is the next step which is usually involves in high temperature curing. This process is time consuming and materials usually waste during the etching process. Besides, these processes involve series of chemical reactions they may not be compatible with polymers used as substrates. Printing techniques which are emerging in the last decade can be an alternative for conventional lithography.

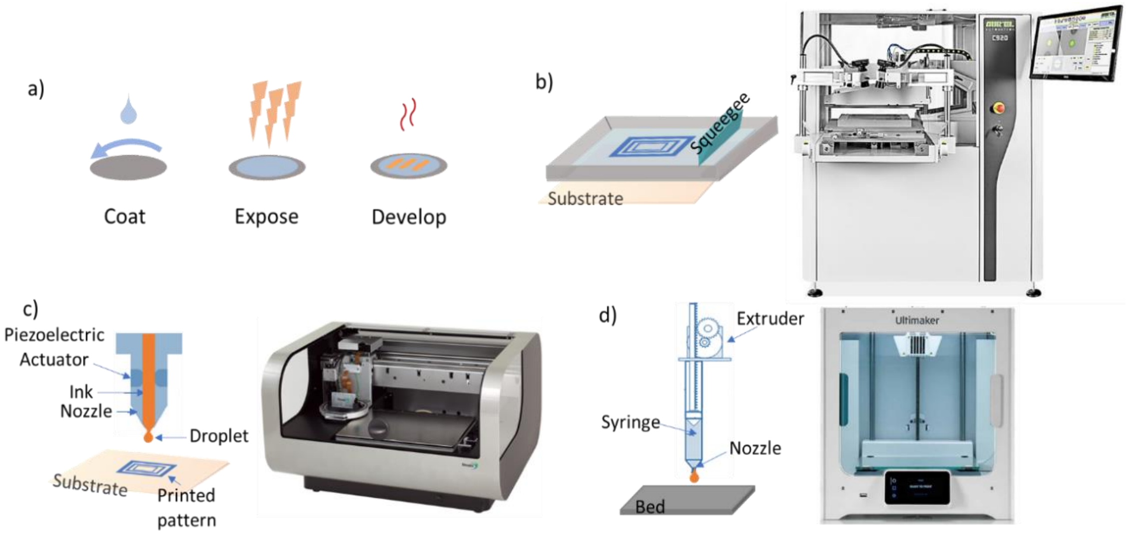

Figure 2-11 Schematic illustration of some common fabrication techniques along with some relevant printers for realising flexible/stretchable electronics (a) photolithography, (b) Screen printing method and semi-automatic stencil-screen printer Aurel C920, (c) Piezoelectric inkjet printing and Dimatix (DMP-2831), (d) FDM 3D printing mechanism and Ultimaker S5 3D printer.

In application such as RFID or smart packaging, lead time and cost reduction are important factors, photolithography is not appropriate process. In printing techniques, since deposition and patterning are done at a same time, lead time is shorter than photolithography. **Figure 2-11 (b),(c),(d)** shows the major printing methods compatible with flexible/polymeric materials which are mainly used in fabrication of flexible/stretchable antennas in the framework of this thesis. While screen printing is suitable for mass production by using predefined masks, inkjet printing is non-contact method, depositing ink on a substrate without using a mask. This is based on drop-on-demand (DoD) technologies that nozzles only discharge droplets whenever digital signal asks for it (157). In order to achieve high conductivity usually inks require thermal annealing, which may not be compatible with some flexible/stretchable substrates. In this regard, a new class of conductive inks which anneal in room temperature have been developed recently (158). Nozzle clogging, by far, is the most reported issue in inkjet printing. Besides above mentioned methods, 3D printing of functional biomaterials is advancing implantable wireless devices allowing in vitro culturing of cartilage tissue around conductive coil antenna to enable wireless readout (159).

2.5 Summary

The increasing popularity of flexible electronics for wearables had led to increase the demands on integrating as many electronic components as possible for sensing and communication. This resulted in a huge complexity in both the design, realization, and operation of the wearable device. As one flexible sensor node became a big lump of multi sensor devices, electronic interconnections and wireless devices the need to reduce this complexity became indispensable for further advance the flexible electronics design and applications. In this regard, recent advances in the areas of antenna sensing with the incorporation of smart materials show a promising solution that can open the door to the implementation of a smart sensor node where some of the sensing and identification functionalities can be done through either the smart material or the geometry of the device.

This chapter has presented the recent trends in antenna sensing with the aim of taking advantage of the antenna as sensing element for flexible and wearable applications. General classification of RFID tags, principle of their operation, and methods to design self-sensing RFID tags have been discussed as well. Different methods of transduction mechanism were presented. Since the antenna transduction requires sensitive/functional material to be able to respond to stimuli, an overview of smart sensing materials appropriate to a particular stimulus was detailed. Moreover, a reflection on some of the implementation for future improvement on the performance of flexible sensing antennas has been presented. According to the framework of this thesis, some materials which are commonly used in fabrication of flexible electronics have been introduced. Also, briefly the most common fabrication techniques for realization of flexible electronics have been presented.

Chapter 3. Near-Field Communication based sensing tag[1]

3.1 Introduction

The development of customizable, inexpensive, mass-producible, environmentally friendly smart RFID tag is on high demand for various applications such as health and food quality. As it was established in chapter 2, one method to develop sensing RFID tag is to integrate internal/external sensors to the conventional RFID tags which originally are used for identification. This chapter presents design, simulation, fabrication and characterisation of screen-printed NFC tag. The developed sensing tag is integrated with some sensor as it will be described later in this chapter to demonstrate sensing capability of the tag in two applications: (i) The tag along with the sensors were integrated to a wound dressing and wireless sensor reading carried out though NFC enabled smartphone using the developed smartphone application for powering the system as well as real-time sensor data acquisition. (ii) An LED is used as an indicator to check temperature and strain in food packages (qualitive measurement) which can be useful for any NFC enabled smartphone users without need for a particular smartphone application.

3.2 NFC antenna design, simulation and fabrication

The NFC tag consists of a NFC RFID chip and an antenna. The typical NFC antenna is a planar loop (coil, L_{ant}) consisting of some turns of conductive traces. The NFC transponder chosen for this work is the RF430FRL152H a programmable 16-bit MSP430 low-power microcontroller based integrated circuit (IC) from Texas Instruments (Dallas, Texas, USA), that includes an internal capacitor (C_{int}) of 35 pF (160). According to the equation (3-1) to achieve a resonance frequency at 13.56 MHz compatible with NFC technology the inductance of the coil should be 3.94 μH but to reduce size of the coil we decided to use a tuning capacitor (C_{ext} = 39 pF) parallel to the coil thus inductor should be L_{ant} = 1.8 μH. The quality factor (Q) of the coil antenna can be calculated from equation (3-2) where R_{ant} is the

---

[1] Design, simulation, fabrication and characterization of all printed NFC tags were carried on by F. Nikbakhtnasrabadi.

antenna resistance at resonance frequency (13.56 MHz).

$$f_{ref} = \frac{1}{2\pi\sqrt{L(C_{int}+C_{ext})}} \tag{3-1}$$

$$Q = \frac{R_{ant}}{2\pi f_{ref}\, L_{ant}} \tag{3-2}$$

For the initial design of the planar inductor, the Grover Method (161) was used on the basis of the following equation:

$$L_{ant} = L_0 + \sum M \tag{3-3}$$

where M is the mutual inductance between each of the antenna segments and L_0 is defined as per the following equation, being s the number of segments and L_j the self-inductance of each one:

$$L_0 = \sum_{j=1}^{s} L_j \tag{3-4}$$

On the basis of the Grover Method, the inductance of an antenna with square coils was estimated as:

$$L_{ant} = K_1 \mu_0 N^2 \frac{d}{1+K_2 \cdot p} \tag{3-5}$$

where μ_0 refers to the vacuum permeability ($4\pi \times 10^{-7}$ H/m); N is the number of turns; d is the average coil diameter defined as $d = (d_{out} + d_{in})/2$; p is the fill ratio calculated as $p = (d_{out} - d_{in})/(d_{out} + d_{in})$; and K_1 and K_2 are non-dimensional coefficients that depend on the antenna layout (e.g., square, hexagonal, octagonal, etc.). For our squared-shape antenna, $K_1 = 2.34$ and $K_2 = 2.75$ (162).

Advanced Design System (ADS) simulator (Keysight Technologies, Santa Clara, CA, USA) is used to obtain final dimensions and turns of our antennas. Four designs have been considered as it is shown in **Figure 3-1**. The simulation results are shown in **Figure 3-2**. The sheet resistance of the silver paste was considered 95 mΩ/sq in simulations.

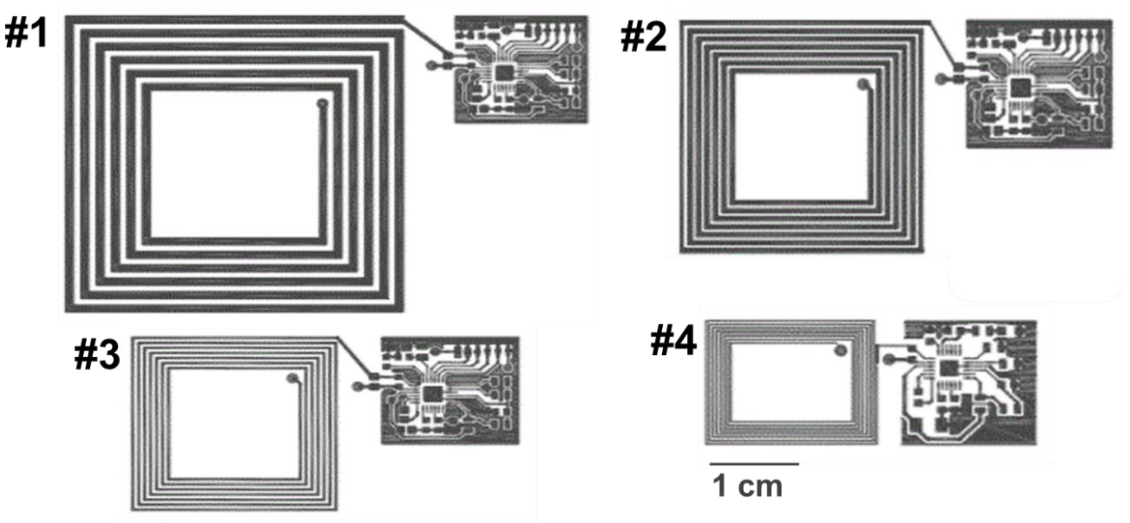

Figure 3-1 The layout of designed NFC tag.

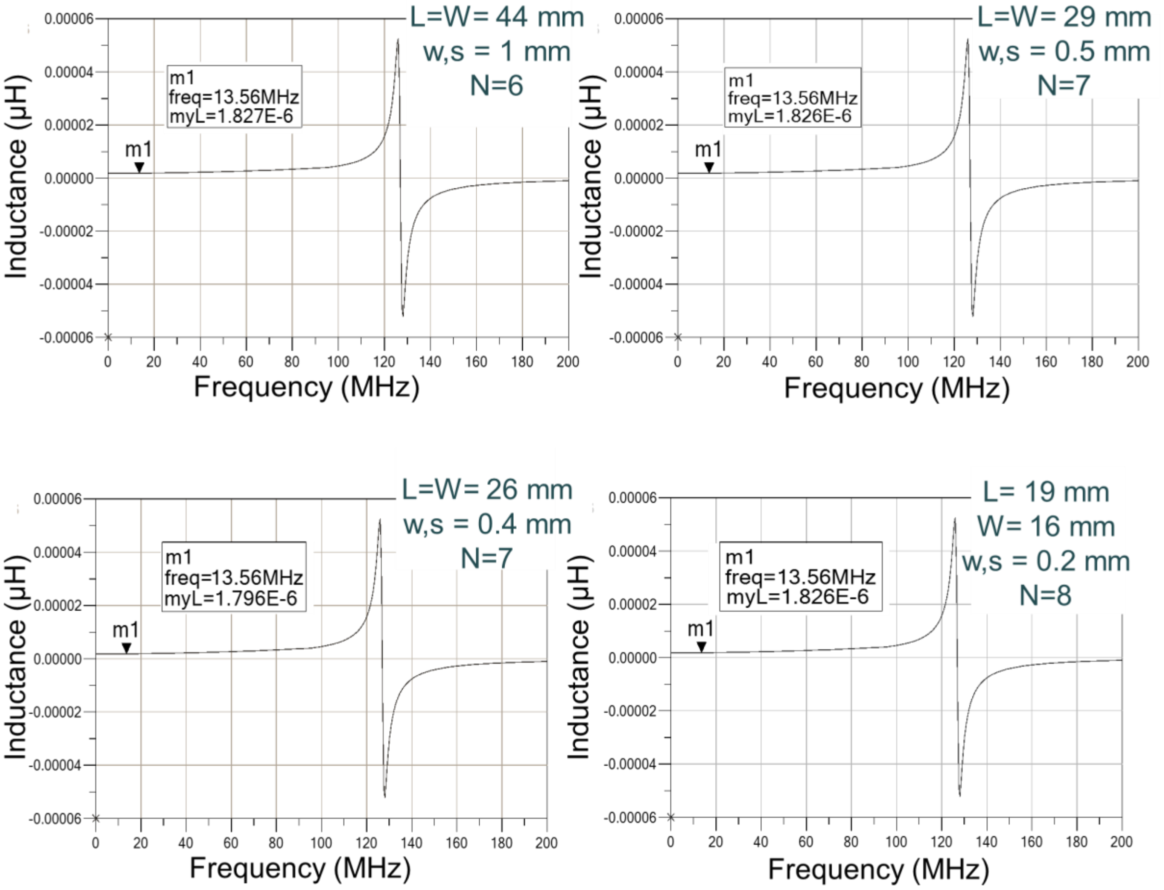

Figure 3-2 Simulated results of four planar inductors. The target value for inductance was 1.8 μH.

Designs were screen-printed on various flexible substrate using silver paste (PE872, Dupont, UK) and characterised using an Agilent 4294A Precision Impedance Analyzer and a 42941A impedance probe kit fixture (Keysight Technologies, Santa Clara, CA, USA). A semi-automatic screen printer (model C920, Aurel Automation, Italy) was used for printing. After printing they were cured at air oven 90 °C for 30 mins. The geometry, simulated and measured value of the inductors are summarised in **Table 3-1**. w and s stand for width and space between conductor tracks respectively. The resistance value of each one-layer printed inductor and quality factor are also included. The fourth design which has the narrowest printed tracks did not behave as an inductor with the predicted value. This could be due to density of the tracks means that 0.2 mm interspace between tracks is not a right space even though the simulation shows that it can create 1.83 μH inductance. Among the three other designs, the second one which was a square-shaped inductor with 29 mm length shows the highest quality factor so we continue with this design, increasing the number of printed layers to achieve the maximum quality factor.

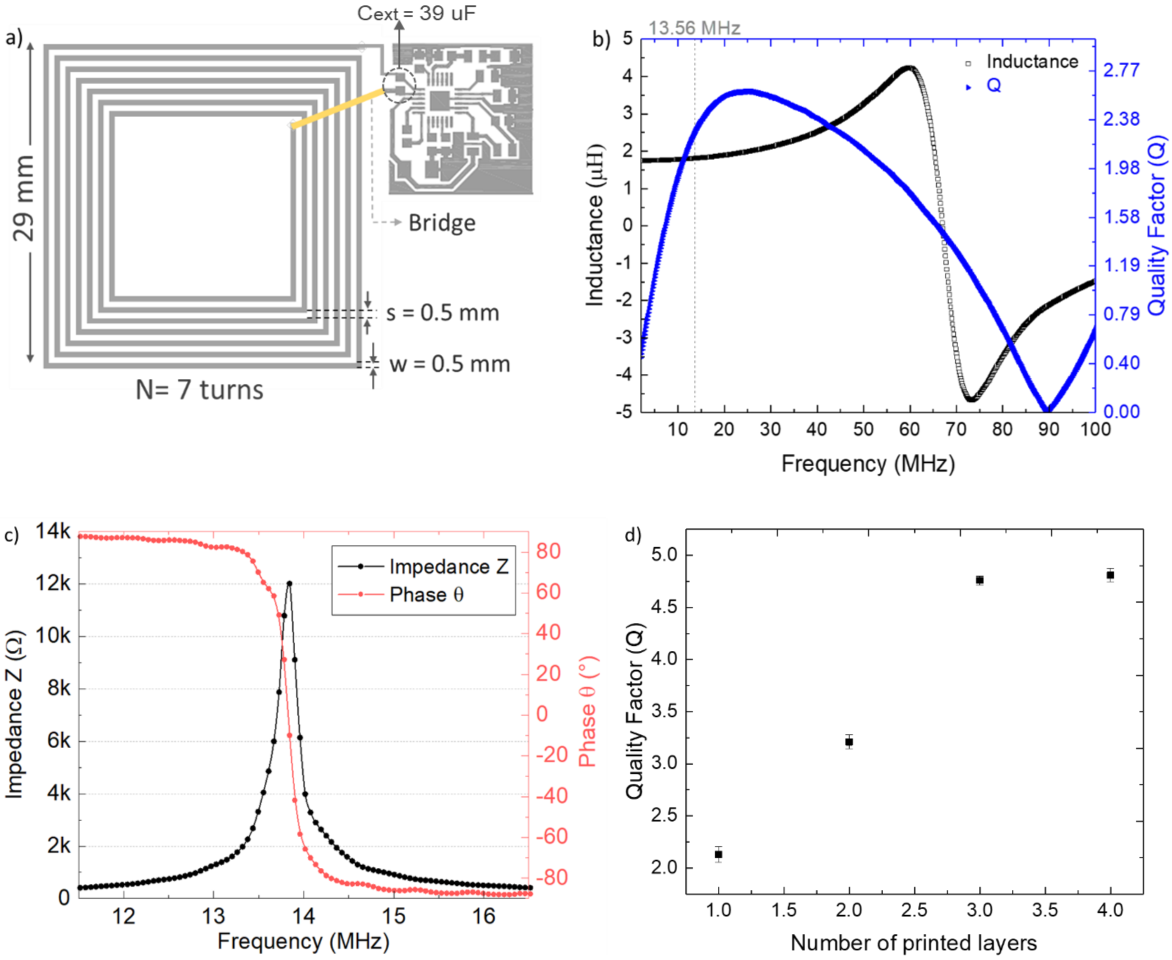

Figure 3-3 (a) Dimensions of the designed NFC tag antenna. (b) Frequency response of the screen-printed NFC coil before bounding a chip and electronic components (c) Frequency response of the NFC tag after bonding a chip and external capacitor. (reproduced from (163)) (d) Effect of increasing number of printed layers on the quality factor of the printed planar coil.

Table 3-1 Geometries and simulation (Sim.) and measured (Meas.) values for the inductors.

Design No.	No. of Turns	Length (mm)	Width (mm)	w and s (mm)	L (Sim.)	L (Meas.)	R (Meas.)	Q (Meas.)
1	6	44	44	1	1.83	1.82 ± 0.17	68.28 ± 4.2	1.93 ± 0.013
2	7	29	29	0.5	1.83	1.78 ± 0.11	46.32 ± 3.5	2.13 ± 0.011
3	7	26	26	0.4	1.79	1.79 ± 0.13	71.22 ± 3.95	1.6 ± 0.011
4	8	19	16	0.2	1.83	-	124.53 ± 5.1	-

Figure 3-3 (b) and **(c)** show the frequency response of this antenna before and after attaching the C_{ext} and the NFC transponder respectively. A 1.78 ± 0.11 µH at 13.56 MHz was achieved, close to the simulated inductance value. The measured quality factor at the same frequency was $Q = 2.13 \pm 0.071$. Increasing the number of printed layers has improved the quality factor as it is shown in the **Figure 3-3(d)**. Printing three layers has increased the quality factor to 4.73 and it was not practically possible to increase it further because adjacent tracks were merging. This effect is like coffee-ring effect in inkjet printing which states that a new layer of printing spread slightly and make a wider line compared to the previous printed layer. So, three layers of printing was the optimum value we could achieve.

3.2.1 Challenges in electrical bonding and mechanical stability

It is worth mentioning that first we demonstrated the application of the NFC RFID tag for health and food quality monitoring by integrating the NFC transponder and antenna on a rigid FR-4 substrate in (164, 165) and then on flexible polyimide substrate in (166, 167). **Figure 3-4 (a), (b)** shows these two versions. However, both the rigid and flexible tags developed earlier, followed the conventional copper etching method used for standard PCBs.

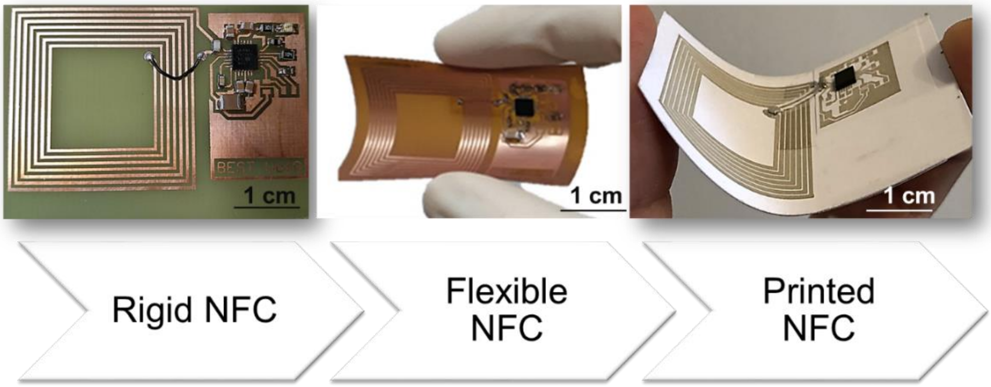

Figure 3-4 The NFC transponder based (a) rigid, (b) flexible, and (c) screen-printed smart tag.

This approach leads to generation of electronic waste (e-waste) due to the unused etched copper. This could be overcome by additive manufacturing (AM) route, which has been used to develop different types of NFC smart tags (168, 169). This approach commonly uses Thin Shrink Small Outline Package (TSSOP) for electrical bonding of NFC chips. However, electrical bonding of the SMT Integrated Circuits (ICs), resistors, capacitors is still challenging as the mechanical stability of the adhered components is not comparable with the rigid and flexible copper-etched tags. Moreover, there is no literature which has described the challenges for mounting the VQFN (Very thin Quad-Flat No-leads) packaged SMT components on the screen-printed tags. **Figure 3-4(c)** shows our final screen-printed tag, designed after optimizing the antenna structure, substrate and electrical bonding materials. The selection of suitable substrate and adhesive materials are discussed in the following section.

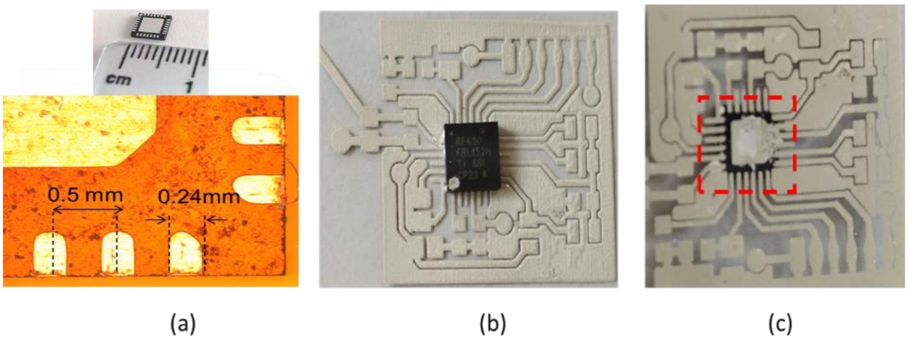

Figure 3-5 The NFC transponder IC: (a) The overall size of the chip including dimension of the pins and distance between them, (b) ground plane is mounted on the printed layer of the smart tag, and (c) spread of the silver paint after curing. (Courtesy: The bonding for screen-printed tags was led by Dr. Moupali Chakraborty)

The substrate was first chosen as polyester with 70 μm thickness, and silver patterns of the earlier designed circuit is screen printed on it. The NFC transponder RF430FRL152H (170) is a VQFN packaged 24 pin tiny chip with the dimension of 4 mm × 4 mm and with a spacing of 0.25 mm between the two consecutive pins as shown in **Figure 3-5(a).** Since this package has a high contact area compared to leaded surface mount components the mechanical robustness is higher when the chip is attached to the substrate. At first, silver paint is used as the adhesive to bond the IC on the silver pattern. As the adhesive in semi liquid state, small misalignment in the mounting process of the IC could result in an erroneous connection between the printed patterns. To overcome this issue, the ground plane (**Figure 3-5(b)**) of the NFC transponder is mounted efficiently by depositing a little amount of conductive adhesive like silver paint (16) with the help of a needle on the substrate, and thereafter cured at 80 ^{O}C. However, the paint spreads at the time of curing and makes an undesirable connection between the pads of the IC. **Figure 3-5(c)** shows the spread of the paint.

To overcome this issue, silver filled conductive epoxy (171) is used and as it is more viscous than silver paint, the spread of the adhesive is eliminated. However, electrical bonding of the pins of the VQFN-packaged IC with the adhesive is one of the big challenges. Each pin is 0.25 mm apart from the consecutive pin, thus, they need to be connected to the printed pattern under the microscope. Manual deposition of the adhesive with the gap of 0.25 mm distance is extremely crucial. Even after the efficient deposition on the substrate as well as on the wall of the IC, deposition of the epoxy at the junction of the IC and the substrate was not fully achievable. Apart from the that, another challenge can be seen as the mechanical stability of the bonding with the conductive adhesive. The small SMD (0603 packaged) parts like capacitor can be bonded strongly (Fig. 5), however, the electrical bonding with the IC is not robust enough to sustain the rough handling. Bending of the substrate can detach the IC from the printed pattern and may damage the printed layout permanently.

The above-mentioned challenges can be overcome by using Sn42/Bi57.6/Ag0.4 low-temperature solder paste, where hot air at temperature of 138 ^{O}C is used to melt the solder paste to build the electrical bonding. However, the Polyester (70 µm) substrate cannot sustain in more than 80 ^{O}C temperature. These challenges lead to the matt photo paper substrate (120 gsm) which can sustain the melting temperature of the solder paste. The solder paste provides a strong mechanical stability of the IC with the paper. Besides, the paper also has the advantage of being biodegradable.

In this process, solder paste is added on the ground plane of the IC, then IC is aligned precisely, and hot air is blown over it at 140 ^{O}C temperature. Once the ground plane is fixed, a little solder paste is applied uniformly in each side of the square IC and there is no need of applying solder paste in each pin of the IC. Because of the hot air, the solder only makes the bonding with the silver tracks, not with the paper substrate, thus minimizes the probability of shorting consecutive pins of the tiny IC. The hot air should be blown perpendicular to the IC, otherwise the chip shifts its place and makes an unwanted connection between the tracks.

3.3 Antenna Characterization

Tagformance Pro HF is used to characterise the paper based printed NFC tag (**Figure 3-6 (a)**). The equipment works like a vector network analyser to measure the effect of the designed NFC tag on the input impedance of a reader antenna. The reader antenna was Voyantic C60 antenna which is a loop (diameter 60 mm) antenna with 4 turns.

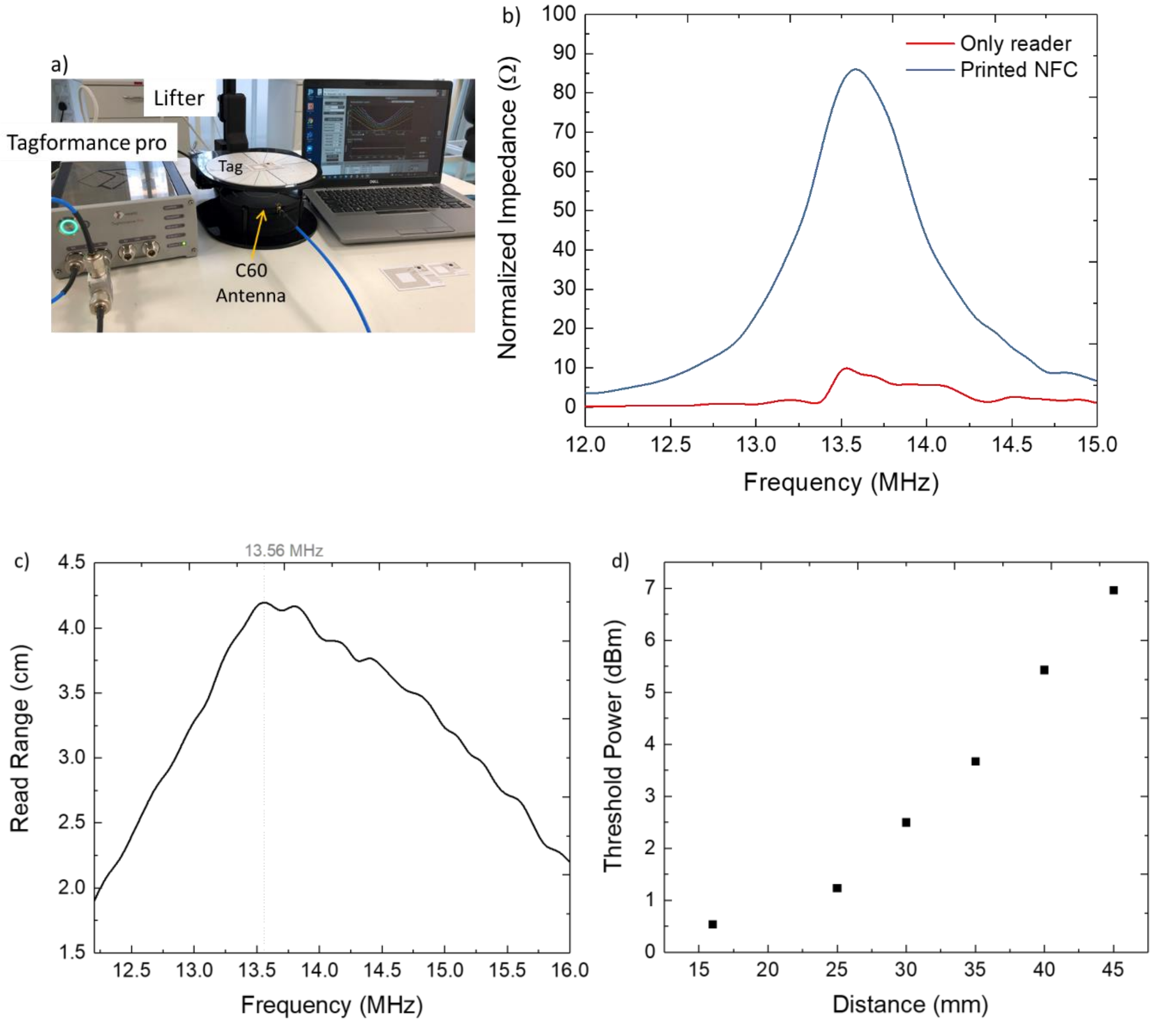

Figure 3-6 (a) Tagformance Pro setup to characterise NFC tags (b) Normalized input impedance of the reader antenna with and without present of the printed tag on the lifter. (c) Reading range of the printed tag at resonant frequency (13.56 MHz) and a range of frequency round this value (12-16 MHz) covering a part of HF band. (d) Sensitivity of threshold power to distance between the tag and the reader antenna.

When no tag is in the vicinity of the C60 the quality factor of the antenna is 38.1. The input impedance of the reader antenna is measured with and without presence of the tag in its proximity (**Figure 3-6(b)**). The peak of impedance happened at 13.6 MHz very close to

13.56 MHz which is the frequency the tag was designed for. The reading range of the tag in practice is shown in **Figure 3-6 (c)** when the output power of the reader set at 0 dBm.

The threshold power (P_{th}) is measured to provide information about sensitivity of the tag to the distance from the reader antenna. To do so, the tag was placed on the lifter to adjust the measurement distance. During this measurement, the tag communicates with the reader while the distance between the tag and the reader is increasing from 16 mm to 45 mm. As it is shown in **Figure 3-6(d)** the threshold power increases as the lifter goes up. The initial output power was 0 dBm and frequency was swept from 10 MHz to 20 MHz with 10 kHz resolution. The lowest output power in each distance happened at 13.6 MHz which is the optimal operation frequency of the tag. In the case that an NFC enabled smartphone is using as the reader the power that the phone can provide to this unit defined the reading range of the tag.

The data of the transponder RF IC is sent back via RF signal in a process called load modulation. Load modulation takes in the alternation of the antenna load that leads in a change of the backscattered signal. **Figure 3-7** shows the relation between the variation in P_{th} and the load modulation of the printed tag at 13.56 MHz at 16 mm distance from the reader. It shows the threshold of transmitted power to have the strongest modulation. The load modulation also is function of magnetic field intensity (**Figure 3-7**) of the tag to evaluate the tag performance on all power levels to find the optimal power level to communicate with the tag.

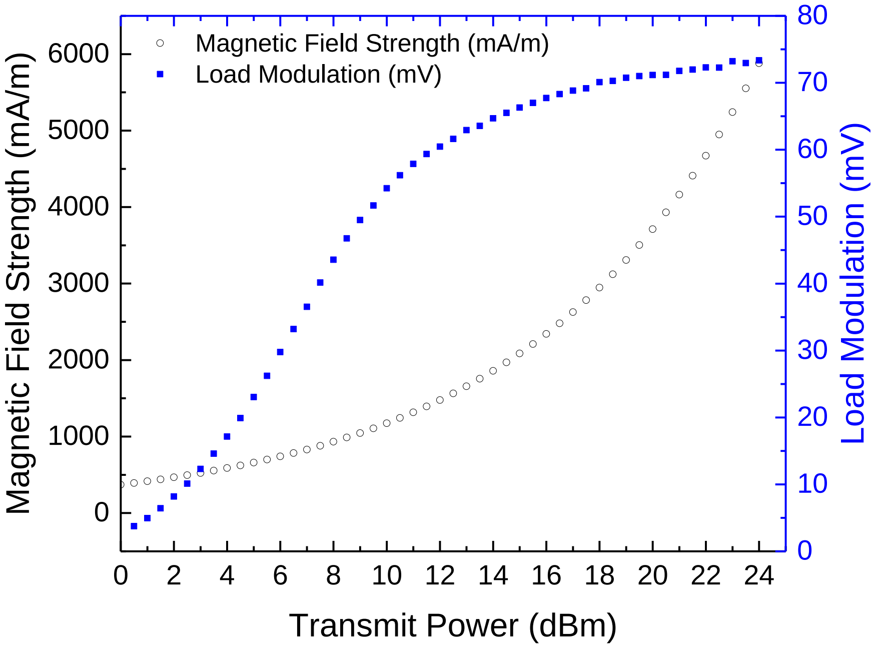

Figure 3-7 Threshold power of the printed tag as a function of magnetic field intensity and load modulation at 13.56 MHz

3.4 NFC tag for sensing applications

3.1.1 Sensing NFC tag as smart bandage[2]

The circuit and system-level block diagrams of the developed smart bandage system are shown in **Figure 3-8(a),(b)** respectively. The fabrication and characterization of microfluidic strain sensor and the resistive temperature sensor were presented in our article (166). Both sensors are based on conductive poly (3,4-ethylenedioxythiophene) polystyrene sulfonate (PEDOT:PSS) polymer. The sensors and NFC tag were integrated on wound dressing to obtain a wearable system. Since both sensors were flexible, the realised bandage was fully flexible suitable for healthcare application such as assessment of wound status or respiratory diseases where wireless monitoring via wearable strain (e.g., respiratory volume) and temperature sensors is critical. The sensors can be operated and read from distance of 25 mm with a user-friendly smartphone application developed for powering the system as well as real-time acquisition of sensors data.

The designed antenna was connected to the RF analog front-end of the chip using ANT1 and ANT2 pins. The interface between the sensors and the RF430FRL152H transponder was done through a resistive sensor bias interface, which makes use of an internal 14-bit sigma-delta analog-to-digital converter (ADC) and a Programmable Gain Amplifier (PGA) featuring a very high-impedance input and a programmable gain combined with full offset compensation, very low offset drift, and low noise. As shown in **Figure 3-8(a)**, a voltage divider was implemented as the conditioning circuit for the strain sensor. One end of the resistor R_1 was connected to VDDSW, a regulated output voltage of $V_{ddsw}{\sim}1.5\ V$ with a current up to 450 µA that the chip is able to provide under an adequate EM field from the RFID reader. The other end of R_1 was connected to the strain sensor (R_{strain}) and one of the analog-to-digital converter inputs (ADC0). The other terminal of R_{strain} was grounded to SVSS with the virtual ground setting enabled on the chip. Using this option, the voltage at SVSS is raised to approximately 125 mV to prevent minor errors due to the non-linear behavior of the ADC near the ground.

---

[2] This subsection is adopted from publication #5

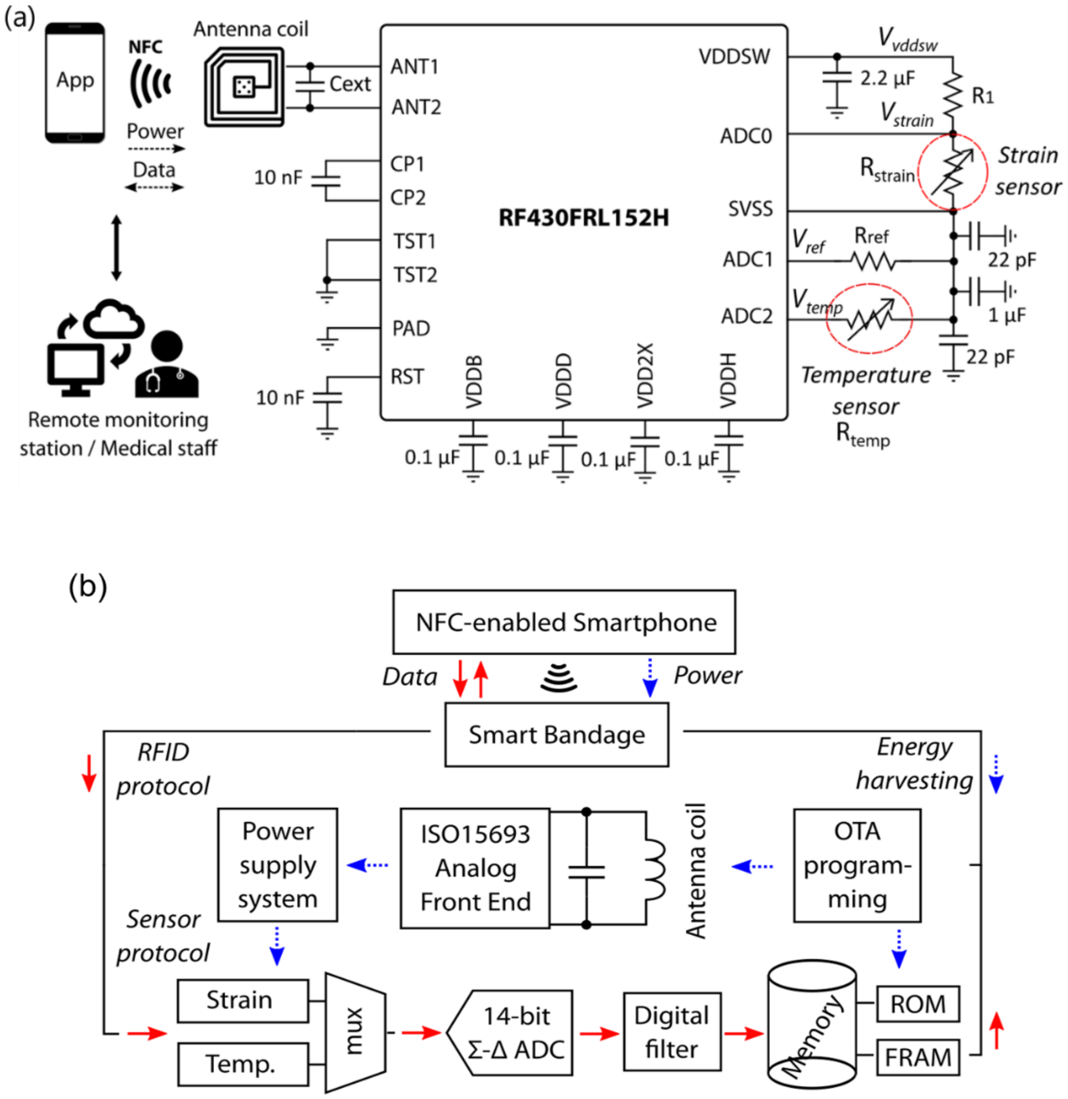

Figure 3-8 Circuit (a) and system-level (b) block diagram of the developed smart bandage for wireless strain and temperature monitoring (166).

The temperature sensor (R_{temp}) was connected between ADC2 and SVSS. To get more accurate temperature measurements, a reference resistor ($R_{ref} = 100\ k\Omega$) was also used and connected between ADC1 and SVSS. The temperature measurement approach was different from the strain sensing in that a current source was applied to the temperature sensor (ADC2) and reference (ADC1) pins to determine their resistances. Typically, an output current of ~2.4 µA is applied by the chip to both pins according to the specifications, but the exact amperage of this current source can vary from part to part. Using the R_{ref} known resistor, the accurate current level driven through both pins can be determined, and thus a precise voltage calculation can be performed. For the sampling of both sensors, a digital decimation filter was programmed after the 14-bit sigma-delta converter to achieve noise reduction. It consisted of a cascaded integrator-comb (CIC) filter whose decimation ratio was programmed to 256. This resulted in a conversion time of 128 ms, which was quick enough for our application. The chip was programmed to sequentially sample the voltage values at the three ADC pins, storing them in specific locations of the FRAM. Those memory locations were then accessed by the *SensAble* application (developed by Dr. Pablo Escobedo) through NFC commands, and the voltage values were converted to strain and temperature values using the abovementioned calibrations. To develop the program that conducts the readout routine in the chip, Code Composer Studio (CCS) version 7.4 was used. The firmware was uploaded to the RF430FRL152H ROM using Over the Air programming (OTA) through a TRF7970A RFID reader from Texas Instruments.

As conditioning stage for the strain sensor acquisition, a voltage divider circuit was implemented whose output was connected to one analog-to-digital converter input (ADC0). The calculation of the actual voltage present on the ADC0 was done using equation (3-6):

$$V_{strain} = \frac{\frac{ADC0data}{2^{14}-1} \times 0.9\,V}{G_{PGA}} \tag{3-6}$$

where ADC_0 *data* is the value stored into memory by the ADC, G_{PGA} is the gain of the Programmable Gain Amplifier (PGA), and 0.9 V is the upper rail of the ADC, whether the virtual ground is enabled or not (full voltage swing is from 0 V to 0.9 V). In our case, no amplification was needed for the strain measurements (G_{PGA}=1). The value of R_1 in the voltage divider was selected considering the resistive characterization of the strain sensor to accommodate the output of the voltage divider within the input range of the ADC. A value of $R_1 = 130\ k\Omega$ was selected to harness the full span of the ADC up to 0.9 V after considering the resistive values that can be obtained from the strain sensor. The internal ADC of the NFC chip has 2^{14} = 16384 possible output codes or steps, meaning that the resolution is 0.9V/16384 = 55 μV per step. Considering a resistance range up to 180 kΩ as per the strain sensor characterization, this means that the ADC is able to detect resistance changes with a minimum resolution of ~11 Ω, which is good enough for the given application. **Figure 3-9(a)** shows the output voltage of the implemented divider (i.e., the input voltage of the ADC0) as a function of the strain resistance value. Once this voltage was acquired by the ADC, the resistive value of the sensor can be directly calculated as:

$$V_{strain} = V_{vddsw}\frac{R_{strain}}{R_1+R_{strain}} \Rightarrow R_{strain} = R_1\frac{V_{strain}}{V_{vddsw}-V_{strain}} \tag{3-7}$$

For temperature sensing, the sensor (R_{temp}) was connected between ADC2 and SVSS. and a reference resistor ($R_{ref} = 100\ k\Omega$) was connected between ADC1 and SVSS. The voltages present at inputs ADC1 and ADC2 are computed within the microcontroller in a similar way to that presented in Equation (3-7):

$$V_{ref} = \frac{\frac{ADC1data}{2^{14}-1}\times 0.9V}{G_{PGA}} \; ; \; V_{temp} = \frac{\frac{ADC2data}{2^{14}-1}\times 0.9V}{G_{PGA}} \qquad (3\text{-}8)$$

From the reference voltage, the exact current value driven through both pins can be determined as:

$$I_{out} = \frac{V_{ref}}{R_{ref}} \qquad (3\text{-}9)$$

Finally, the resistance value of the temperature sensor can be obtained as:

$$R_{temp} = \frac{V_{temp}}{I_{out}} \qquad (3\text{-}10)$$

Equation (3-10) shows another way to directly calculate the sensor resistance by combining the previous expressions:

$$R_{temp} = \frac{ADC2result}{ADC1result} \times R_{ref} \qquad (3\text{-}11)$$

Afterwards, the actual temperature value was calculated from the resistance value as per the calibration presented. **Figure 3-9(b)** shows the temperature voltage V_{temp} as a function of the temperature sensor resistance R_{temp}. For the temperature measurements, the gain of the PGA was set to the maximum possible value (G_{PGA}=8) to increase the resolution at full-scale. Therefore, the maximal full-scale range, in this case, was reduced to $V_{FS} = V_{REF} \times (1/G_{GPA}) = 0.9V \times (1/8) = 0.1125\,V$. Considering the 16384 possible output codes of the ADC (14 bits), the resolution is, therefore, 0.1125 V/16384 = 6.9 µV per step. Considering the resistance range associated with the temperature variations, this means that the ADC can detect resistance changes with a minimum resolution of ~10 mΩ, which is translated to 0.88 ºC in terms of temperature. This detection limit is lower than the minimum difference between two detectable consecutive temperature values that can be obtained by the sensor.

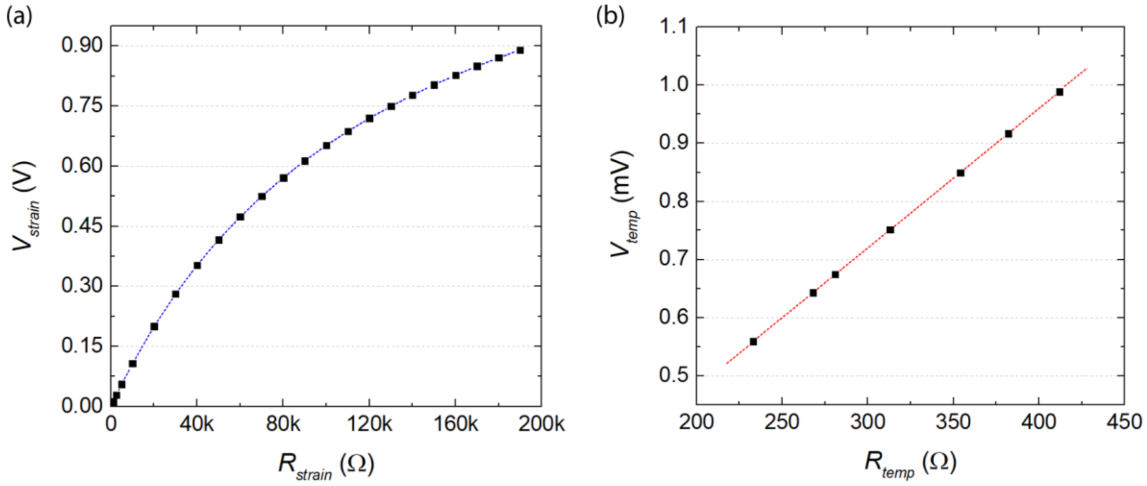

Figure 3-9 (a) Output voltage of the implemented voltage divider (V_{strain}) as a function of the strain sensor resistance (R_{strain}). (b) Temperature voltage (V_{temp}) as a function of the temperature sensor resistance (R_{temp}) considering a typical output current of 2.4 µA applied to the ADC2 pin (166). Reproduced from (166).

The typical reading distance of an NFC tag is between 1 cm and 5 cm if the tag is scanned with a mobile phone as a reader. Several factors can affect the performance, including the technology within the NFC chip, the tag antenna size and design, the tag quality, and the reader antenna. In flat position and with the Xiaomi Mi6 smartphone used in this work (Xiaomi Inc., Beijing, China), a maximum vertical reading distance of 43 mm was achieved. Although the previous results were taken off-body, no major differences were observed in the reading distance when the tag was attached to different human limbs. For instance, maximum reading distances of 41 mm, 38 mm and 25 mm were measured with the tag attached to a thigh, a wrist, and a thumb, respectively.

Finally, the smart bandage was tested as a proof of concept on a medical anatomic mannequin for wireless monitoring of chest expansion and contraction during respiration using the strain sensor (172, 173). This can be of interest for wireless assessment of respiratory diseases such as asthma. For that purpose, the smart bandage was placed on the chest of a cardiopulmonary resuscitation (CPR) manikin, as observed in **Figure 3-10(a)**. The CPR manikin was used in conjunction with GlasVent, which is a low-cost, emergency, DIY (Do it Yourself) ventilator developed by our group (174). As shown in **Figure 3-10(a)**, GlasVent is an automated version of manual resuscitator device commonly known as bag mask ventilation (BVM or AMBU bag), which is widely used by clinicians prior to initiating the mechanical ventilation. With the smart bandage fixed to the chest, respiration could be wirelessly monitored using the *SenseAble* app by the upward and downward slopes of the relative resistance associated with inhalation and exhalation (chest expansion and contraction), as observed in Figure **3-10(b,c)**.

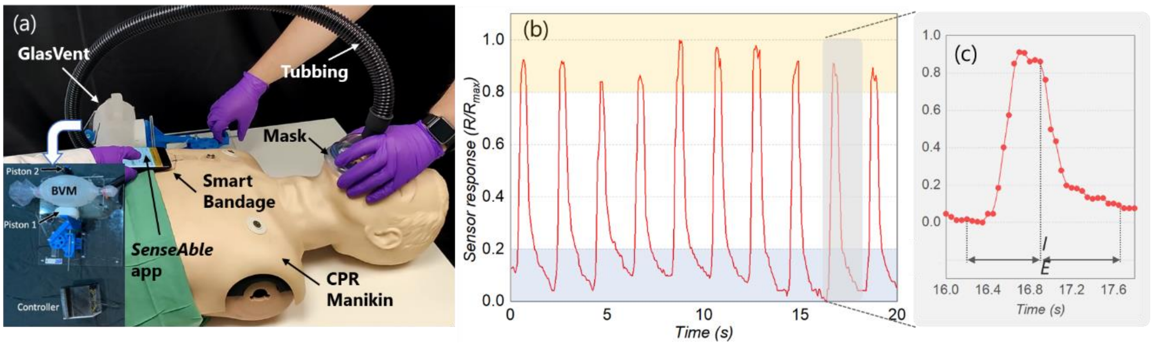

Figure 3-10 (a) Experimental setup for the wireless monitoring of chest expansion and contraction during respiration using the smart bandage and the GlasVent ventilator in a medical CPR manikin; (b) Sensor response over time measured by the smart bandage associated with the inspiration and expiration cycles during respiration. In this case, the resistance of the strain sensor was normalized to the maximum resistance obtained during the chest expansion due to inhalation; (c) Detailed view of one breath cycle consisting of two-time components, i.e., inspiration (I) and expiration (E). (166)

3.1.2 Sensing NFC tag for qualitive food monitoring[3]

In most food packages, the presence of undesired gases could indicate the loss of quality and shelf-life of the food, as they originate from the oxidation of the content or the microbial growth (175). While spoilage can take many forms, inflated or swollen food packages serve as the beacon of microbial contamination. This is known as Blown Pack Spoilage (BPS) (176). In vacuum-packaged meat, BPS is mainly caused by *Clostridium estertheticum* and it is characterized by the production of large volumes of gas (mainly carbon dioxide, CO_2), which result in severe distention of the packaging (177). Therefore, swelling might be an initial sign of harmful bacterial activity within the food package, leading to discoloration, nutritional loss, and final spoilage (178). In the literature, the vast majority of food monitoring methods are based on measuring the gas concentrations emitted from food in a container, thus utilizing chemical sensors (179, 180). In this case, our proposed smart sensing tag detects strain and temperature to monitor packaged food quality (167). In the particular case of RFID/NFC tags for temperature/strain sensing (181-183), the use of physical sensors to detect the distention of the packaging as a result of BPS is lacking in the current state of the art. In this context, the bulge in a food package can be detected using an appropriate strain sensor integrated with it. Temperature is another crucial factor in determining the shelf-life of food products. Temperature alterations can provoke the growth or survival of food-spoilage microorganisms and bacteria (184). Although there can be several other

---

[3] This subsection is adopted from publication #4

parameters (e.g., chemical parameters such as pH) to evaluate the food quality, temperature and strain are two critical physical parameters that can indirectly help to evaluate the quality of food thus, the sensor tag presented here (**Figure 3-11(b)**) consists of strain and temperature sensors only. The sensors are similar to the one which were used in previous section.

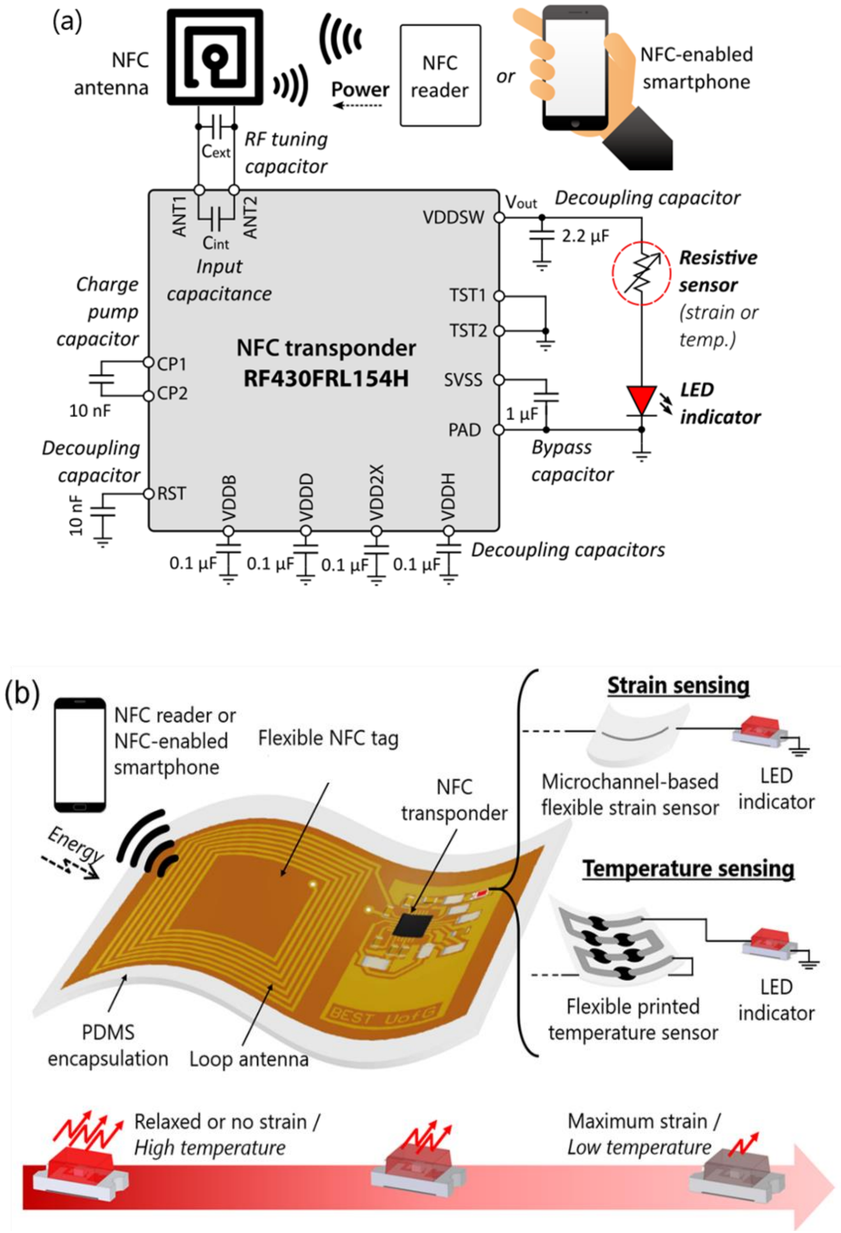

Figure 3-11 (a) Schematic circuit diagram of the passive NFC tag for strain or temperature sensing. The sensor is connected in series with an LED indicator whose intensity is modulated according to the sensor value. (b) Overview of the smart label with NFC-based sensing system. (167)

The response of the sensors at different temperature/strain conditions can be quantified and displayed using standard seven segment displays. However, for food packaging applications the exact values of temperature or strain are not always needed, as often the goal is only to identify if the food is stale or not. Given this scenario, a simple indicator to warn only when the packed food is stale can be more cost-effective. For this reason, the smart tag presented here includes an LED connected in series with the developed resistive sensors (**see Figure 3-11(b)**). The varying resistance of sensors modulates the light intensity of the LED indicator, thus allowing the user to detect the state of food in a visual way. The NFC tag serves as the energy harvester to power the whole tag, thus allowing its operation using any NFC-enabled smartphone.

The developed NFC tag and sensor along with a LED were integrated as shown in **Figure 3-11(a)**). Apart from them the external capacitor, some other passive components were integrated as well. The sensors response was correlated with the intensity of the LED, which acted as a visual indicator. Upon introduction of the reader (NFC-enabled smartphone), the LED glowed and its intensity was related to the amount of strain experienced by the sensor. In this case, the NFC antenna was acting as the energy harvester for the whole tag. The change in the intensity of the LED was visible and distinguishable visually. However, for characterization purposes, the intensity of the light was measured using a lux-meter mobile application for the different strain conditions. As a semi-quantitative system, the presented solution is apt for large scale deployable packaging tags. **Figure 3-12(a)** shows the light intensity of the LED connected in series to the sensor for different strain values. The intensity of the sensor decreased significantly when the sensor was in a bent condition, which could be the case for a faulty or inappropriate packaging. The brightness of the LED was highest (~67 Lux) for relaxed or no strain condition, whereas the intensity was significantly low (~8 Lux, causing the LED to be virtually off) for the highest strain condition. **Figure 3-12(a)** also shows a decrease in the intensity of the LED brightness with the increase of the bending angle. Similar to the mentioned above case, the optical intensity response of the temperature sensor is shown in **Figure 3-12(b).**

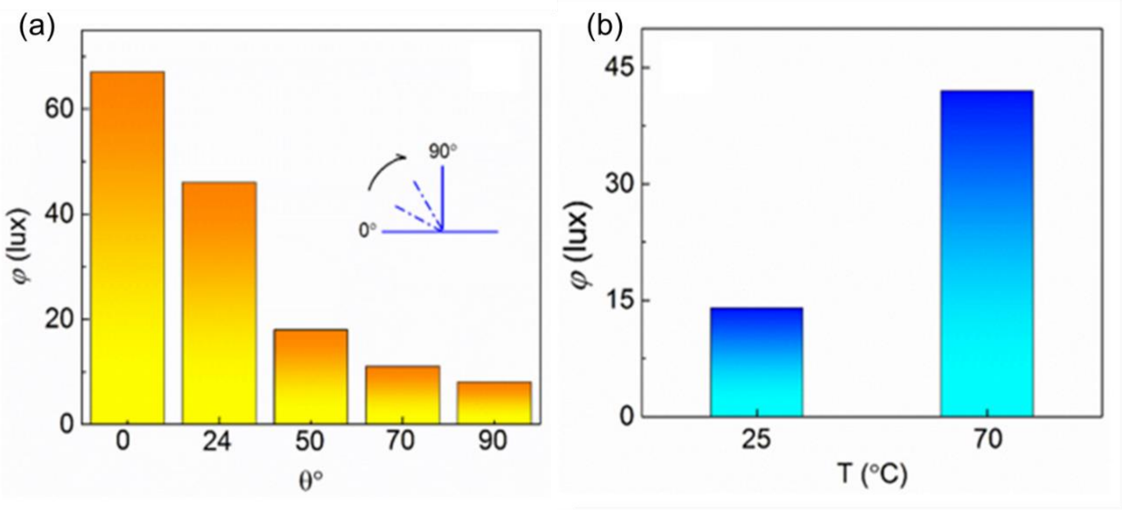

Figure 3-12 (a) The intensity of the LED (φ) with strain on the sensor due to different angle of bending (θ). (b) Optical intensity (φ) of LED due to different temperature (T). Adopted from (167).

As a proof of concept, the potential applicability of the proposed NFC-based strain sensor has been tested on a meat package for the detection of BPS, as illustrated in **Figure 3-13**. For this purpose, it was first checked that the LED was ON with maximum brightness upon approach of an NFC-enabled smartphone when the meat was fresh and suitable for consumption (i.e., the package was not inflated). Afterwards, the meat package was kept in a non-refrigerated atmosphere to accelerate its spoilage. A few days later, the package started swelling due to the BPS effect. After the distention of the meat package caused by the spoilage, the LED did not turn on anymore upon approach of the reader smartphone to the tag, since the strain sensor resistance had increased upon bending, which indicated that the meat was unfit for consumption.

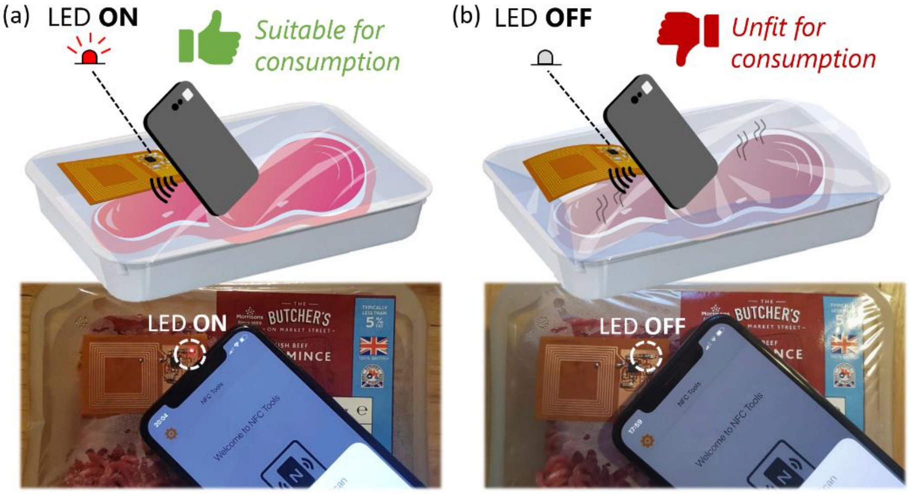

Figure 3-13 Example of the application showing the NFC strain sensor tag attached to a food package for meat spoilage detection. The LED will be ON if the product is suitable for consumption, or OFF if the food is unfit for consumption (163).

This simple experiment shows the possibilities of the proposed sensing tag, thus opening new avenues in this field. While the simplicity of the resistive-based sensing mechanism does not provide a quantitative correlation between the sensor response and the exact spoilage status, the threshold detection is enough for the proposed application in the field of BPS. This simplicity allows, on the one hand, the use of any NFC-enabled smartphone as energy harvester without the need for an ad-hoc application. On the other hand, the NFC chip does not need to include any internal Analog to Digital Converter (ADC) module, making the design compatible with a wider range of commercially available NFC chips, which usually do not incorporate any type of sensor front end interface.

Similar to the strain sensing arrangement, the temperature sensor was also connected in series with the LED indicator. Similar to the previous case, the NFC link acted as an energy harvester, i.e., the antenna was used to provide power to the tag upon approach of the reader. The resistance of the fabricated temperature sensor decreased with the increasing temperature. Hence, for a higher temperature, the optical intensity of the connected LED increases. In the presence of an NFC reader, the intensity of the LED varies depending on the temperature. The intensity at 70 ºC was measured to be ~42 lux whereas the intensity was ~14 lux at room temperature (~25 ºC). This sensor also can show in a semi-quantitative way the temperature of any package.

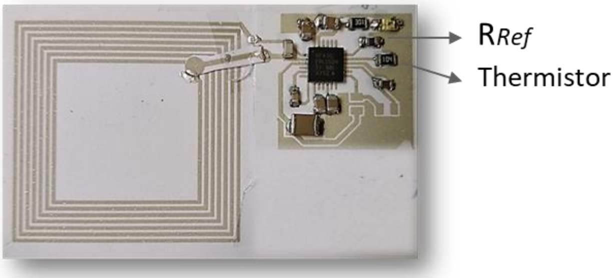

Figure 3-14 Temperature sensing NFC tag utilising off the shelf component as sensor

The PEDOT_PSS based temperature sensor was replaced by a 100 kΩ thermistor (Panasonic Negative Temperature Coefficient) as well as shown in Figure 3-14. A reference resistor ($R_{ref} = 100\ k\Omega$) was connected between ADC1 and SVSS for calibration purpose to increase accuracy of the reading. In this case, the thermistor can function accurately from -40 °C to 125 °C and provides accurate measurements within 0.5 °C.

3.2 Summary

This chapter presents the development of NFC based sensing tag, using the capability of the NFC RFID chip to integrate an external sensor to achieve a complete battery-less sensing platform. The main purpose of this work is to fabricate a cost-effective NFC sensing tag which is suitable for green electronic applications as degradable substrate. Additive manufacturing technique (screen printing) was implemented to reduce material waste (e-waste) associated with conventional copper etching for standard PCBs. Moreover, paper as low cost, easy to recycle and biodegradable substrate was chosen to reduce the cost of each tag. Different substrates have been used in order to realize the sensing tag. Paper was the best choice for realization of printed flexible tag as mechanical bounding of the chip on flexible substrates is challenging. Two flexible resistive sensors developed in the group were integrated to the NFC tag. The temperature and strain values of those flexible sensors were converted to voltage values and reading carried out by NFC enabled smartphone. The circuit layout was tailored by adding a LED as an indicator to monitor temperature and strain of food packaging.

Chapter 4. Antenna sensing using functional materials[4]

4.1 Inductor-Capacitor Resonant Tank based Printed Wireless Pressure Sensor on Electrospun Poly-L-lactide nanofibers

4.1.1 Introduction

In chapter 3, a conventional NFC tag structure was presented consisting of an inductive coil and a capacitance in parallel configuration. The capacitor was used to adjust the resonant frequency of the LC circuit in order to be 13.56 MHz compatible with NFC protocols. In some application such as epidermal and implantable wireless devices it is desirable to eliminate any electronic components such as a package NFC chip and surface mount capacitor. Besides, the IC increased the cost of each tag. To this end, a chipless LC circuit can be a reasonable alternative. The chipless LC tank consists of an inductor (L) to communicate to the reader through magnetic coupling and a planar interdigitated capacitor. The capacitor is a replacement for the off-the-shelf capacitor where it is sensing element as well because it is printed on a sensitive substrate (PLLA).

In this work, an interdigitated capacitive (IDC) sensor is developed on electrospun PLLA nanofibers-based substrate and connected in parallel with a planar inductor forming a LC circuit to realise wireless pressure sensor. The LC circuits is designed to resonate at 13.56 MHz. The IDC configuration of the sensor offers long stability, high accuracy, and lower power consumption with respect to typical parallel plate capacitors (PPC) (185, 186). The PLLA nanofibers-based substrate used here, to realise the IDC capacitive sensors, offers better conformal contact with the skin and improves sensitivity under the pressure due to its piezoelectric property. It provides a direct interaction between the sensing elements and environment (74). Moreover, due to the uni-polarization of PLLA nanofibers during electrospinning, change in the permittivity of the dielectric layer is expected when the

---

[4] Section 4-1 is extracted from publication #2 where F. Nikbakhtnasrbadi is the main contributor. The simulation, fabrication and characterization of the LC tank were carried out by F. Nikbakhtnasrbadi. Section 4-2 is extracted from publication #3 where characterization and simulation were carried out by F. Nikbakhtnasrbadi.

external stimuli are applied, which allows linear responses of capacitive response over a wide range of 0-16 kPa. This pressure range is of the same order as one used in commercial bandages for compression therapy and therefore, we have integrated the presented LC tank-based sensor on a compression bandage to demonstrate its potential use in the online monitoring of sub-bandage pressure. The application of optimum pressure by the bandage, together with the electroceutical arrangement facilitated by the piezoelectric PLLA substrate, could accelerate the cell regeneration and hence wound healing.

The wireless mechanism of presented sensor is based on inductive coupling in near field region. Applying an external pressure leads to changes in the capacitance of IDC on PLLA substrates, and thus the resonant frequency of the LC circuit is altered as a function of applied pressure. The sensing data is encoded through backscattering power without using an IC to record and process data. The electrospinning and screen-printing, used here to develop entire sensor, offers a unique possibility for low-cost and mass production of devices with high reproducibility.

4.1.2 Sensor design and fabrication

Initially, the LC tank was simulated using the Advanced Design System (ADS) momentum simulator (Keysight Technologies, Santa Clara, CA, USA). **Figure 4-1** shows the schematic of the parallel LC tank. The dielectric constant of the nanofibers substrate was calculated as 3.5 in simulation for frequency of 13.56 MHz. However, the dielectric constant was almost constant in the frequency range of 10-14 MHz. Square-shape PPCs with 1 cm dimensions and dielectric layer of the nanofibers with the thickness of 40 µm were printed to measure the dielectric constant. The approximate thickness of printed layers and surface roughness were considered in the simulation. **Table 4-1** shows the physical dimensions of the LC tank.

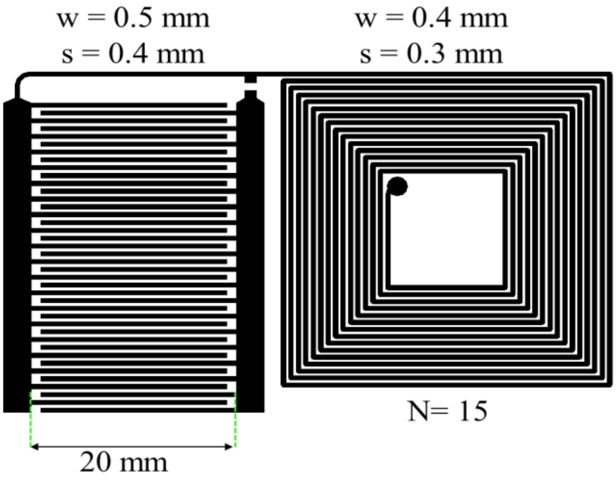

Figure 4-1 Schematic of the parallel Inductor-Capacitor tank.

Table 4-1 Physical dimensions of the IDC and planar inductor

IDC		Inductor	
Parameter	Value (mm)	Parameter	Value (mm)
Length of fingers	20	Width of line	0.4
Width of fingers	0.5	Spacing	0.3
Number of fingers	40	Number of turns	15
Interspacing	0.4		

Figure 4-2 shows the fabrication steps for realising LC tanks using screen printing. Commercial stretchable silver paste (PE873) (Dupont, UK.) with a sheet resistance of 110 mΩ/sq was used to print planar LC tank, which consists of a rectangle inductor connected in parallel to an IDC. A bridge was also printed separately to make a connection between both ends of the inductor. The silver paste has good electrical conductivity in DC and high-frequency range and can be printed and cured over various polymeric substrates at low temperatures (i.e. 100-160 °C for 2-10 mins) as per the supplier datasheet. The electrospinning method allows fabrication of a thin membrane of well-aligned PLLA nanofibers. The membrane is highly flexible and has a porous structure that can interact well with soft human tissue because of conformability, breathable and non-toxic character. The preparation of PLLA nanofibers will be explain in following section. The silver paste used

in this work, also has an appropriate viscosity to establish good adhesion with the nanofibers after thermal curing. The IDC pattern was printed on the nanofibers, whereas the inductor was printed directly on a PI sheet. Since the nanofibers have piezoelectric properties, only IDC is printed on PLLA nanofibers membrane to develop the pressure sensor. The inductor was printed on the PI sheet to isolate it from the electric charge generated by PLLA nanofibers. Thus, the effect of pressure on the performance of the coil antenna is negligible. We also printed several inductors on PI sheet using inkjet method and noted that the quality factor of inkjet-printed inductor is much lower than the one realised using screen printing. In fact, the quality factor with 5 layers of inkjet printed inductor can be attained with just one layer of screen printing structure. So, inkjet printing seems time consuming and costly compared to screen printing. Besides, the ink used for inkjet printing is less viscous compared to the paste used for screen printing. As a result, the inkjet printed structures may see the ink seeping through the PLLA nanofibers and it was also spreading on the PI substrate. On other hand, with high viscosity of the paste used in screen printing we did not experience such challenges and therefore the current work was carried by screen printing method. The screen printer employed is a semi-automatic screen-stencil printer (model C920, Aurel Automation, Italy) with a flat bed. The screen used to print the pattern is 400 mesh thread per centimeter. The density of mesh is adequate to print a fine pattern with a resolution of less than 100 µm. The interconnect was also printed on the PI sheet to connect the inner end of the inductor to the capacitor. After printing, the samples were cured in an oven for 20 mins at 130 °C. **Figure 4-2(e)** shows the photograph of the LC tank configuration consisting of a planar inductor connected in parallel to an IDC printed on flexible PLLA nanofibers.

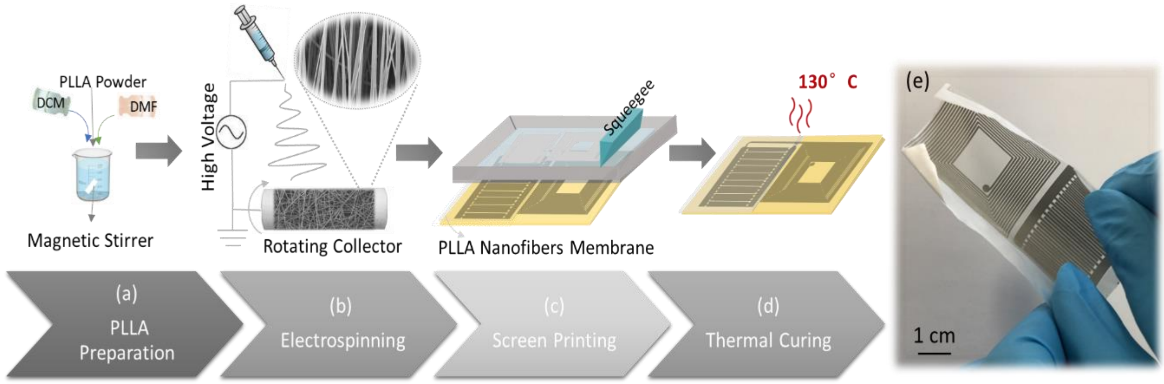

Figure 4-2 Schematic showing the fabrication of pressure sensor based on printed LC Tank on Electrospun PLLA Nanofibers. (a) polymer solution preparation (b) electrospinning of PLLA solution, (c) screen printing LC structure and (d) curing the devices at 130 °C for 20 mins. (e) Optical image of printed LC tank on PLLA nanofibers.

4.1.2.1 Preparation of PLLA nanofibers[5]

A 4 wt% PLLA solution was prepared by dissolving PLLA pellets (Corbion, The Netherlands) in a 1:4 ratio DMF and Dichloromethane (DCM) (Sigma-Aldrich, UK) mixed solvent for 10 h. The solution was stirred at room temperature by a magnetic stir bar at 300 rpm (**Figure 4-2(a)**). The multi-layered membrane of the PLLA nanofibers mat, was fabricated by electrospinning of the PLLA polymer solution at 15 kV and a flow rate of 0.5 ml/h with a drum speed of 3000 rpm (**Figure 4-2(b)**). The electrospun nanofibers were annealed in an oven at 100 °C for 4 hours.

4.1.2.2 Cell growth, adhesion and proliferation on electrospun PLLA nanofibers[6]

Human dermal fibroblast (adult) (HDFa) cells were used to assess the biocompatibility and suitability of the PLLA nanofibers as wound dressings. First, HDFa cells were cultured at 37 °C in a 5% CO_2 incubator at log phase growth using Medium 106 (fibroblasts) complemented with a low serum growth supplement containing fetal bovine serum, basic fibroblast growth factor, heparin, hydrocortisone, and an epidermal growth factor. The cultured HDFa cells were then seeded on the electrospun PLLA nanofibers in 24 well plates at a cell density of 1×10^4 cells /sample. After a 1 h resting phase to allow cells to settle on the fibers, the desired volume of culture media was added to each well before incubating at 37 °C in a 5% CO_2 incubator for 1, 3 and 5 days. The culture medium was replaced every 2 days.

Prior to incubation the electrospun PLLA nanofibers were cut into circular shapes that fit into the 24-well plates. The electrospun PLLA nanofibers were then immersed in 70% v/v ethanol for 12 h followed by washing with sterile PBS (X3) and sterilized under UV light for 1 h on each side. Following sterilization, the electrospun PLLA nanofibers were hydrated by immersing the scaffolds in Medium 106 for 24 h at 37 °C. After 1, 3 and 5 days of incubation, respectively, cell morphology attachment and growth were assessed using SEM microscopy (SU8240 Hitachi High-Tech). For this, HDFa cells grown on the electrospun PLLA nanofibers were rinsed with PBS (X3) and fixed using 2.0% glutaraldehyde in phosphate buffer saline (PBS) at 5 °C for 12 h. The fixed cell/nanofiber samples were then

---

[5] Dr. E. Hosseini fabricated PLLA nanofibers mat using electrospinning method

[6] This study was carried out by Dr. S. Dervin

dehydrated by submerging each sample in a series of ethanol solutions (50%, 60%, 70%, 80%, 90%, and 100% ethanol, respectively) for 15 min and then air dried. Prior to SEM imaging the samples were Au coated.

4.1.2.3 LC tank fabrication

The morphology of the piezoelectric PLLA nanofibers that are well aligned and densely packed (average diameter of 800 nm) is imaged using a high-resolution scanning electron microscope (SEM) (SU8240 Hitachi High-Tech) as shown in **Figure 4-3(b).** Also, the SEM image of the conductive composite paste (**Figure 4-3(c))** shows the stretchable silver paste contains micrometer-sized silver flakes. The average thickness of the single-layer printed line on PI sheet was 10.83 ± 0.65 μm with a conductivity of 1.1×10^{6} *S/m*. The optical microscopy images of a corner of inductor traces and the finger of IDC respectively in **Figure 4-3(d),(e)**, show the resolution of screen-printed structures. It is worth mentioning that due to the high density of PLLA nanofibers and high viscosity of paste, the latter did not seep through the substrate.

The crystallinity of the electrospun nanofibers was investigated using X-ray diffraction (XRD) (PANalytical X'Pert PRO MPD diffractometer). **Figure 4-3(f)** shows the XRD pattern graph of electrospun PLLA nanofibers before and after annealing. Only one sharp diffraction peak at 2 theta of about 16.5° was observed. This peak corresponds to the crystalline planes of (200) and (110) of PLLA and confirms the piezoelectric β-phase of PLLA nanofibers (187, 188). The result confirms that the electrospinning process could control the crystalline structure of PLLA effectively by aligning molecular chains in the fibres. This is due to the ejection of the polymer solution under pressure through the narrow nozzle and presence of high electric field in the electrospinning process. The peak intensity and the crystallinity of nanofibers increased by annealing, as shown in **Figure 4-3(f).**

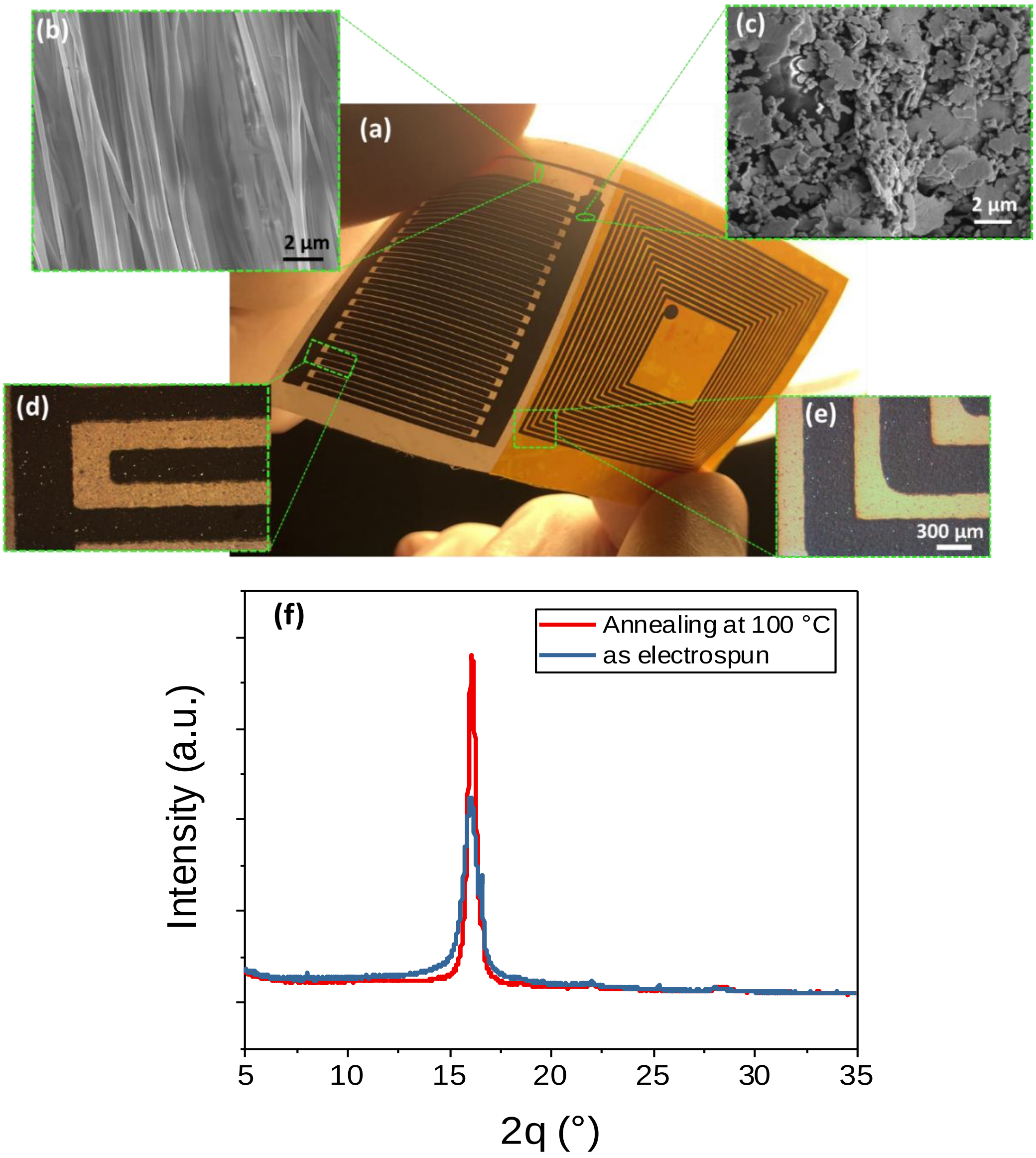

Figure 4-3 Screen-printed flexible LC tank: (a) Photograph of the fabricated LC tank, (b) SEM image of the PLLA nanofibers, (c) SEM image of the stretchable silver paste consists of micrometer-scale silver flakes. (d-e) Optical microscopy images of a finger of the IDC and the corner of inductor lines respectively. (f) XRD pattern of electrospun and annealed PLLA nanofibers. (Courtesy: The XRD analysis was done by Dr. Ensieh Hosseini).

4.1.3 Results and Discussion

Inductors and capacitors were characterized separately using an Agilent 4294A Precision Impedance Analyzer along with a 42941A impedance probe kit (Keysight Technologies, Santa Clara, CA, USA). The capacitor was positioned and fixed to a 1004 miniature single point load cell. Pressures in wide range of 0-16 kPa were uniformly applied to the sensing capacitors using a load cell. A small rectangular glass slide as a moving plate has been used to apply the required pressure. This plate was controlled with a motorized stage with a resolution of ~0.1 mm. The fixed and the moving plates were paralleled to guarantee a uniform contact pressure. Both plates were covered by a thin dielectric pad with relative permittivity close to 1 to prevent forming parallel plate capacitor between the moving plate and the sensing capacitor once they are in contact. The parameters of interest measured using an Agilent 4285A Precision LCR Meter were recorded using a custom-made LabVIEW program.

Tagformance Pro HF (189) was used to characterise the LC tag by monitoring the shift of resonance frequency with the change in pressure. Tagformance Pro is a measurement system for evaluating the performance of UHF RFID, HF RFID, and NFC transponders. The equipment works like a vector network analyser capable of measuring impedance and frequency responses when Passive Measurement is chosen in the measurement menu. Prior to measurement, calibration was performed using 50 Ω terminator and open load following the software instructions. The termination is included in the Tagformance Pro HF kit. This wireless method could be helpful for sub-bandage pressure and wound monitoring and can be easily implemented, without causing wound agitation.

4.1.3.1 Performance evaluation of capacitive sensor

Three samples were fabricated following the procedure explained in the previous section. The IDCs were characterized using the Impedance Analyzer along with the impedance probe kit to cover frequency of interest (13.56 MHz) as well as self-resonant frequency. The self-resonant frequency was in the order of 60 MHz which is much higher than the working frequency. **Figure 4-4(a)** shows the 17.9 ± 0.8 pF capacitance of the IDC samples obtained at 13.56 MHz which is in good agreement with the simulated value (19 pF). It was observed that the capacitance was almost constant over 0 Hz-25 MHz frequency range. Since 13.56 MHz is far below the self-resonant frequency, and is within the region of flat response of the proposed design, the device can be used for pressure measurements. The pressure sensing principle relies on the fact that the applied pulse pressure changes the relative permittivity of the PLLA nanofibers, leading to the capacitance change. The change in capacitance will shift the resonance frequency of the parallel inductor, which can be monitored wirelessly through the inductive coupling with an external reader coil. **Figure 4-4(b)** shows the capacitor response when pressures applied on the surface of the IDC varied between 0 to 16 kPa at a frequency of 1Hz. The change in capacitance was constant and stable at each pressure values, which were repeated four times. To evaluate if the change in capacitance is due to the PLLA piezoelectric substrate, a number of capacitors were also printed on PI and no notable capacitance change was observed with application of pressure.

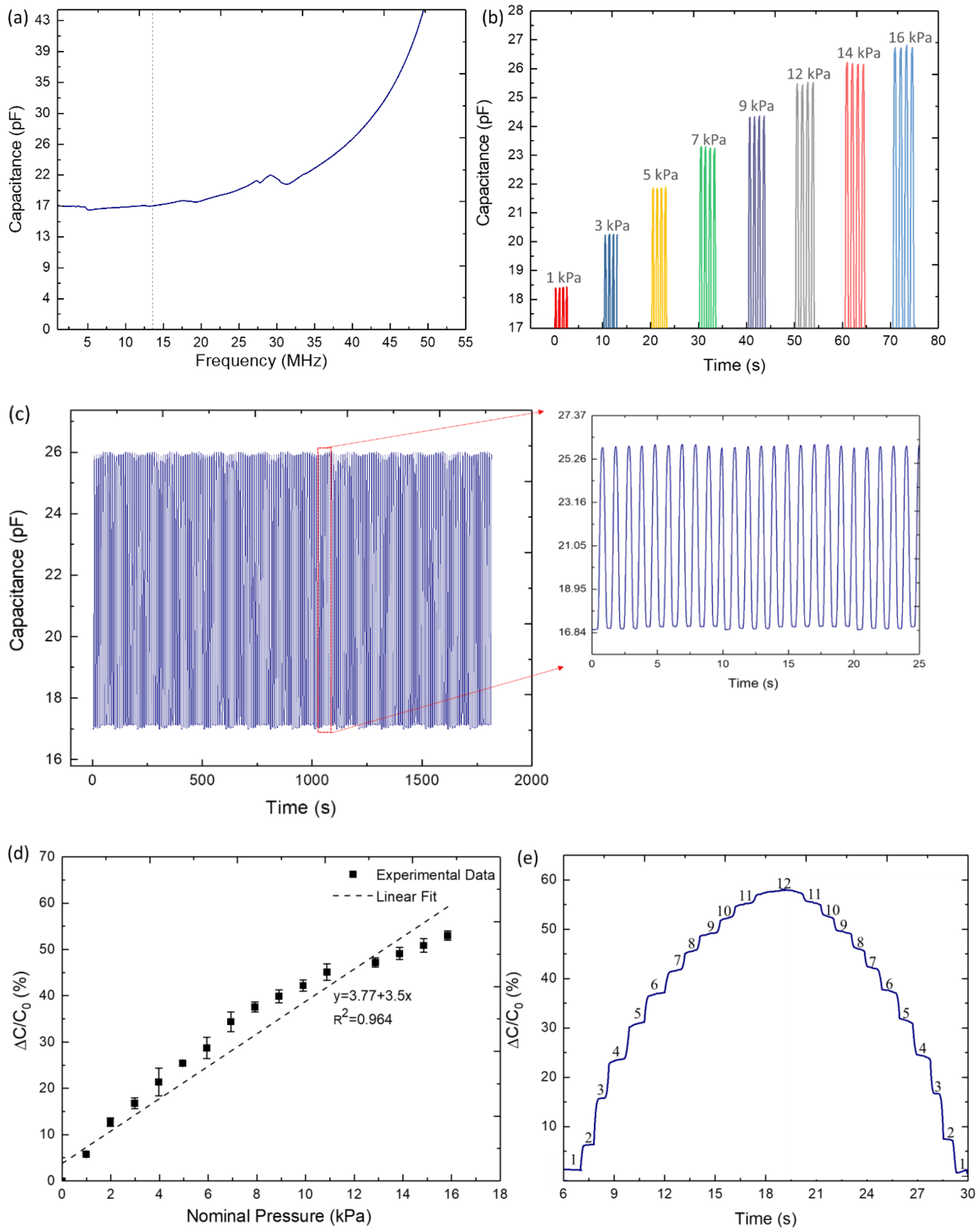

Figure 4-4 (a) Frequency response of the interdigitated capacitor with sweep from 4 Hz to 55 MHz. (b) Response of the IDC to various pressure values at 1Hz. (c) Cyclic response (over 1800 cycles) of the IDC to 14 kPa pressure, showing the durability and stability of the device (inset shows the 25 s of the capacitance response after 1000 cycles). (d) The capacitance variation and sensitivity of the IDC to pressure variation. (e) Capacitance response of the IDC to stepwise loading-unloading pressure from 0 to 12 kPa.

To demonstrate the durability and robustness of fabricated sensors, they were also subjected to loading-unloading cyclic pressure for up to 1800 cycles at 14 kPa. As shown in **Figure 4-4(c)**, the sensor exhibited a long fatigue life with stable variation under cyclic loading and releasing. **Figure 4-4(d)** shows the change of the capacitance of IDC as a function of applied pressure for three fabricated sensors. The low variation of the response among these sensors confirms the uniformity attained with the controlled fabrication process described above. The sensitivity of presented piezoelectric IDC was calculated with normalized change of capacitance divided by the nominal applied pressure ($(\Delta C/C_0)/\ \Delta P$). As shown in **Figure 4-4(d)** the capacitance variation of the IDC increases linearly under the applied pressure with an average sensitivity of almost 3.5 Pa^{-1}. The capacitance response of the IDC to stepwise loading-unloading pressures (from 0 to 12 kPa) in **Figure 4-4(e)** shows the outstanding reliability with negligible hysteresis effect.

4.1.3.2 Characterization of Planar inductor coil antenna

The measured average value of the inductance (7.75 ± 0.14 μH) at resonance frequency (13.56 MHz) is close to the simulated value (7.8 μH). The average value of resistance at that frequency was 367.42 ± 25 Ω (see **Figure 4-5(a)**). The slight deviation of resistance could be mainly due to the surface roughness of printed paste. The average quality factor achieved is 1.81, as shown in **Figure 4-5(b)**. The measured value is in good agreement with the simulation at 13.56 MHz. The quality factor of printed inductors is compared with conventional copper inductors with the same geometrical parameters and thickness of metal obtained through ADS simulation. This resulted in the quality factor of 65.72, which is far higher than the printed coil in the current work.

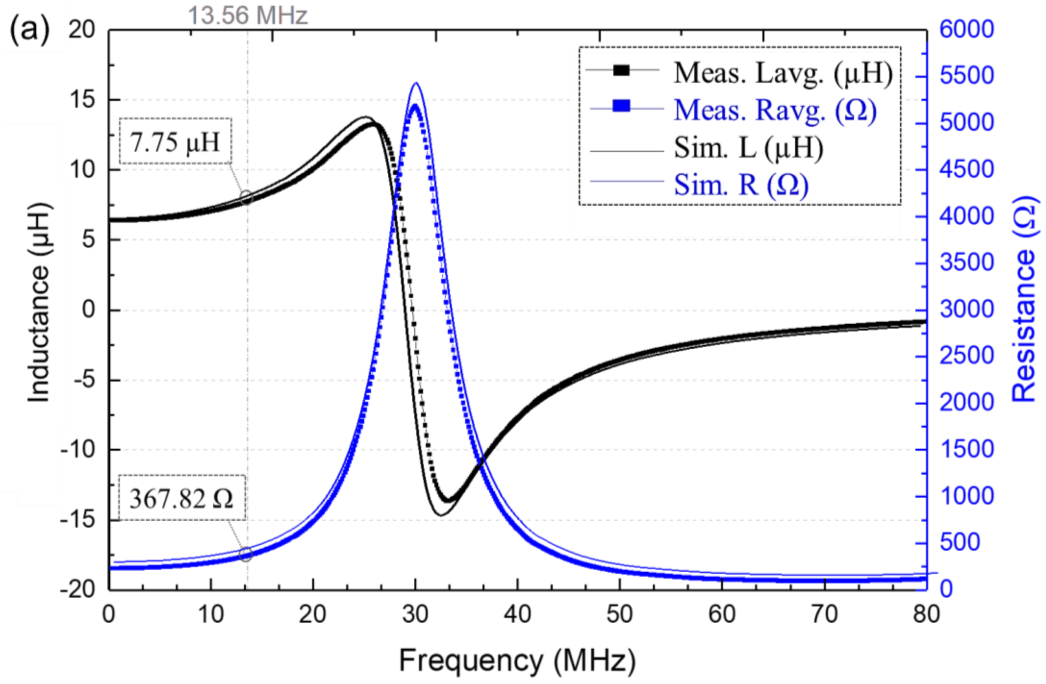

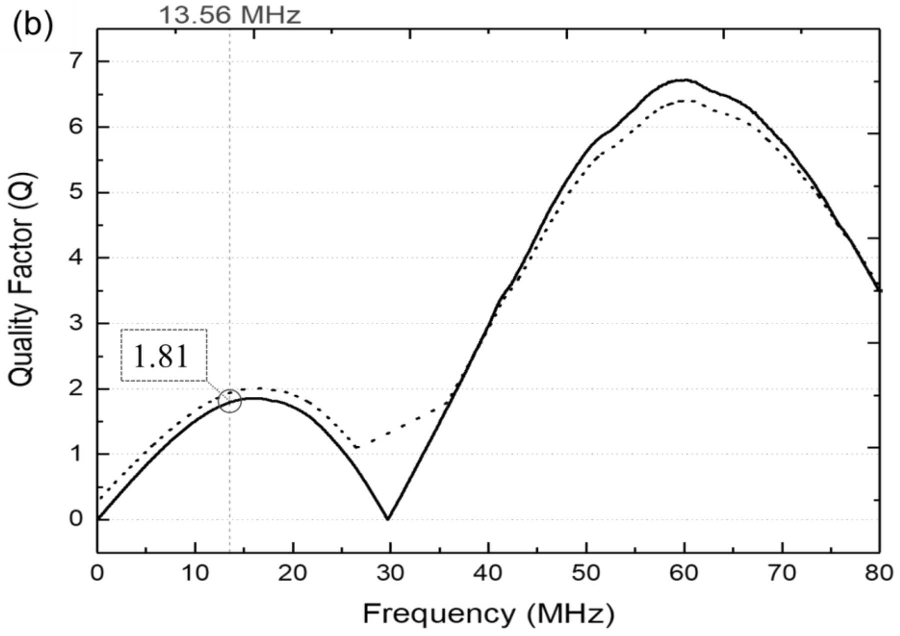

Figure 4-5 (a) Measured and simulated frequency response of the screen-printed inductors in terms of average inductance and average resistance. (b) Measured and simulated (dots) quality factor of printed inductor. (190)

The parallel LC tag resonates at around 13.61 MHz, which is close to the value obtained from the simulation (see **Figure 4-6(a)**). To use quality factor as a sensing measure, the variation of quality factor of the tag with applied pressure has been evaluated (see **Figure 4-6(b)**). The quality factor fluctuates around the initial value, so it does not indicate a periodic variation with respect to applied pressure. Here, quality factor is ${f_{res}}/{BW}$, where the f_{res} is working frequency and BW is half-power bandwidth, BW= $|f_2 - f_1|$. So, for the realised LC tag, the bandwidth is in the order of 648 kHz.

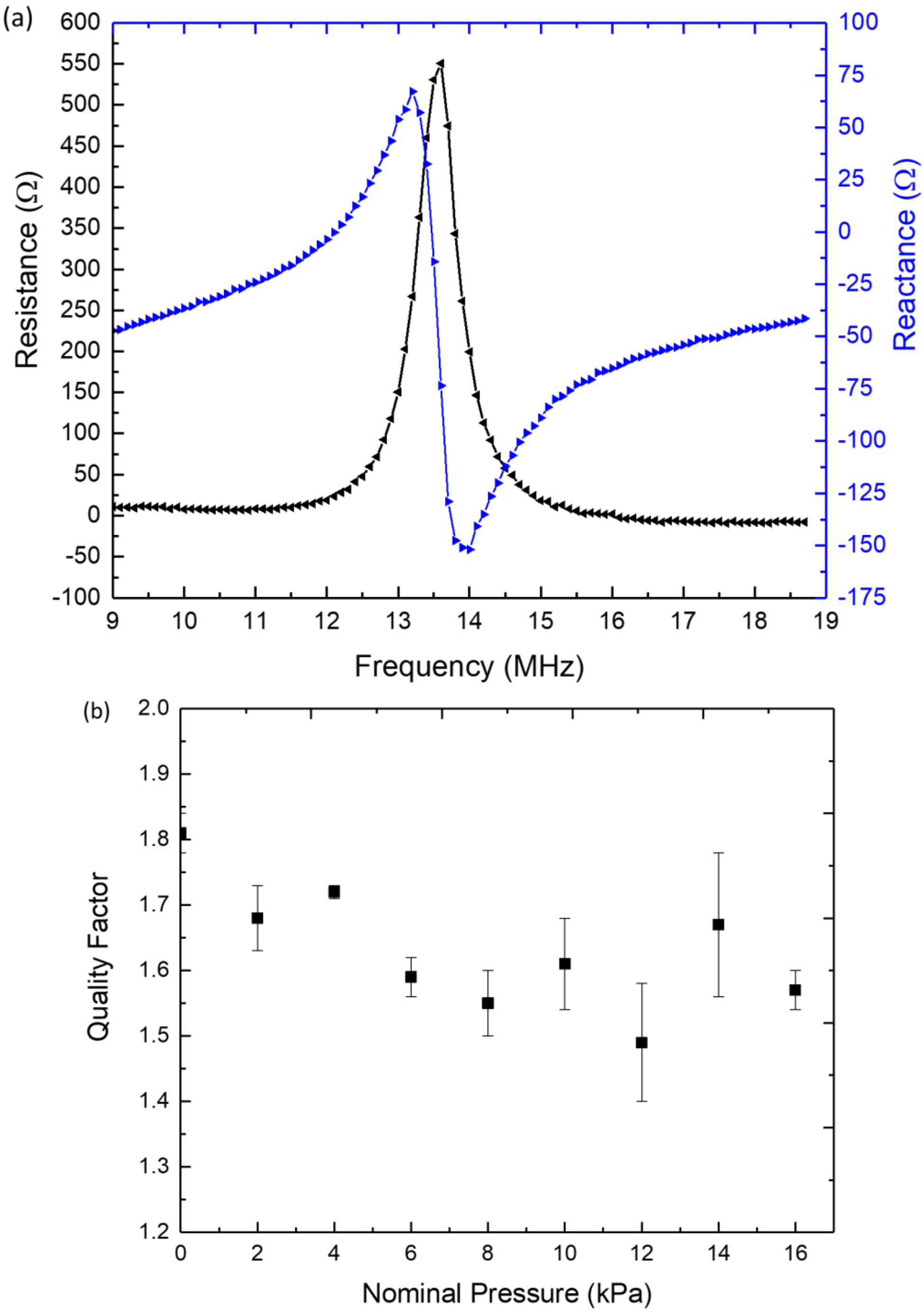

Figure 4-6 (a) measured resistance and reactance of the LC tag. (b) Quality factor of the LC tag function of applied pressure.

A reference measurement was also carried out to measure S11 of the reader antenna without a tag. This is used to calculate the normalized responses where the effect of the test antenna has been subtracted. The reader antenna was Voyantic C60 that is also included in the Tagformance Pro HF kit. **Figure 4-7(a)** shows the set-up. Voyantic C60 is a loop (diameter 60 mm) antenna with 4 turns. When no tag is in the vicinity of the C60, the quality factor of the antenna is 38.1. To carry out the measurements, the tag was held parallel to C60 at the centre, considering 16 mm distance between the reader antenna and the tag. This distance is suggested by Voyantic to minimise the error in the field strength while using C60 as the reader antenna. It is important to retain the distance and the angle constant as both parameters have an impact on the coefficient of coupling between the two coils. The frequency sweep range was 10 MHz - 30 MHz with 10 kHz resolution, which covers the working frequency of LC tag and sufficient margin around this frequency to monitor the effect of applied pressure on the resonant frequency. The transmit power in this case was set as 0 dBm.

4.1.3.3 Inductive telemetry system

Pressures (0-16 kPa) was applied on the capacitor at a frequency of 1 Hz. Once the magnetic field from the reader antenna is received by the LC tag, the shift of resonant frequency is considered as an indicator of applied pressure when the distance between both coil antennas is constant/unchanged. The normalised impedance of the printed tag at different values of pressure is shown in **Figure 4-7(a),(b)** in terms of resistance and reactance. The relation between change of impedance and resonant frequency shift is shown in **Figure 4-7(c),(d)** as a function of applied pressure. The effect of applied pressure can be seen in both magnitude (**Figure 4-7(c)**) and phase (**Figure 4-7(d)**) of frequency response. **Figure 4-7(e)** shows the linear curve fitting can represent the shift of resonance frequency while the pressure is increasing. Both magnitude and phase follow almost similar trend. However, the phase parameter expresses more reliable result as the standard deviation for different samples is negligible. The magnitude and phase of the resonance frequency decreases linearly by 0.1 ± 0.08 kHz/Pa and 0.11 ± 0.02 kHz/Pa, respectively in the range from 0-16 kPa.

Table 4-2 compares the response of our sensor with few relevant capacitive sensors reported for pressure monitoring (wired and wireless techniques). Among capacitive sensors reported for in kPa range operation, our sensor demonstrates highest sensitivity ($(\Delta C/C_0)/\ \Delta P$). Wireless performance also is good, considering that the frequency shift at reader depends on the mutual inductance and quality factor of the two coils. Since our coil is printed the quality factor is lower than the coils fabricated by metal traces. Thus, our sensor also demonstrates a good sensitivity to the pressure, in comparison with other non-printed and non-flexible wireless sensors.

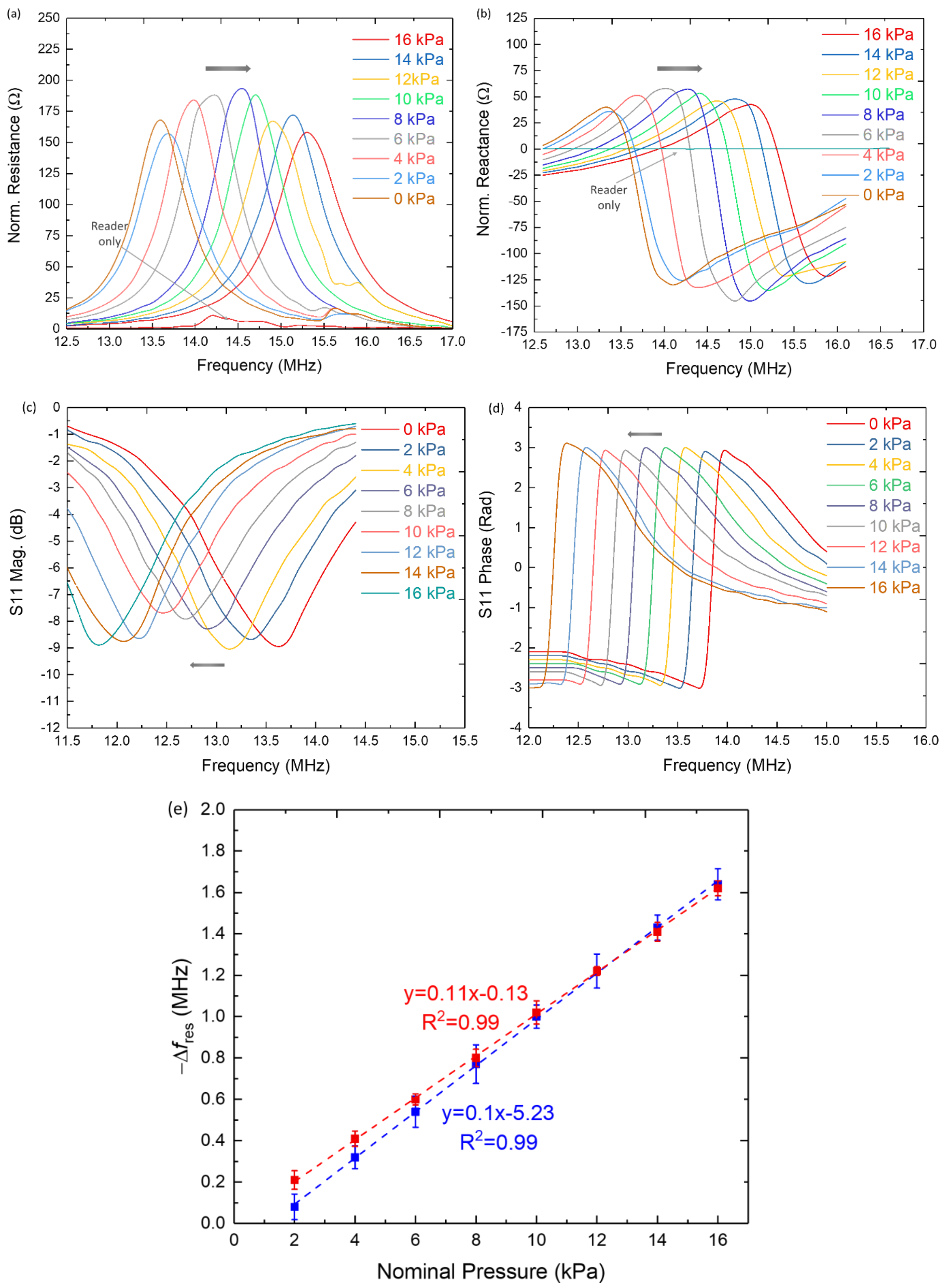

Figure 4-7 (b) Change in reader coil response associated with applied pressure: real and (c) imaginary part of the normalized. (d) frequency response of the reader coil (e) reflection coefficient phase shift. (f) comparison of frequency change considering two parameters: magnitude (red dotted line) and phase (blue dotted line) of the reader coil.

Table 4-2 Comparison between some capacitive pressure sensors

Sensing material	Type of capacitor	Pressure Range	Sensitivity		Frequency Range	Wireless	Reference
			$(\Delta f_{res})/\Delta P$	$(\Delta C/C_0)/\Delta P$			
Pyramid Microstructure PDMS	PPC	0-26 kPa	−2030 Hz/kPa	-	~725-800 MHz	Yes	(191)
Boron-doped silicon diaphragm	PPC	0-6.6 kPa	900 Hz/kPa	-	95-103 MHz	Yes	(192)
Single layer graphene	Coplanar IDC	0.11-80 kPa	-	0.01 kPa^{-1}	N/A	No	(186)
sandpaper-molded carbon nanotube/ PDMS composite	PPC	<5 Pa	-	9.5 kPa^{-1}	N/A	No	(193)
PVA-PDMS	PPC	0.1- 50 kPa	-	4 MPa^{-1} at 0.1 kPa	N/A	No	(194)
Pure PVDF nanofibers	PPC	1-6 kPa	-	0.02 kPa^{-1}	N/A	No	(195)
PLLA electrospun nanofibers	IDC	0-16 kPa	1200 Hz/kPa	0.035 kPa^{-1}	~11-14 MHz (HF band)	Yes	This work

4.1.3.4 Biocompatibility: Cell growth, adhesion and proliferation on electrospun PLLA nanofibers

SEM imaging was used to examine the cell growth, adhesion, and proliferation of HDFa cells grown on the electrospun PLLA nanofibers. As can be observed from **Figure 4-8**, the attachment of HDFa cells to the PLLA substrates is prominent after 24 h. The attached cells then started to noticeably spread across the scaffolds provided by the electrospun PLLA nanofibers, forming a monolayer like structure inter-cellular connections, and thus indicative of the strong cytoskeleton stretching. The observed cell behaviors on the electrospun PLLA nanofibers therefore confirm that the nanofibrous scaffolds facilitate cell adhesion/attachment and proliferation due to their porosity and high surface area and hence are suitable to accelerate the wound healing.

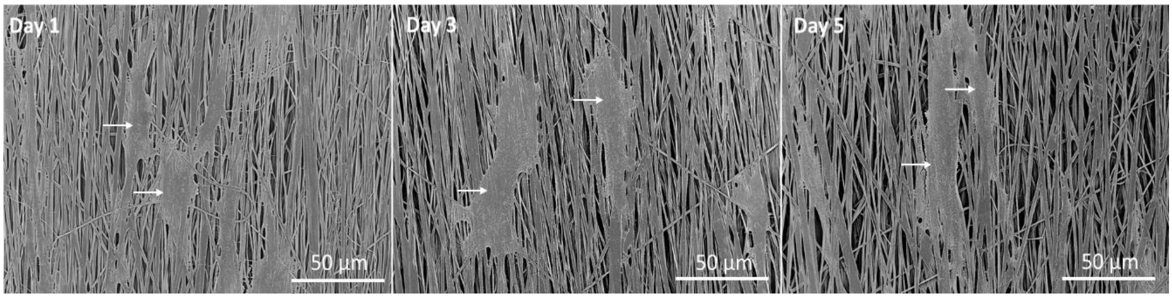

Figure 4-8 SEM images of HDFa cells cultured on well-aligned PLLA nanofibers after 1, 3 and 5 days. (Courtesy: The biocompatibility study was led by Dr. Saoirse Dervin and SEM images are taken by Dr. Dhayalan Shakthivel)

4.1.3.5 Application in wearable healthcare systems

The presented LC tag HF pressure sensor could find potential application in the area of accelerated wound healing and compression therapy. Compression therapy is an action of applying controlled pressure to the affected limb. Compression bandages are designed to boost blood flow and hence accelerate the wound healing. It also can be used to maintain constant pressure. There are several methods to apply negative pressure over the tissue (196); however it is crucial to monitor the extent of the applied pressure in a non-invasive method to improve the effectiveness of therapy. Swelling and bruising are very common side effects in pressure therapy techniques for which there is no accurate control over the applied pressure and can increase the risk of further harm. Thus, wireless pressure sensor worn under the compression bandage or integrated on the bandage to monitor regularly the pressure applied on the wound could be an interesting non-invasive solution for the patients with chronic wounds. As shown above the fabricated sensor showed linear sensitivity and repeatability in the pressure range of 0-16 kPa (0-120 mmHg) which covers the pressure range reported for compression therapy (197). Further, the performance of the developed wireless sensor was evaluated by placing it under a commercial compression bandage worn by an healthy adult volunteer around the elbow of healthy women wearing the sensor under a commercial compression bandage (#1523, Molnlycke) (see **Figure 4-9(b),(c)).** Four layers of the bandage were worn in a carefully controlled manner. **Figure 4-9(a)** shows the capacitance change and resonant frequency (wireless measurement) upon tightening the compression bandage. The modified Laplace equation (**Equation 4-1)** is used to calculate a gradual increase in pressure on the sensor over the clinically applicable range of pressures (198, 199).

$$Pressure\ (mmHg) = \frac{Tension\ (KgF) \times n\ \times K}{Circumference\ (cm) \times Bandage\ width\ (cm)} \qquad (4\text{-}1)$$

where the n is number of layers of bandage applied, K is constant of 4630 and $Circumference$ refers to the circumference of the limb. According to this law, the applied pressures by a bandage are a direct function of the number of layers and the tension of the bandage fabric itself, but reverse function to the width of the bandage circumference of the limb (198). These results show the possibility of predicting the pressure from the shift of frequency of reader antenna, provided the elasticity of the bandage and size of the limb are known. The reader coil in presented test can be substituted by a customized reader with a narrow bandwidth which can discriminate the different pressure ranges.

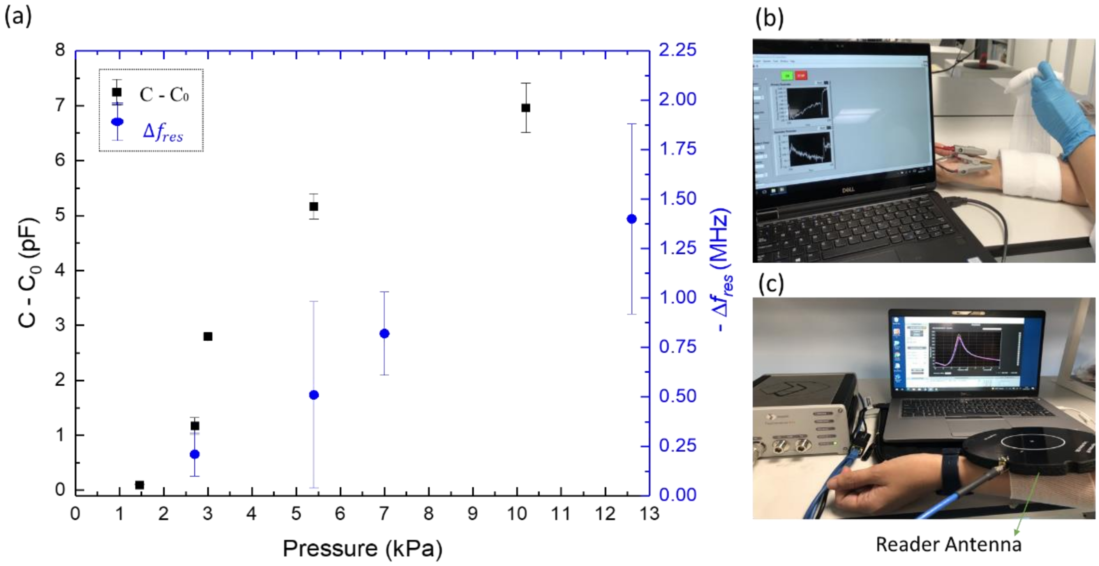

Figure 4-9 Potential application for the proposed LC tank to monitor pressure of compression bandage. (a) change of capacitance and frequency as a function of applied pressure. (b) setup to test the LC tank under compression bandage (with wire). The result was obtained using LCR meter controlled by a LABVIEW program. (c) Wireless setup to test the LC tank set under a compression bandage.

As compression bandage is in close contact to human body the change in temperature of the body may affect the performance of the capacitive sensor. In this regard, the capacitance of the capacitive sensor was monitored while the temperature was increased gradually from 25 °C to 40 °C. For this purpose, the sample was mounted on the PE120 stage (Linkam, UK) and the capacitance was recorded using a LCR meter controlled by a LABVIEW program. The temperature was increasing by 1°C each time. Only 2% change in capacitance was observed during this experiment however when the temperature was stabilized it reached to the original value. So, the performance of the capacitive sensor is very stable in case of any change in the human body temperature.

For application such as wound healing, the presented sensor is expected to be in direct contact with open wounds and hence the materials used should be biocompatible. To ensure the biocompatibility of the PLLA nanofibers and determine their suitability as wound dressings the morphology, attachment, and growth of HDFa cells was examined after 1, 3 and 5 days of culture using scanning electron microscopy. SEM observations revealed the attachment, growth and migration of the HDFa cells along the well-aligned axes of the PLLA nanofibers and presented no cytotoxic effect. Since PLLA nanofibers are biocompatible, the LC tag can be worn on the skin without the risk of skin agitation. Furthermore, some research suggests that the PLLA can promote wound healing by preventing bacterial infections (200) and due to its piezoelectric nature. With results showing durable sensing over long periods, the presented LC tag could provide a conformal and comfortable option for health monitoring.

4.2 Loop antenna as flexible temperature sensor

Herein, the work on printed loop antenna as a temperature sensor led by Dr Mitradip Bhattacharjee is presented briefly as this is another example of using a sensitive/functional material to add sensing element to an antenna. In case of LC tank, discussed in this chapter, the sensitive material was the substrate while in this case the main body of antenna (printed silver paste) itself is partially replaced by Poly(3,4-ethylenedioxythiophene): polystyrene (PEDOT:PSS) which is one of the most stable conductive polymers. PEDOT:PSS is sensitive to variation of temperature as it is discussed further in this subsection. The methodology, discussion and results are published in (46).

As shown in **Figure 4-10** the loop antenna which serves the dual function of temperature sensing and communication was printed on a flexible Polyvinyl Chloride (PVC) substrate which is commonly used for food packagings. The loop antenna is similar to a terminated folded dipole antenna which is terminated to a resistor (i.e. PEDOT:PSS). The main body of the antenna is silver ink and PEDOT:PSS was used as a resistive material which is sensitive to temperature. The resistance of the antenna changes when PEDOT:PSS is exposed to temperature change. Thus, the input impedance of the antenna changes. The antenna contains a PEDOT:PSS based temperature sensing element. The length of each side of the square antenna was 2.5 cm with a conductive track width of 2 mm thus the antenna is resonating at 1.2 GHz. In order to analyse the temperature sensing performance, the temperature-sensitive part was first fabricated separately using silver electrodes and conductive polymer PEDOT:PSS then the temperature sensing experiments were carried out. The ohmic resistance of the temperature sensing part decreases by ~70% when the temperature increases from 25 ^{o}C to 90 ^{o}C.

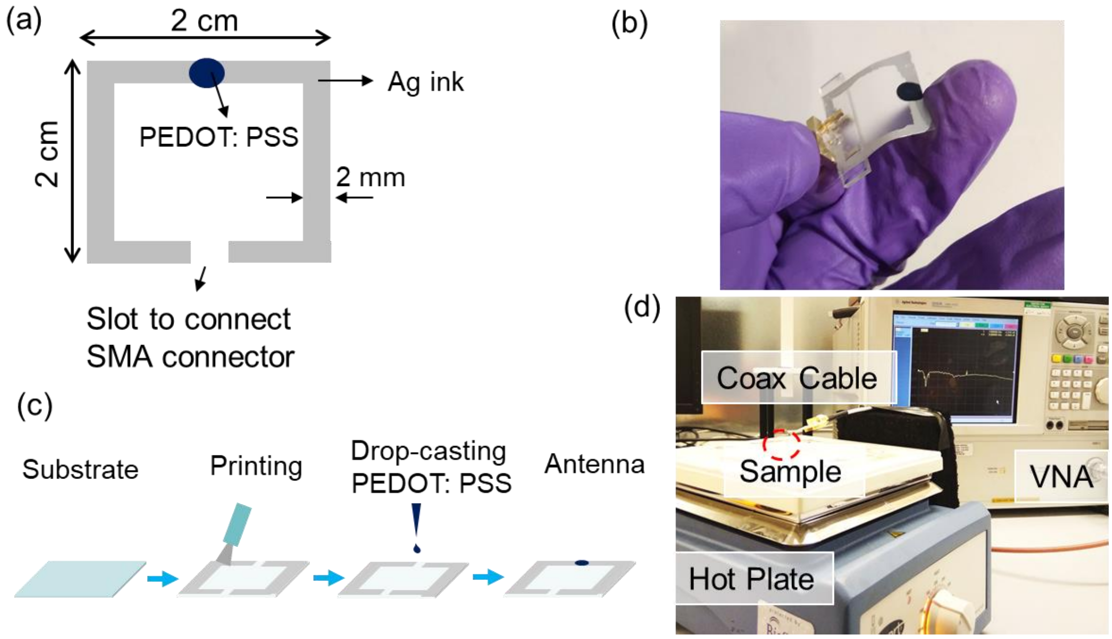

Figure 4-10 (a) Schematic illustration of the antenna design. (b) Images of the printed antenna-sensor on PVC substrate. (c) fabrication steps. (d) Experimental setup to measure change of resonant frequency over the change of temperature. Adopted from (46).

The characterization was perform using a vector network analyzer (Agilent E83628) to measure the return loss at different temperature values. The temperature change experiments were performed using a temperature controllable hotplate (Stuart CD162). A high-precision IR thermometer (FLUKE 62 MAX) was used to monitor the temperature while performing the experiments. The range of temperature was 25 °C – 90 °C. A theoretical study was performed to calculate the induced current in the antenna. It was found that the resistance was decreasing with the increase in temperature. The experimental result was also compared with the theoretical study.

In order to understand the induced current through the sensing antenna and the effect of the temperature on the same, a theoretical analysis was performed with small loop assumptions. The aim of this study was to calculate the average current in far-field through the antenna and hence to see if the model works in the frequency range of interest. The equivalent circuit for a receiving antenna contains an open-circuit voltage V_{OC}, a load impedance Z_L, and an input impedance Z_a connected in series. The current flowing through the loop is related to V_{OC}. With these assumptions, the induced current I can be written as:

$$I = \frac{V_{OC}}{Z_L+Z_a} \tag{4-2}$$

The voltage developed across the open terminal of the loop can be explained by Faraday's law for the time-varying magnetic flux. For a loop having N turns, the voltage is:

$$V_{OC} = -j\omega N \iint \bar{B} \cdot d\bar{s} \tag{4-3}$$

Where, $\omega = 2\pi f$ is the radian frequency, $\bar{B}$ magnetic flux density through the loop, and $d\bar{s}$ is the incremental surface area of the loop. The direction of the area in this case, is normal to the loop. Considering the loop to be small, the approximate magnetic flux crossing the loop is, $\iint \bar{B} \cdot d\bar{s} \approx B(\pi b^2)$, where B is the magnitude of magnetic flux. Moreover, the magnetic flux density can be calculated as, $\bar{B} = \mu\bar{H}$, where $\mu = \mu_0\mu_r$ is the permeability of the material. ($\mu_0 = 4\pi \times 10^{-7}$ H/m, the permeability of free space and μ_r is the relative permeability of the material). Hence, the induced voltage in an *N* turn small loop can be calculated as,

$$V_{OC} = -j\omega N\pi b^2\mu_0\mu_r H \tag{4-4}$$

The voltage across the Z_L can be calculated as:

$$V_L = V_{OC}\frac{Z_L}{Z_a+Z_L} \tag{4-5}$$

Whereas, the induced current is determined using the input impedance of the antenna which is defined as, $Z_a = R_a + jX_a$, where R_a is the input resistance, and X_a is the input reactance of the antenna. In addition, the input resistance also has two parts, $R_a = R_r + R_\Omega$, where, R_r is the radiation resistance, and R_Ω is the ohmic resistance of the antenna. The radiation resistance of a small N-turn loop antenna is:

$$R_r = 31200\left(\frac{N\pi b^2}{\lambda^2}\right)^2 \tag{4-6}$$

However, the ohmic resistance attributes to the power loss in terms of heating due to the current flow. If the conductivity of the material is σ, then the ohmic resistance (i.e. the surface resistance) for each turn is typically approximated as follows:

$$R_\Omega = \frac{b}{a}\sqrt{\frac{\omega\mu}{\sigma}} \tag{4-7}$$

Where, b is the radius of the loop and a is the radius of the wire. The small loops have high inductance which can be calculated as:

$$L = \mu b N^2\left(ln\left(\frac{8b}{a}\right) - 2\right) \tag{4-8}$$

In general, the reactance X_a is the inductance associated with the antenna. Hence, the input impedance can be written as:

$$Z_a = R_a + j\omega\mu b N^2\left(ln\left(\frac{8b}{a}\right) - 2\right) = 31200\left(\frac{N\pi b^2}{\lambda^2}\right)^2 + \frac{b}{a}\sqrt{\frac{\omega\mu}{\sigma}} + j\omega\mu b N^2\left(ln\left(\frac{8b}{a}\right) - 2\right) \tag{4-9}$$

Hence, the current induced in the small loop can be calculated as:

$$I = \frac{-j\omega N\pi b^2\mu_0\mu_r H}{Z_L+31200\left(\frac{N\pi b^2}{\lambda^2}\right)^2+\frac{b}{a}\sqrt{\frac{\omega\mu}{\sigma}}+j\omega\mu b N^2\left(ln\left(\frac{8b}{a}\right)-2\right)} \qquad (4\text{-}10)$$

This equation describes the effect of the load impedance on the current in the loop. **Figure 4-11** shows the obtained current values with (a) temperature and (b) frequency. The plots suggest that induced current increase with temperature and have a stronger effect at higher frequencies. However, **Figure 4-11 (b)** shows that the current also increases at low frequency ranges.

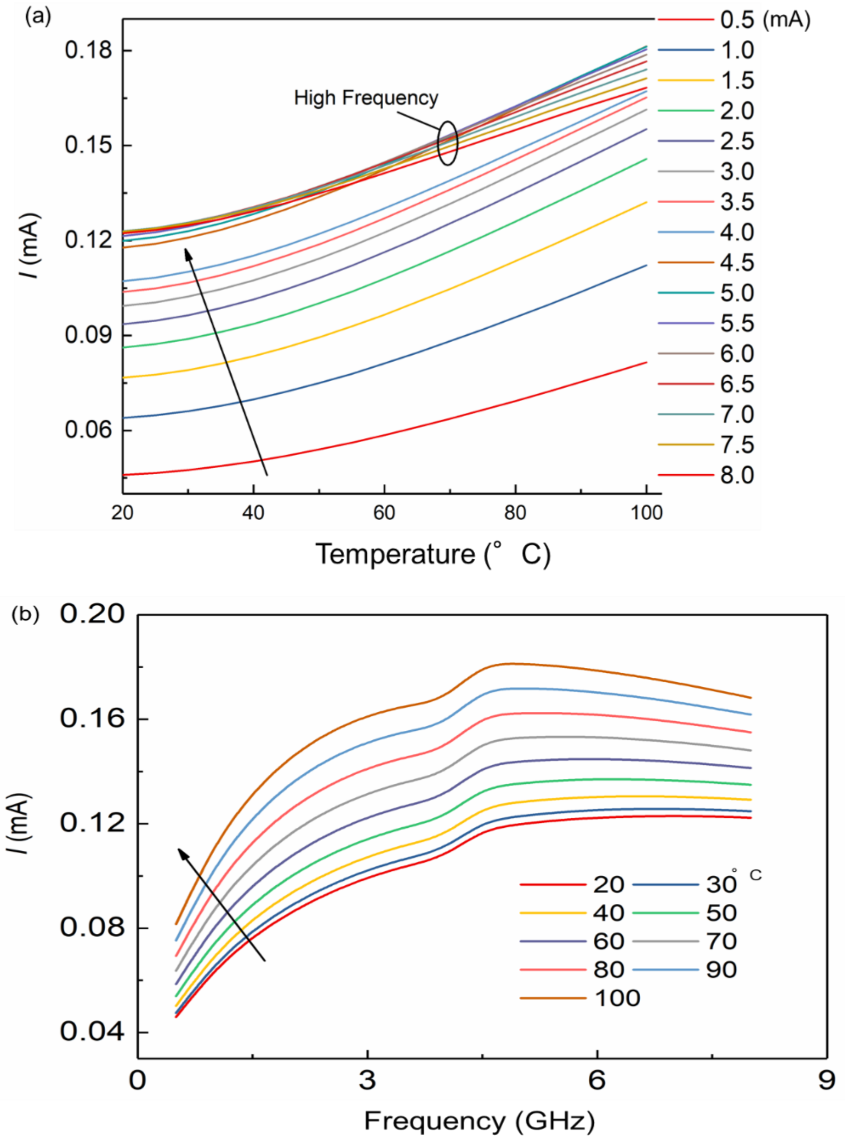

Figure 4-11 Simulated induced current values (a) with temperature and (b) with frequency obtained from the theoretical study. The equivalent circuit for a receiving antenna contains an open-circuit voltage V_{OC}, a load impedance Z_L, and an input impedance Z_a connected in series as illustrated in the inset (a). (46)

The temperature sensing properties of the antenna were tested by increasing the temperature of the antenna using a controllable hotplate. The S_{11} parameter was measured for the sensing antenna at different temperature conditions. It was observed that the magnitude of return loss decreased due to the enhancement of temperature. This can be attributed to the change in the resistance of the sensing PEDOT:PSS element that leads to the overall change in the sensing antenna impedance. **Figure 4-12** shows the S_{11} parameter vs the frequency for the PEDOT:PSS sensing antenna at different temperatures ranging from 25 – 90 ºC at 1- 2.5 GHz. A sensitivity of ~1.2%/ºC was observed for the sensing antenna.

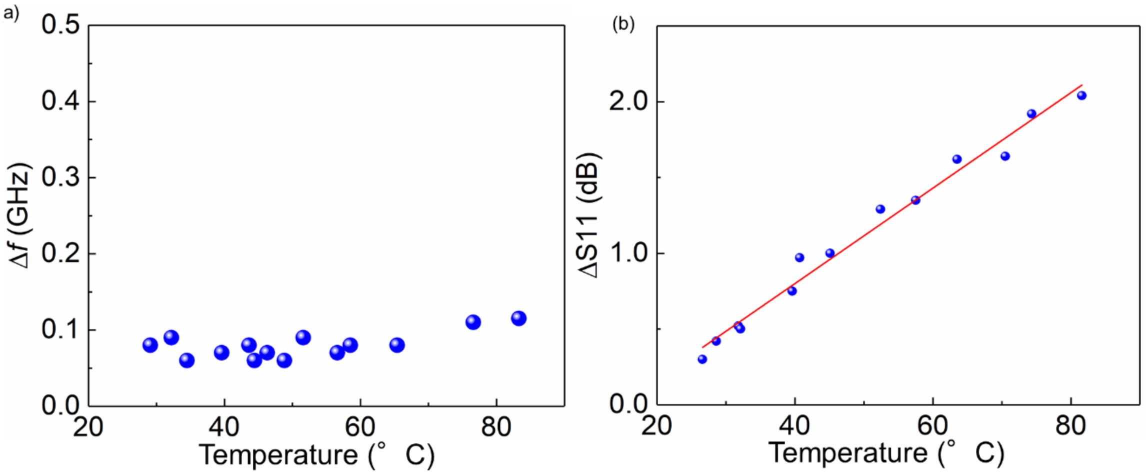

Figure 4-12 Frequency Response of the antenna at different temperatures. (a) frequency shifts due to the temperature changes (b) magnitude of ΔS_{11} at different temperatures.

Two types of bending conditions were taken under consideration (i) lateral bending – where the sensing patch was bent during the bending and (iii) cross bending – where the bending does not affect the sensing material. Two bending radii, 5.7 cm, and 11.0 cm were employed in the experiments. The bending radii were decided based on the radii of disposable bottles used for water or beverages. The antenna was found to be suitable for bending applications as well. It was also observed that the return loss and resonant frequency changes significantly once the antenna undergo a lateral bending. However, the antenna is found to be more stable in the case of cross bending conditions.

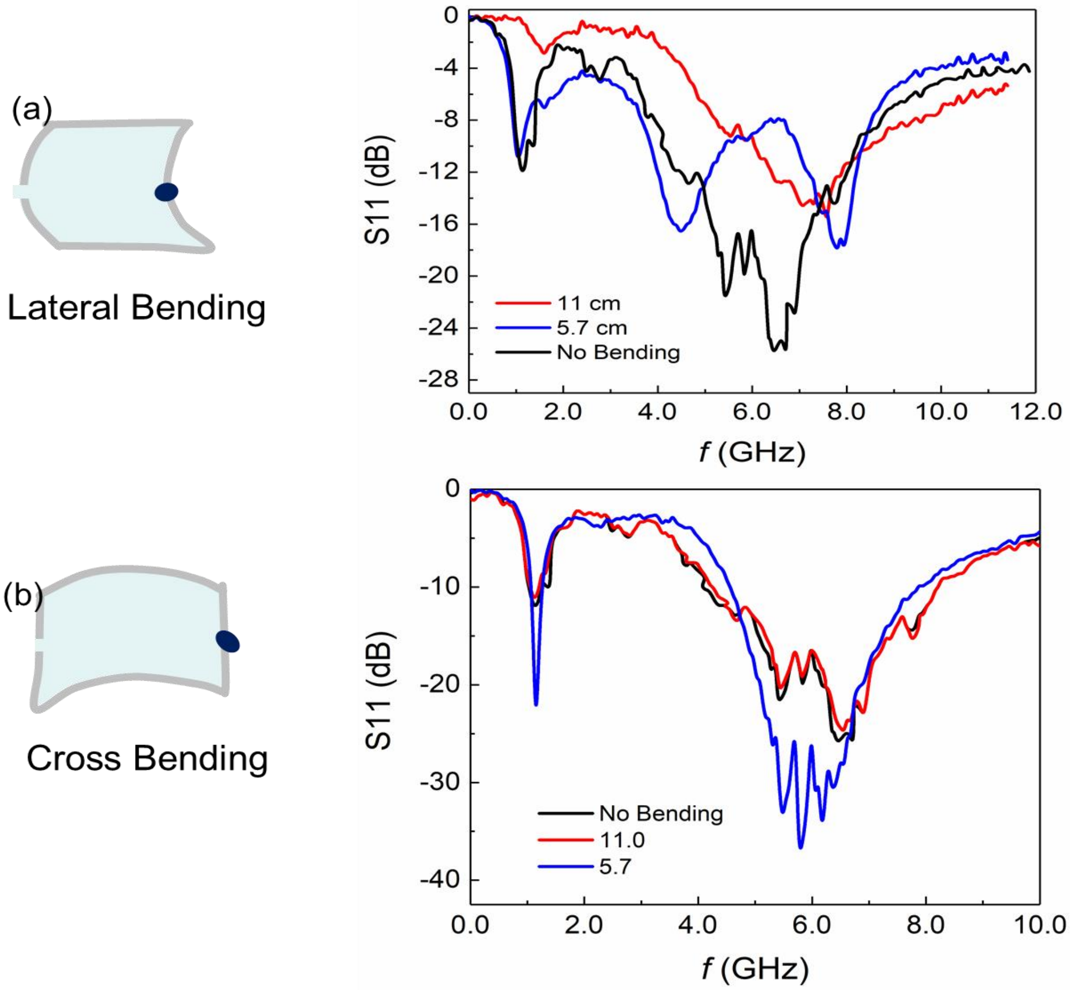

Figure 4-13 Bending effect on the fabricated sensing antenna (a) Effect of lateral bending of sensing antenna on S_{11}. (b) Effect of Cross-bending of sensing antenna on S_{11}. The legends in the plots show the bending radii 11.0 and 5.7 cm.

This flexible sensing antenna can be used as temperature sensing applications in smart labels. This sensor is printed and disposable in nature and hence is expected to be a more affordable solution for large scale deployment.

4.3 Summary

In this chapter two kind of antenna sensing using functional materials have been presented. In the first study, we have developed a screen-printed flexible LC tank device to wirelessly detect the pressure and have showed its suitability for biomedical application. The presented sensor is developed using low-cost and scalable fabrication methods such as electrospinning and screen-printing. The tank consists of a planar inductor connected in parallel to an interdigital capacitor designed to resonate at 13.56 MHz. The sensing principle is based on the change in the capacitance of IDC under pressure which leads to a variation in resonant frequency. The shift of frequency of the parallel LC tank as a measure for applied dynamic pressure is detected wirelessly using the inductive coupling with a second external inductor. The realised capacitive sensor exhibit high sensitivity 0.035 kP^{-1} and 1200 Hz/kPa in wireless characterisation, along with excellent durability over 1800 cycles. The fabricated sensor demonstrated good repeatability and linear sensitivity in the pressure range (0-16 kPa) appropriate for wearable healthcare applications such as monitoring the sub-bandage pressure. The application of optimum pressure by the bandage, together with the electroceutical arrangement facilitated by the piezoelectric PLLA substrate, could accelerate the cell regeneration and hence wound healing. An in-depth analysis of the influence of piezoelectric properties of PLLA on the wound healing through electrical stimulation will be explored further as a future work.

In the second study, a flexible loop antenna as wireless temperature sensor was developed. The functional material was PEDOT:PSS which is one of the most stable conductive polymers. The antenna was similar to a dipole antenna which is terminated to a resistive material (PEDOT:PSS). The relation between temperature change and frequency response of the antenna has been studied. The S_{11} parameter was measured for the sensing antenna at different temperature (25- 90 °C). It was observed that the magnitude of return loss decreased due to the enhancement of temperature. A sensitivity of ~1.2%/°C was observed for the sensing antenna. A theoretical study was performed to analyse the induced current in the antenna. It was found that the resistance was decreasing with the increase in temperature. The experimental result was also compared with the theoretical study.

Chapter 5. Sensing antenna through geometry changes

5.1 Textile-based stretchable antenna as strain sensor[7]

5.1.1 Introduction

In chapter 2, it was established that one mechanism to design a sensing antenna is to exploit geometry deformation (e.g. the elongation or bending). These geometrical modifications could change the resonant frequency of the antenna which then can be mapped to the external stimuli causing the modification, this chapter focus on this concept. These features are needed to reduce number of devices on wearable system without increasing number of elements for users' comfort.

The general approach to convert the conventional electrodes to stretchable ones consists of patterning them with a repeated unit cell. Generally, the stiffness of metals could be managed using this approach to fabricate highly stretchable 3D structures (201). Kirigami-like structures (202-204), twisted helical springs (205), and serpentine shapes (82, 206, 207) are some of the conventional methods to develop large-area electronics with duplicated unit cells, either to enhance stretchability or minimize the size (208). These methods have been rarely reported as an active or passive microwave device such as an antenna.

5.1.2 Antenna design

The schematic view of the three microstrip antenna design used in this work is shown in **Figure 5-1**. Similar designs, converting a solid antenna structure into a meshed layout for RF applications, have been reported in past (209). The stretchability of meshed structure increases with the bigger serpentine arc angle. Based on the study that has been done in [45] there is a trade-off between mechanical stretchability and EM performance of meshed antennas. It was shown that the attenuation constant (α) which is an indicator of propagation loss is minimum when the serpentine arc angle is 220°. Considering the limitation of chosen

---

[7] This section is extracted from publication #1 where F. Nikbakhtnasrabadi was the main contributor. The design, simulation, fabrication and characterisation were carried out by F. Nikbakhtnasrabadi.

fabrication method (cutting with laser) the length of each unit which indicates the density of meshes is chosen as 15 mm which is in the sub-wavelength range, about λ/15 (λ is free space wavelength). The effect of line width is negligible [50] on the resonance frequency however to keep the radiation loss minimum as possible the minimal value of 1 mm is chosen as line width which is the smallest feature of the textile that can be cut using the laser cutter. **Figure 5-1** illustrates the general strategy that was followed to convert the solid antenna to a fully stretchable structure. Firstly, a conventional textile microstrip patch antenna was designed (**Figure 5-1 (a)**). Based on that design, the patch layer was then patterned in a meshed layout to improve the stretchability of the antenna (**Figure 5-1 (b)**).

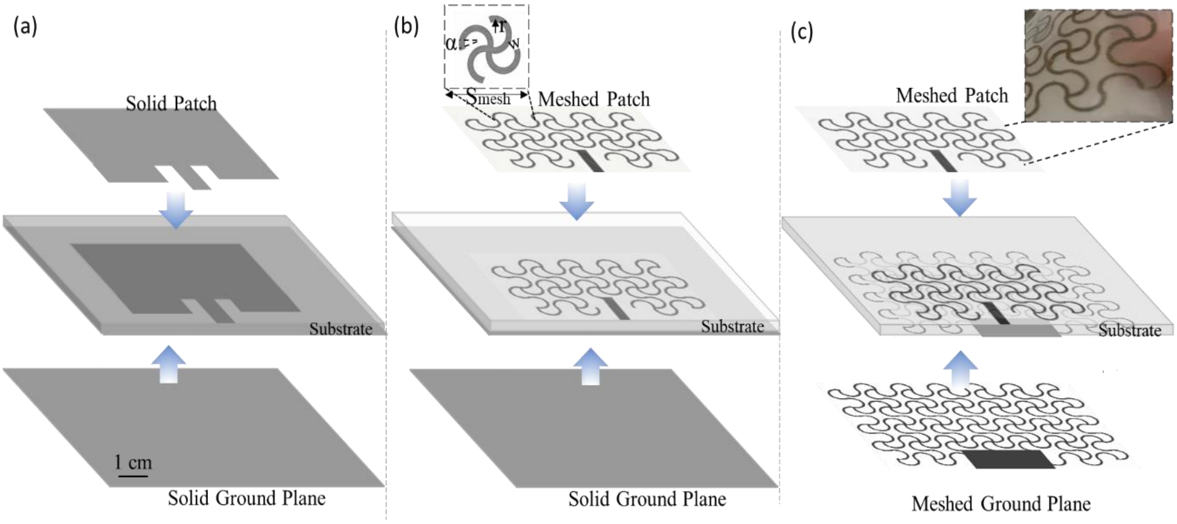

Figure 5-1 Schematic view of the three versions of the designed textile microstrip antennas. In all cases, the substrate is Ecoflex with thickness of 2 mm and the overall size of the patches and ground planes were kept equal. (a) Microstrip antenna made of solid metal-plated conductive textile. (b) Improving stretchability of microstrip antenna by converting the solid patch to a meshed structure. The ground plane is kept as solid metal-plated textile. (c) Conversion of both the solid patch and the ground plane with meshed structures. The inset image demonstrates that meshed structures are embedded in Ecoflex because Ecoflex was partially cured.

Afterward, the ground plane was also converted to a meshed layout, thus achieving up to 100% stretchability comparing to initial length (**Figure 5-1 (c)**). The strain is defined as $\varepsilon = \frac{L-L_0}{L_0}$ where L_0 is the initial length of the stretchable antenna and L is the elongated length under uniaxial strain conditions. In the following sections, the electromagnetic performance of these three textile antennas is compared in terms of resonant frequency and radiation pattern.

The dimensions of the antenna are the key factors that define its resonant frequency. To design a rectangular patch antenna, the length and the width of the rectangular patch were calculated based on the transmission line model. The four most popular feeding techniques to feed microstrip antennas, i.e., to drive power to the antenna are: coaxial probe, microstrip line, aperture coupling, and proximity coupling. To realize a planar structure and eliminate the need for additional matching elements, the proposed antenna was fed using an inset feed microstrip line. Generally, the input impedance of the patch in the edge is almost 300 Ω. Since most microwave sources are manufactured with a characteristic impedance of 50 Ω, an inset feed line was used to match the impedance of the source and the patch. Inset point and size of slots were obtained through optimization in High-Frequency Structure Simulator (HFSS) software (ANSYS Electromagnetics Suite 19.0, US). According to the desired dimensions of the antenna (45 mm × 26 mm), the main resonant frequency was found at 4 GHz for the case of the solid textile patch antenna. According to Ofcom (210), the 3.8 - 4.2 GHz spectrum band could enable the use of 5G technology for private industrial networks. The dimensions of the ground plane were kept $6h + L$ and $6h + W$ as suggested in the literature (211). The ground plane was made from the same conductive textile with dimensions of 57 mm × 38 mm. The threshold for reflection coefficient was considered -$20\log|S11| < -10$ dB, meaning that 90% of incoming power in the desired resonant frequency is radiating, where dielectric and ohmic losses are negligible. The slot width adjacent to the feedline was 3 mm, which was inset into the rectangular patch for 9 mm.

5.1.3 Materials

In this work, silver-plated knitted textile (MedTex, UK) was used to fabricate the radiating patch and ground plane of microstrip antennas, while Ecoflex was sandwiched in between the two layers as the substrate. The employed textile sheet was made of 94% Nylon and 6% Elastomer plated with 99% pure silver. The total thickness of the textile sheet was 0.55±10% mm with an average conductivity of 1.14×10^3 S/m. The average thickness of plated silver was ~0.015 mm (212). This textile sheet was selected due to its stretchability without significant change in its resistance. All the mentioned values were assigned as the conductive textile material properties in the HFSS model. Ecoflex 00-30 (Smooth-On Inc., US) with 2 mm thickness was used as a substrate for all samples. The polymer was supplied in two parts, i.e., base and curing agent (A and B). In the simulation model, a dielectric constant of 2.8 and loss tangent of 0.02 was assigned to Ecoflex considering mixing ratio 1A:1B (213).

5.1.4 Textile-based antenna fabrication

Three versions of textile-based microstrip antennas, as shown in **Figure 5-1**, were fabricated using the CO2 laser machine. To fabricate the first version (**Figure 5-1 (a)**), which is a conventional microstrip antenna made from the stretchable conductive textile, the patch and ground plane outlines were cut using the laser-based cutting machine according to the designed dimensions (see Section II). For the Ecoflex 00-30 substrate, parts A and B were mixed well with a 1:1 ratio. The mixture was then degassed in a desiccator for 15 minutes to remove bubbles. Afterward, the mixture was poured into a rectangular mold made of Polylactic Acid (PLA) with 2.5 mm depth. Once Ecoflex was partially cured, the patch was placed on top. Since the mixture was not fully cured at this point, the patch was slightly embedded within the substrate thus ensuring good adhesion between them and sealing the textile. The porous nature of the fabric allows the creation of polymer-polymer bonding that provides good adhesion. Afterward, the cured Ecoflex was peeled off from the mold and the ground plane was bonded to the substrate underneath using a very thin layer of fresh Ecoflex. At this point, it was observed that the strong adhesion limited the stretchability of the textile in a way that the antenna was not stretchable anymore, despite the stretchy nature of the used textile. Eventually, an edge-mount Subminiature Version A (SMA), 50 Ω, RF connector was attached to the antenna feed line. Since the materials used to fabricate the antenna were sensitive to high temperatures, the SMA connector was attached using room-temperature curable silver conductive adhesive epoxy (MG Chemical, UK) instead of soldering.

The first step to overcome the lack of stretchability in the first version of the textile antenna was to pattern the patch in a rectangular serpentine structure. The solid patch was converted to a serpentine-shape layout as shown in **Figure 5-1 (b)**. The antenna stretchability is highly dependent on the morphologic parameters of the serpentine pattern, such as the radius of curvature, arc angle, and tracks width. The arc angle was set to 220° according to the previous study (214), which results in less absorption loss while maintaining mechanical robustness. **Figure 5-1 (b)** inset shows the serpentine-unit pattern, which was periodically implemented throughout the entire structure. The internal radius and the thickness of each arc unit were 2.25 mm and 1 mm, respectively. These values were chosen considering the resolution limitations of the laser cutter. Material database of laser cutter in terms of power (optimum value=20%), speed (optimum value =3), and Pulse per Inch (optimum value of PPI=1000 Hz) were tuned to prevent burning marks in the edges of the design. The connection track between the feedline and the meshed patch was slightly wider (i.e. 1.5 mm) than the other tracks to avoid failure upon stretching. The pattern was first designed in AutoCAD and then imported to Corel Draw for the cutting process with the automated laser machine.

Figure 5-2 (a) shows a microscope view of the silver-plated textile before and after cutting. Although some outlines with burn marks can be observed, the resistance did not change significantly. The resistance of serpentine-unit (end-to-end) was 1.8±0.17 Ω. **Figure 5-2 (b)** shows scanning electron microscopy (SEM) images of random joint points of the fabricated pattern at different magnifications. White marks show that the polymer was slightly melted in the edges by the laser. Lastly, the meshed patch and solid ground plane were bonded to the Ecoflex substrate and an SMA connector was attached as described earlier.

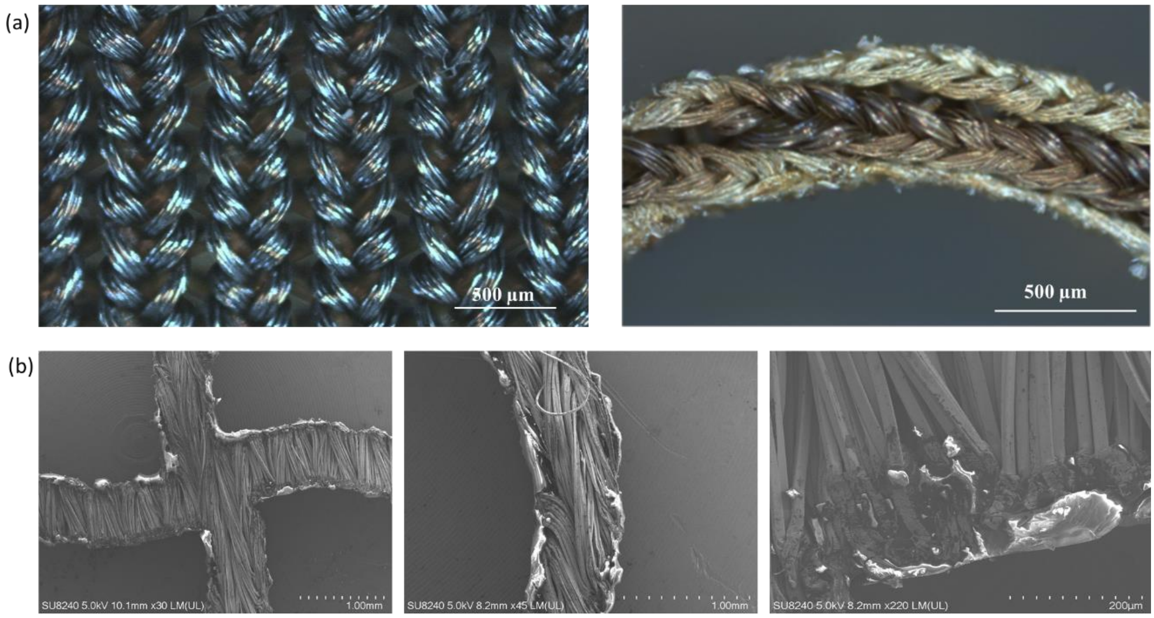

Figure 5-2 (a) Optical images of silver-plated knitted textile (left) and laser cut textile (right). (b) SEM image of laser cut textile of a random joint point and magnification on cut edges where Nylon/Elastomer was melted due to laser operation.

To achieve a fully meshed microstrip antenna with higher stretchability, the solid ground plane was also converted to a meshed pattern (see **Figure 5-1 (c)**). The effect of replacing the solid textile with a meshed pattern on the resonant frequency and radiation pattern will be explained in the next section. In this stage, the textile was laser-cut using the same method, as described before to pattern the patch, to fabricate meshed ground plane. It is worth mentioning that the 1×2 mm^2 portion in the midpoint was kept solid to provide durable support to connect SMA to the ground plane. Likewise, as previously described, both meshed patch and ground planes were attached to the substrate and an SMA connector.

5.1.5 Gold meshed-patch antenna fabrication

To compare the performance of our textile-based microstrip antenna (i.e. meshed-patch with a solid ground) with its metal-based counterpart (82, 193), a gold (Au) meshed antenna with the same dimensions was fabricated using photolithography steps (215). To this end, a polyimide (PI) layer (DuPont Inc., Delaware, USA) was spun on a carrier wafer. Then it was cured for three hours at 200 °C in nitrogen ambient to form a sheet of 25 μm thickness. Later, a positive photoresist (S1818) was spun (4000 rpm for 30 sec) on it and baked on a hotplate at 115 °C for 3 minutes. The pattern was defined using a high-resolution optical mask aligner (SUSS MicroTec., Germany) with UV exposure for 6 seconds. Then MF-319 developer was used for 2.5 minutes to form the pattern. Metal evaporation of Ti(10 nm)/Au(100 nm) formed the layer of metal deposited on the PI substrate. Subsequently, a lift-off stage in an ultrasonic acetone bath was performed. **Figure 5-3 (a)** depicts the fabrication process, while **Figure 5-3 (b)** shows the sample after being rinsed gently in Isopropyl alcohol (IPA) to remove any gold residues. Optical microscope images (**Figure 5-3 (b)**) confirm that gold tracks are intact without any crack and the adhesion between the gold layer and the PI film is robust. Eventually, the unpatterned part of the PI film was removed using the CO2 laser, and the patch was attached to the Ecoflex substrate following the same procedure described for the textile-based microstrip antennas. Instead of using CO2 laser, one can use lift-off process to separate PI film from the gold pattern however due to JWNC instruction this was not possible as MF-319 developer was used earlier. Commercial single-side copper clad board (Kitronik, UK) with a thickness of 1 mm was used as a free-stand ground plane beneath the sample.

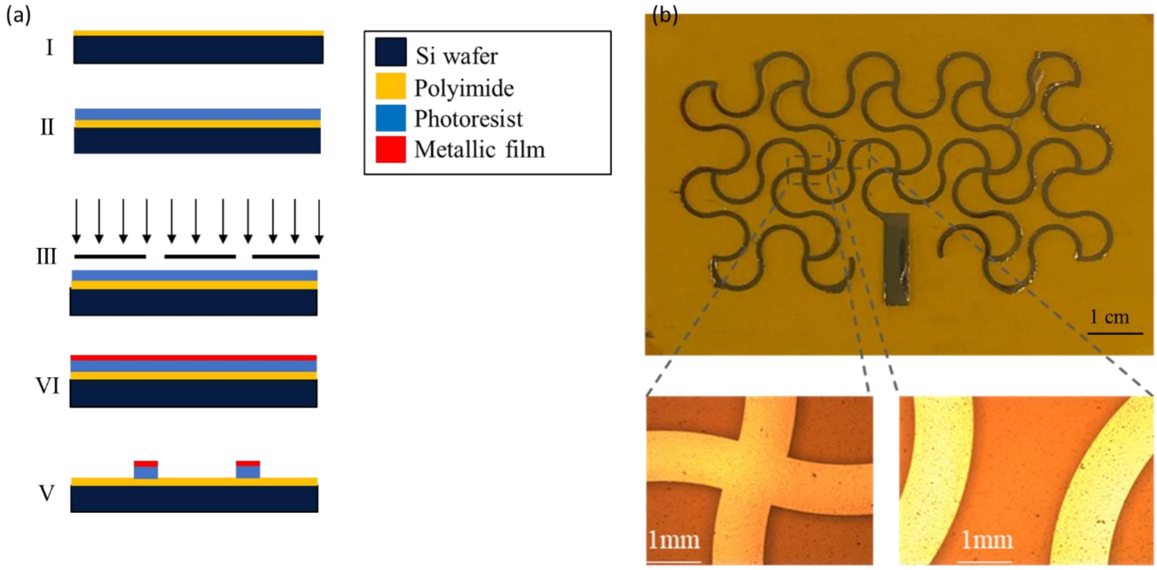

Figure 5-3 (a) Schematic representation of the fabrication steps for realization of gold patch on Polyimide. (b) Optical microscope image of random parts of the gold pattern. (Courtesy: the fabrication was done under supervision of Dr. Mahesh Soni)

5.1.6 Characterization set-up

For RF characterization, the scattering parameters of the antennas were collected using a Vector Network Analyzer (VNA) (E83628, Agilent Technologies, US) to observe the change of resonant frequency with the applied strain. Radiation pattern measurements were conducted inside an anechoic chamber as shown in **Figure 5-4 (a).** To characterize the fabricated prototypes, a custom-made setup was used to evaluate their performance over uniaxial stretching (**Figure 5-4 (b)**). The holder is 3D-printed using an Ultimaker S5 and polylactic acid (PLA) filament (RS Components, UK). Two parallel grooved grippers were used to hold the sample in place and uniform uniaxial tension was applied to the samples by pulling the grippers with the help of a light rope and a pulley system. Grade markers were printed on the setup to measure the elongation while applying uniaxial strain.

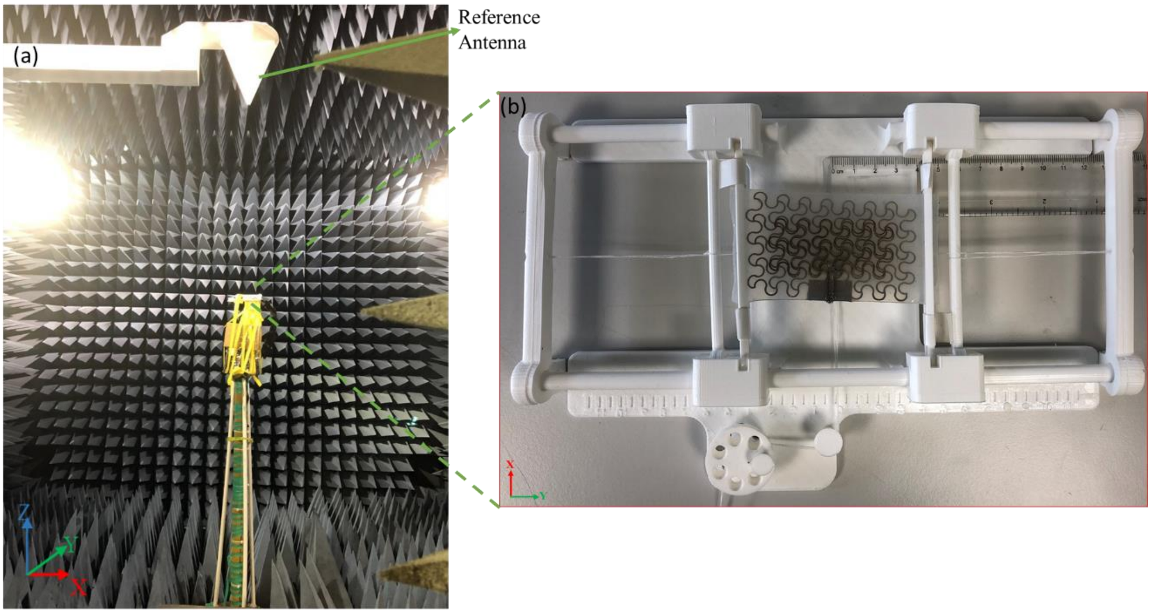

Figure 5-4 Experimental setup for radiation pattern measurements inside the anechoic chamber (left). Broadband (0.5 MHz -18 GHz) dual polarized log periodic antenna was used as reference. The inset image on the right shows the fully meshed microstrip antenna mounted on the custom-made setup in zero strain condition.

5.1.7 2D digital correlation technique

To validate the experimental results, all the proposed structures were simulated in HFSS. The stretching procedure was recorded using a high-resolution camera and Digital Image Correlation (DIC) technique to monitor the deformation of the meshed layouts, as described below. Processed images acquired at a specific stage of stretching were imported into HFSS to evaluate their electromagnetic (EM) performance. The Mechanical deformation of serpentine mesh geometries upon the uniaxial strain has been investigated in past using the finite element method (FEM) through ABAQUS with some simplifications (e.g. considering uniformity in strain to the entire model and out of plane deformation as in-plane deformations) applied due to the excessive number of nodes and elements (82, 209). It is

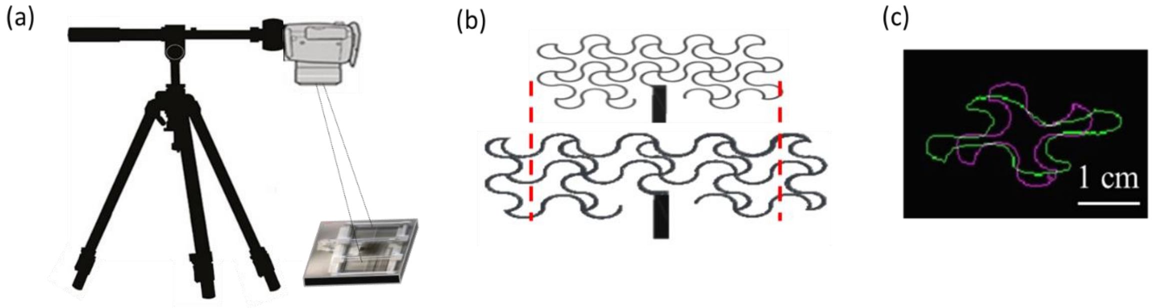

Figure 5-5 (a) 2D DIC set-up with horizontal tripod arm. The Optical axis of the camera is aligned perpendicular to the sample surface to avoid errors in the image correlation. (b) CAD schematic representing the surface morphology of the patch in 0% (top) and 40% strain (bottom). (c) serpentine unit cell of the patch. Purple contour shows an un-deformed shape while green one shows the corresponding contour for 40% strain.

worth mentioning that the conductive material in previous studies was a conventional copper sheet. In our study, commercial conductive knitted textile was used, in which actual material properties such as Young's Modulus, Poisson's Ration, and Coefficient of Friction are unavailable. Moreover, the nonplanar nature of textiles and the effect of mechanical distortion on the inhomogeneous displacement of the textile yarns make FEM an unreliable technique for our textile antennas. As an alternative, a two-dimensional DIC technique was used to evaluate the applied strain using the contact-less full-field optical technique over the sample area during uniaxial tensile tests. DIC provides an accurate solution to investigate material deformation and crack propagation in real-world applications (216). The basic principle of this technique is to monitor displacements by analysis of a digital image series. This is done by taking successive images of the objects over time under various uniaxial strain conditions and then analyzing them through specific correlation-based algorithms (217). To apply this technique, the camera was positioned vertically and parallel to the flat surface of the sample to avoid out-of-plane image correlation errors (218). Since only one camera is using in this technique it cannot record out-of-plane displacement as well however in our experiment there is no out of plane displacement. The recorded video was split into a series of digital images for postprocessing in MATLAB to obtain a full-field deformation map at different levels of elongation. The effect of uniaxial strain was indirectly determined considering differentiation of the measured displacements. Afterward, the pixel displacements were converted to actual displacements to model the deformed patch in AutoCAD, and then imported to HFSS to investigate the radiation patterns in different levels of applied strain. It was observed that, by increasing the tensile strain, the vertical arcs became shorter and horizontal arcs became wider. However, serpentine units were deformed perpendicular to the feedline direction rather than in the direction of the current flow. **Figure**

5-5 (a) shows a schematic of the DIC setup for in-plane displacement measurement. As a proof of concept, the pristine and deformed shape of the unit cell and patch, obtained using the DIC technique, are presented in **Figure 5-5 (b),(c)** for 0% and 40% strains.

5.1.8 Results and Discussion

In the first place, the custom-made tensile setup was used to study the change in the electrical properties of the textile (i.e., resistance) upon uniaxial stretching. The custom-made tensile setup shown in **Figure 5-6** was used to study the change in the electrical properties of the textile (i.e., resistance) upon uniaxial stretching. The setup consists of two holders controlled by a pair of stepper motors (Translation Stage VT-21L Micronix, US) with a velocity of movement of $V_S = 0.1$ mm/s and a LabVIEW to stretch the samples homogenously from both sides up to 100% strain. Two rectangular textile pieces were added to the design of the patch to make electrical connections. Electrical resistance was simultaneously collected using a digital multimetre (34461A, Agilent, US) connected to the samples.

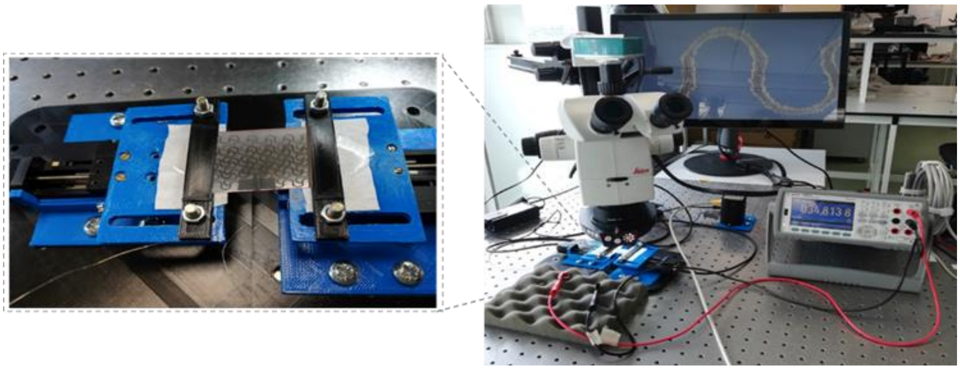

Figure 5-6 Custom-made setup to evaluate the electromechanical performance of meshed textile structure. (Courtesy: This characterization was carried out under Dr. Martina Aurora Costa Angeli supervision)

Figure 5-7 (a) shows that the end-to-end conductance of the patch halved when strain increased gradually up to 100%. The average conductivity of the patch was 0.89 $\times 10^3$ S/m and 0.58 $\times 10^3$ S/m under 0% and 30% strain respectively. The corresponding value of conductivity is still good enough to be used as a radiating structure in antennas (219). Furthermore, to evaluate fatigue cycling stability of the meshed patch a 100 cycles test was carried and it was observed that it retained its original value with standard deviation of 5.8% under 30% strain after 100 cycles. No failure was observed after these 100 cycles. **Figure 5-7 (b)** Electromechanical response of serpentine fabric stretched 100 cycles at 30% strain.

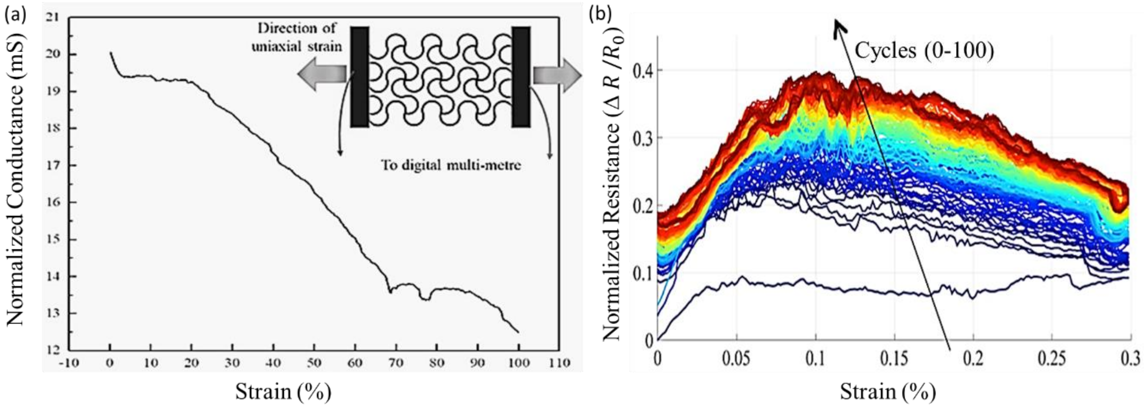

Figure 5-7 (a) Change in conductance of textile meshed patch at different values of uniaxial tensile deformation. Inset image shows schematic of electromechanical test setup. (79) (b) Electromechanical response of serpentine fabric stretched 100 cycles at 30% strain. (Courtesy: This characterization was carried out under Dr. Martina Aurora Costa Angeli supervision)

To characterize the resonance frequency of the antennas, the samples were connected to the VNA using a lightweight coaxial cable. Prior to the measurements, a Short-Open-Load (SOL) calibration was performed using Keysight 85052D calibration kit. **Figure 5-8 (a)** shows that the fabricated solid textile microstrip antenna resonates at 4 GHz, whereas the antenna with the meshed patch over a solid ground plane and the fully meshed microstrip antenna has a resonance at 2.98 GHz and 3.45 GHz, respectively. In conventional microstrip antennas, the resonant frequency is a function of some physical parameters such as the patch length and the substrate thickness. To shift down the resonant frequency, the patch length would need to increase (220). However, the obtained results suggest that meshing the antenna, either the patch or the ground plane, can also be used to tune the resonant frequency to the desired frequency spectrum. In our case, instead of increasing the length of the patch to lower down the resonant frequency, the meshed patch with a solid ground plane reduced the resonant frequency by 25% while the fully meshed antenna moved it down by 13.7%. The radiation patterns in E-plane and H-plane for the solid textile antenna resonating at 4 GHz (**Figure 5-8 (b)**) represent a relatively large back lobe, probably due to the small thickness of the silver layer in the textile ground plane.

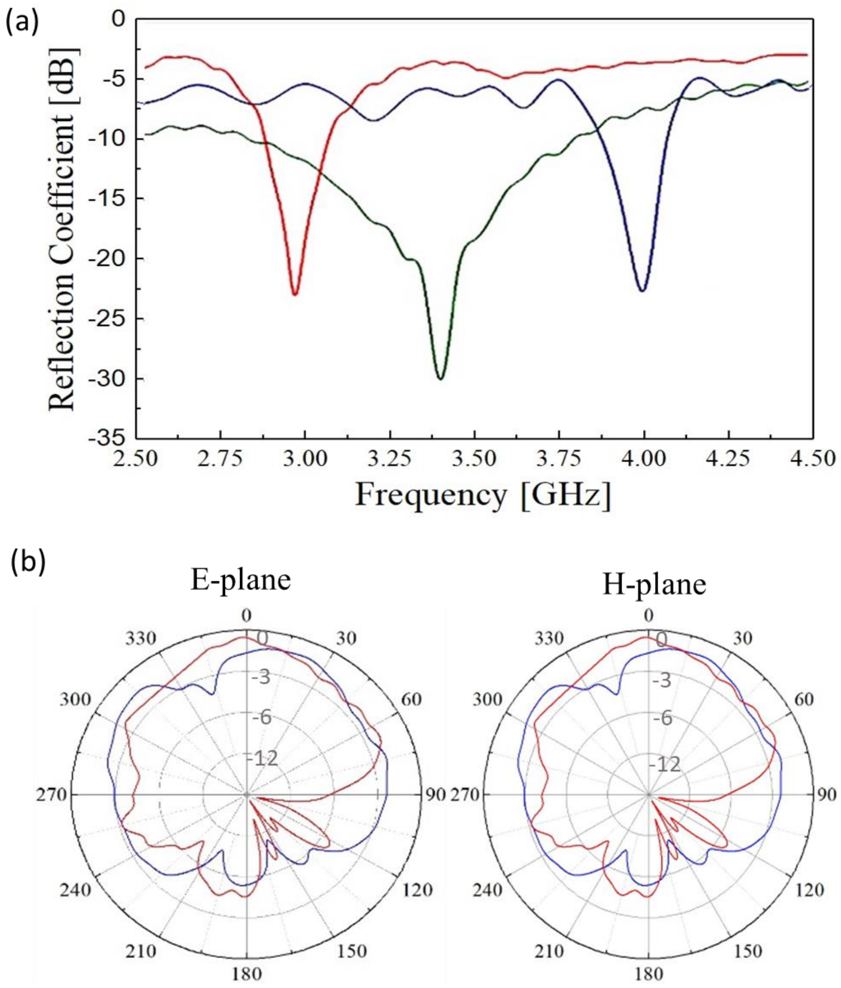

Figure 5-8 Solid textile antenna analysis: a) Effect of meshes in the patch on solid ground and of both patch and ground on the change of resonant frequency compared to conventional equivalent. S_{11} of conventional textile antenna, meshed patch over the solid ground, and meshed patch over meshed ground plane are presented with blue, red, and green lines respectively. b) Measured and simulated radiation patterns in E and H planes at 4 GHz. Red lines represent simulated where the blue line is obtained from the measurement.

The textile meshed patch over the solid ground plane, showed good stretchability up to 40%, with the resonant frequency shifting down with a linear trend as shown in **Figure 5-9 (a)**. It was observed that the resonant frequency moved down to 2.75 GHz when the uniaxial strain increased up to 40%. The reflection coefficient values were kept below -10 dB within the entire elongation range, which indicates that the impedance matching between the antenna and the inset feedline was maintained over the stretching. The linear trend suggests that the antenna has the potential to be used as a strain sensor by exploiting its stretchability, as previously stated. Considering the sensitivity to strain as $\frac{\Delta f/f\ (resonant)}{\Delta L/_{L}}$ $(\frac{MHz}{mm})$, the average sensitivity of the antenna is 0.2 over the 0 to 40% strain range. To study the effect of strain on the radiation pattern, the antenna was placed on the tensile setup with an applied strain of 30%. The radiation patterns in the unstretched and stretched conditions were then compared.

As observed from **Figure 5-9 (b)**, the radiation pattern in the E-plane did not change significantly when the antenna was stretched, but in the case of the H-plane, a null appeared in the main lobe. In general, the gain of the antenna increased when the strain was applied, which is in line with previous work (193), which proved that the losses in the meshed transmission line decreased when the device was stretched.

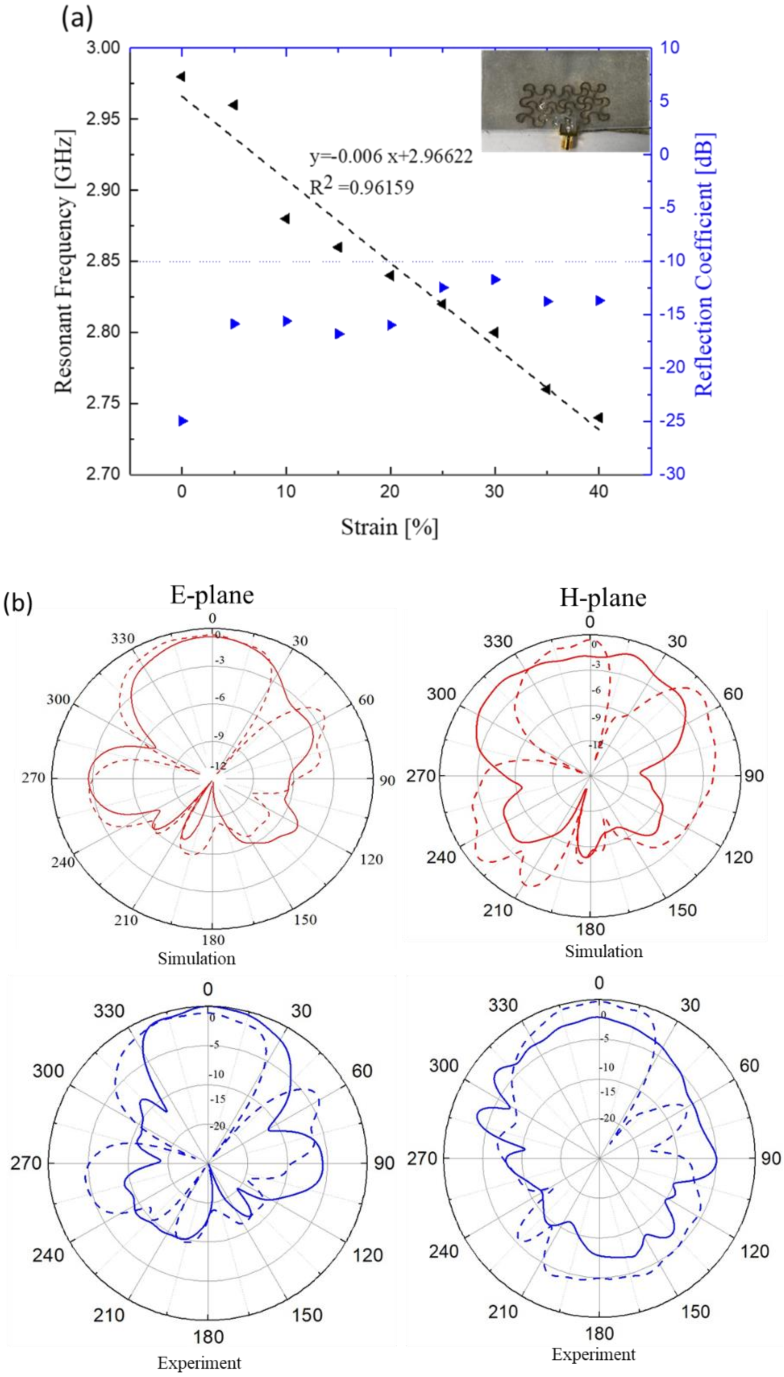

Figure 5-9 Textile meshed patch over solid ground analysis: a) Change of resonant frequency and S_{11} as a function of tensile strain up to 40%. b) Comparison of the radiation patterns in the E-plane (left) and H-plane (right) in relaxed ($f_{res=}$ 2.98 GHz) and 30% uniaxial strain ($f_{res=}$ 2.81 GHz) conditions. The simulation results of 30% strain (bottom) were extracted from the model obtained by DIC method at 30%. Solid lines and dash lines represent 0% and 30% strain respectively.

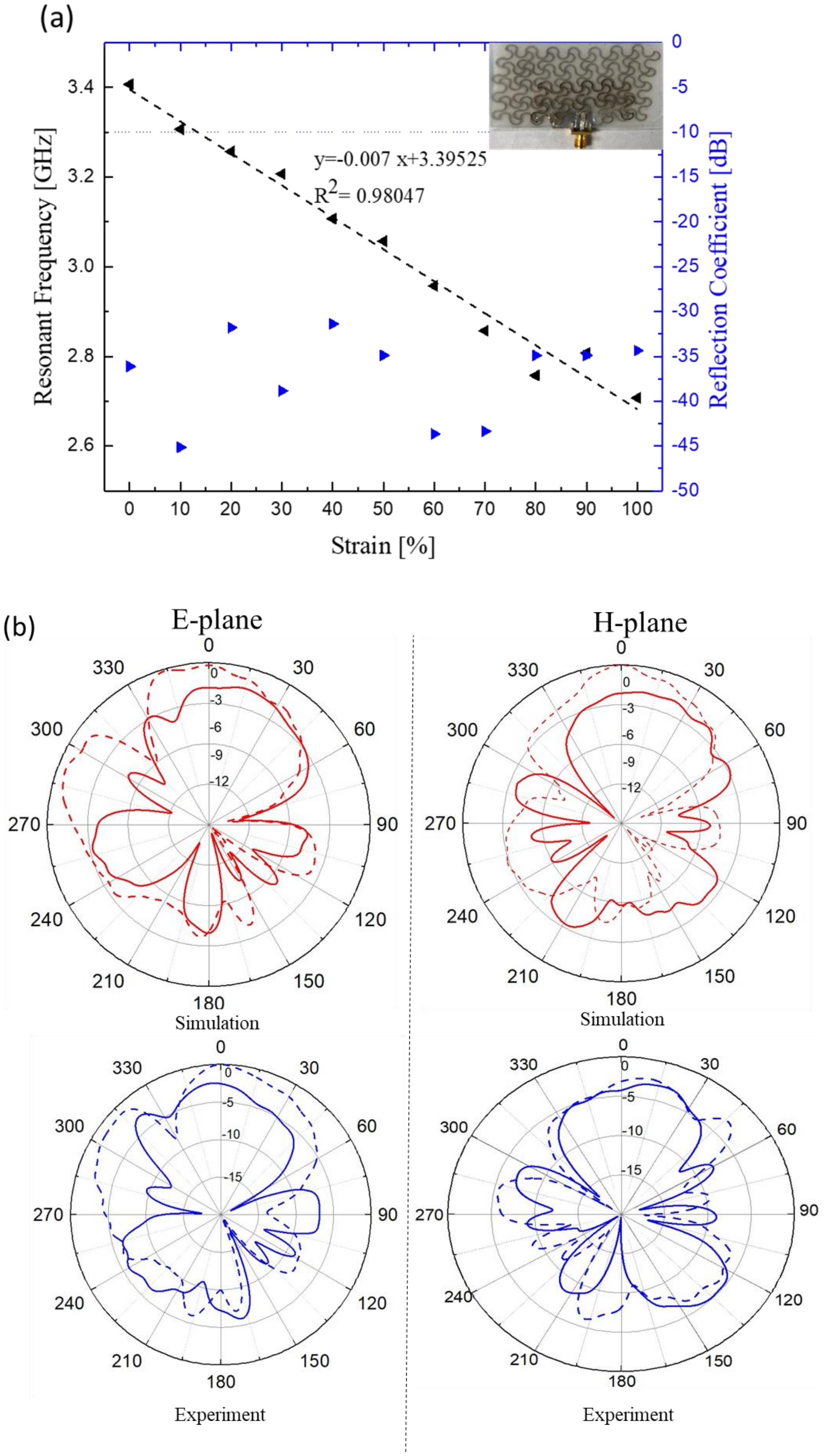

Figure 5-10 Textile meshed patch over meshed ground analysis: a) Change of resonant frequency and S_{11} as a function of tensile strain up to 100%. b) Comparison of the radiation pattern in E-plane (left) and H-plane (right) in relax ($f_{res=}$ 3.45 GHz) and 30% uniaxial strain ($f_{res=}$ 2.75 GHz). The simulation results of 30% strain (bottom) were extracted from the model obtained by DIC method at 30%. Solid lines and dash lines represent 0% and 30% strain respectively.

The EM characteristics of a fully meshed microstrip antenna (i.e. both patch and ground planes patterned using serpentine mesh) as a function of the tensile strain was also characterized. **Figure 5-10 (a)** shows that the resonant frequency shifted downwards linearly from 3.45 GHz to 2.75 GHz when the antenna was stretched from 0% up to 100% of uniaxial strain. These results indicate that the antenna could be used to measure large strain wirelessly (up to 100%) with an average sensitivity of 0.25 $(\frac{MHz}{mm})$. Whilst the inset feed line was designed to match the impedance for the solid microstrip antenna, it was observed that the same design implemented for the meshed versions maintained good impedance matching even over the 100% uniaxial strain (**Figure 5-10 (a)**). The radiation patterns in the E-plane and H-plane are shown at 3.45 GHz (0% strain) and 3.2 GHz (30% strain) in **Figure 5-10 (b)**. It can be observed that the half-power beamwidth of the proposed antenna is very wide, whereas the notable back lobe specifies that some power is lost as back radiation.

Comparison with the fabricated gold meshed-patch antenna, **Figure 5-11 (a)** shows that the resonance frequency (2.58 GHz) of gold meshed patch is lower than the textile-based counterpart antenna even if they have the same dimension ($f_{res=}$ 2.98 GHz). This is due to the structure of the textile, the actual electrical length of the patch in textile-based antenna is longer than in the gold antenna. Moreover, adjacent threads may create some reactive loads causing a shift in the resonance frequency. The silver-plated knitted textile contains a series of interlocking loops, so the actual electrical length is longer than the physical length. In addition, it was observed that applying uniaxial strain on the gold meshed-patch antenna did not have any notable effect on the resonant frequency as it happened for the textile version. In addition, it was observed that applying uniaxial strain on the gold meshed-patch antenna did not have any notable effect on the resonant frequency as it happened for the textile version (see **Figure 5-10 (a)**). Moreover, it was the sample was examined for stretchability and it could not withstand strains beyond 20%, the point at which cracks started to appear and the signal was lost.

The radiation patterns in the E-plane and H-plane (**Figure 5-11 (b)**) shows notable differences between this pattern and its textile-based counterpart. This could be explained due to the differences in the surface morphology between the silver-coated textile and gold, which cause a notable discrepancy in the surface current density on the patches. Indeed, it can be said that the knitted structure of the textile caused surface current phase cancelations in the loop yarn, thus not contributing to the far-field radiation.

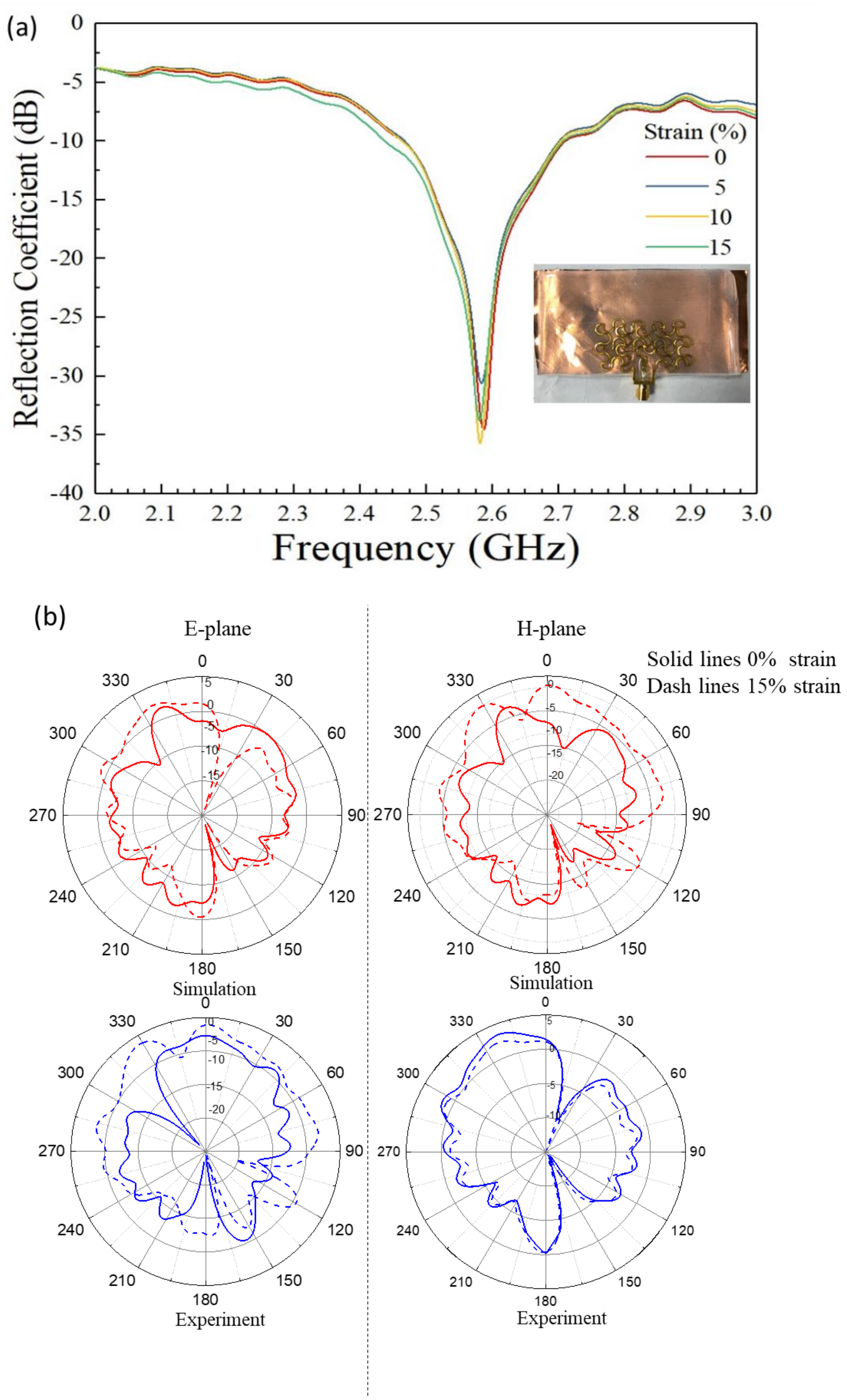

Figure 5-11 Gold meshed patch over a metallic solid ground analysis: (a) Measurement of S_{11} as a function of frequency as strain increase up to 15%. b) Comparison of the radiation pattern in E-plane (left) and H-plane (right) in relax ($f_{res=}$ 2.58 GHz) and 15% uniaxial strain ($f_{res=}$ 2.75 GHz). The simulation results of 15% strain (model obtained by DIC method at 15%) are compatible with the experimental results.

5.1.9 RF readout design and simulation

Considering the properties of the developed antenna in terms of flexibility, stretchability, wearability, and conformability, the device can be used as a mechanical strain sensor on curvilinear surfaces such as the human skin to monitor the movement of the human body. To this end, the fully meshed microstrip antenna was placed on the elbow for movement detection (**Figure 5-12**). Defining the bending angle (θ) as the angle between the arm and the forearm, the motion was captured by the decrease in the resonance frequency of the antenna.

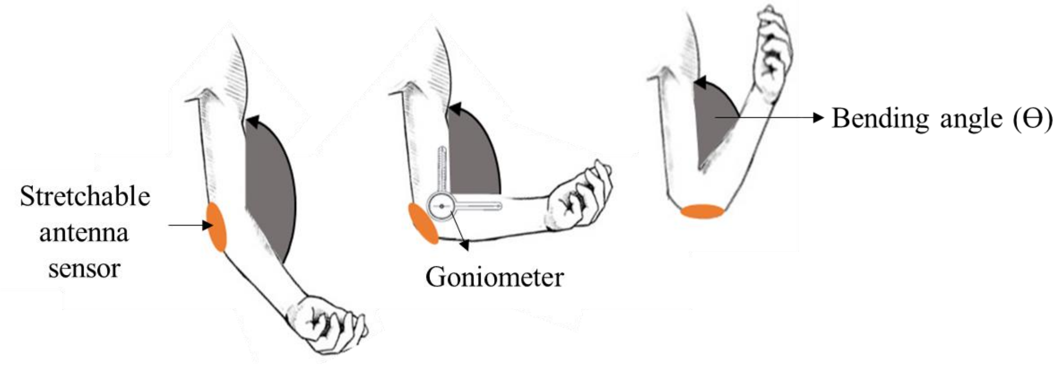

Figure 5-12 The stretchable antenna sensor attache to the elbow .The variation in the resonant frequency and DC voltage associated with the change of bending angles are studied.

A linear trend was observed when measuring the resonant frequency of the antenna for different bending angles ranging from 120º to 40º**.** This way of detecting the bending angle is also attractive for applications such as robotics and prosthetics, where wireless strain sensors can provide an accurate measure of joint angles, without adding to the traditional issue of wiring complexity. Further, it is possible to use the antenna as a mechanical strain sensor to remotely control the robotic movements in a manner (199). In such areas, the fully sensing antenna can provide feedback and trigger the actuator by converting the resonance frequency variation into a variation in DC voltage. This can be achieved by using an RF to DC rectifier (221). Once the information is processed (i.e., the change in the resonance frequency can be acquired and translated to a particular bending angle), it can be transferred to a robotic hand controller for movement control. **Figure 5-13 (a)** illustrates the block diagram of the readout RF circuit for the proposed sensing antenna. The output DC voltage can be used as an actuating signal.

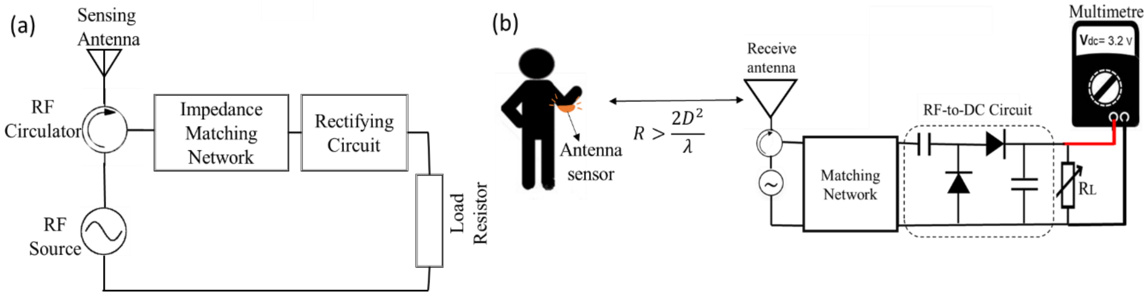

Figure 5-13 (a) Block diagram of the proposed readout circuit to convert frequency shift of stretchable sensing antenna to DC voltage. (b) Measurement setup to translate the bending angle of human arm to DC voltage wirelessly using the stretchable antenna.

In order to characterise the behaviour of the realized antenna under different stretching conditions, the VNA has been used to measure the S_{11} parameter and the amount of shift due to the stretch. The results of this characterisation are used to create a calibration curve as shown in **Figure 5-10**. However, for the implementation in real applications, an RF readout circuit has been proposed which converts the reflected power from the proposed antenna-sensor into a DC voltage by rectification. The VNA characterisation helped as well to identify the frequency range shift in order to design the RF readout circuit and to help select the appropriate RF diode. So, for potential applications the RF readout circuit is the one which is going to be used. The DC output represents the amount of stretch applied to the antenna and can be used to actuate other devices.

The reading principle to detect the deformation in a stretchable antenna is based on the measurement of reflected power from the sensing antenna. A detection circuit for the stretchable sensor antenna can be apprehended with an RF source that emits an RF signal at the resonance frequency of the antenna. The received reflected power can be directed by using a three-port circulator where the reflected power can be converted into a DC voltage using a RF rectifying circuit. Good impedance matching at the third port of the circulator ensures that the maximum power is transferred to rectifying circuit. The proposed setup in **Figure 5-13 (b)** enables to map the bending angle to DC voltage variation. The receiving antenna can be a microstrip patch antenna working at 3-4 GHz.

Advanced Design System (ADS, Keysight Technologies, Santa Clara, CA, USA) was used to simulate rectifier system along with impedance matching network (**Figure 5-14**). Considering the operating frequency range of the antenna, FR4 with a thickness of 20 mil is set as a substrate. The S-parameter touchstones files (at different bending angles), collected from the VNA in the previous experiment, were assigned to the schematic using Data Access Component (DAC). DAC component enables to sweep of multiple imported data files. A three-port RF circulator is a passive device designed by a Y junction symmetrical stripline coupled to a magnetic biased ferrite material. Once the RF signal generated using an RF source and the second port is well match (i.e. operating at the resonant frequency) majority of the emitted power (consider ideal circulator with negligible insertion loss) will be absorbed by the antenna. In this case, the reflected signal to the third port will be minimum. On the other hand, if the impedance is mismatched at the second point, in our case due to deformation of the antenna, the reflected power directed toward the third port will be greater. Good impedance matching at port three is key to direct maximum power to the rectifier circuit.

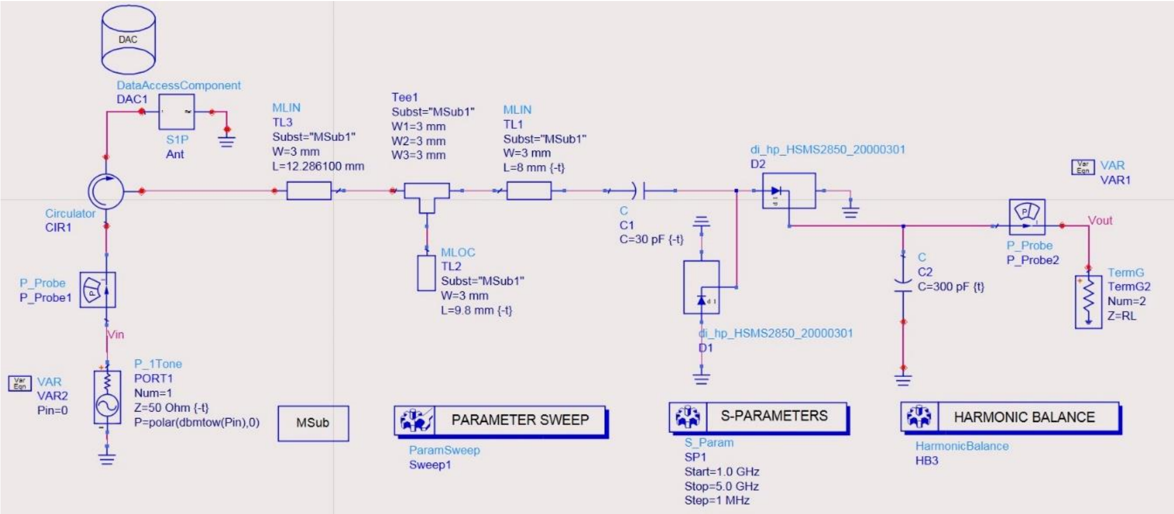

Figure 5-15 Schematic of the rectifying circuit using a single stage RF rectifier simulated in ADS.

The next step is to design L-network matching and a full-wave single-stage rectifier. The optimum lengths of the microstrip lines were calculated using LineCalc tool. Obtained parameters are summarized in **Table 5-1**. The widths of microstrip lines are 3 mm, compatible with conventional PCB fabrication processes. A T-junction between the transmission lines is considered with lines width match to the adjacent transmission lines to avoid parasitic junction effects. A T-junction between the transmission lines is considered with lines width match to the adjacent transmission lines to avoid parasitic junction effects.

Table 5-1 Optimal parameters of the discrete and lumped elements obtained using LineCalc, Optimization and Tuning tools in ADS.

Discrete elements	Length (mm)	Width (mm)	Lumped elements	Value
TL1	12.286	3	C1	30 pF
TL2	9.8	3	C2	300 pF
TL3	8	3	R_L	1-100 kΩ

Further, a full-wave rectifying circuit was designed using two HSMS-2850 diodes in a series configuration. HSMS-2850 is a Schottky detector diode with zero DC bias and high detection sensitivity and a low parasitic capacitance of 0.08 pF, suitable to use from 9.5 MHz to 5.8 GHz according to the manufacturer datasheet. The diode D1 is functional at the positive cycle where the Diode D2 is working at the negative cycle, storing energy in capacitor C1 and C2 respectively. A SOT-23 package with typical package inductance and capacitance of 2 nH and 0.08 pF is selected to be mount on the substrate. A parasitic series resistance of 10 Ω is chosen to modify the default characteristic of the diodes. The optimum values of distributed elements and capacitors are specified in **Table 5-1**. Since the diodes are nonlinear devices at microwave frequencies Harmonic-Balance (HB) method is performed to analyse the circuit. HB is a frequency domain simulator in which the linear devices of a circuit are modelled in the frequency domain where the nonlinear devices are modelled in the time domain and before each iteration are Fourier Transformed.

The conversion efficiency of the RF to DC is defined by

$$\eta = \frac{output\ power}{input\ power} \times 100 = \frac{V^2{}_{Dc}}{R_L \times P_r} \qquad (5\text{-}1)$$

which P_r is reflected power received in rectifying circuit. It is noted that the conversion efficiency is a function of the load resistor, and the received power. **Figure 5-16 (a)** shows the conversion efficiency at different input power levels of -20, -10 dBm, 0 dBm, and 10 dBm respectively. The conversion efficiency is increasing along with an increase in RF input power. At 0 dBm the efficiency is below 50% where the efficiency is at the highest obtained value of 71% at 10 dBm input power. Moreover, to achieve the peak output DC voltage, a load resistor is varying in the range of 1-100 kΩ to study the effect of load resistance on the output voltage and the efficiency. It was noted that for 75 kΩ, DC voltage is 4.6 V at 10 dBm however the efficiency is as low as 12%. Conversion efficiency against input power for some values of load resistor are depicted in **Figure 5-16 (b).** To find a trade-off between the output DC voltage and the efficiency the load resistor of 30 kΩ has been chosen for the rest of analysis.

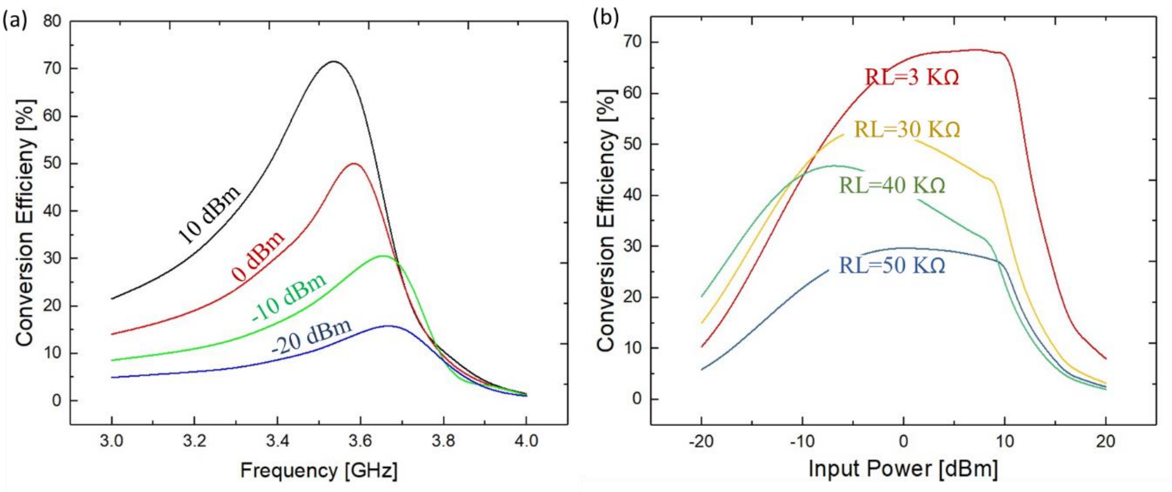

Figure 5-16 (a) The conversion efficiency at different input power levels of -20, -10 dBm, 0 dBm and 10 dBm respectively where the load resistor is 30 kΩ. (b) Conversion efficiency at different input powers for some values of load resistor.

Figure 5-17 shows the output DC voltage variation of the proposed design for load resistance of 30 kΩ where the input power is set at 0 dBm. The simulated maximum value of V_{dc}= 3.5 V is realized when the input data of the sensing antenna is associated with 20° bending of a human hand. The graph shows that in a rest position the DC voltage is minimum, however, the voltage is increasing when the hand is folded. Thus, reported work can lead to remote actuation of a robotic arm to mimic the human hand movement in real life situation. It means the performed movement by a person who is wearing the stretchable antenna could be reflected by a robot.

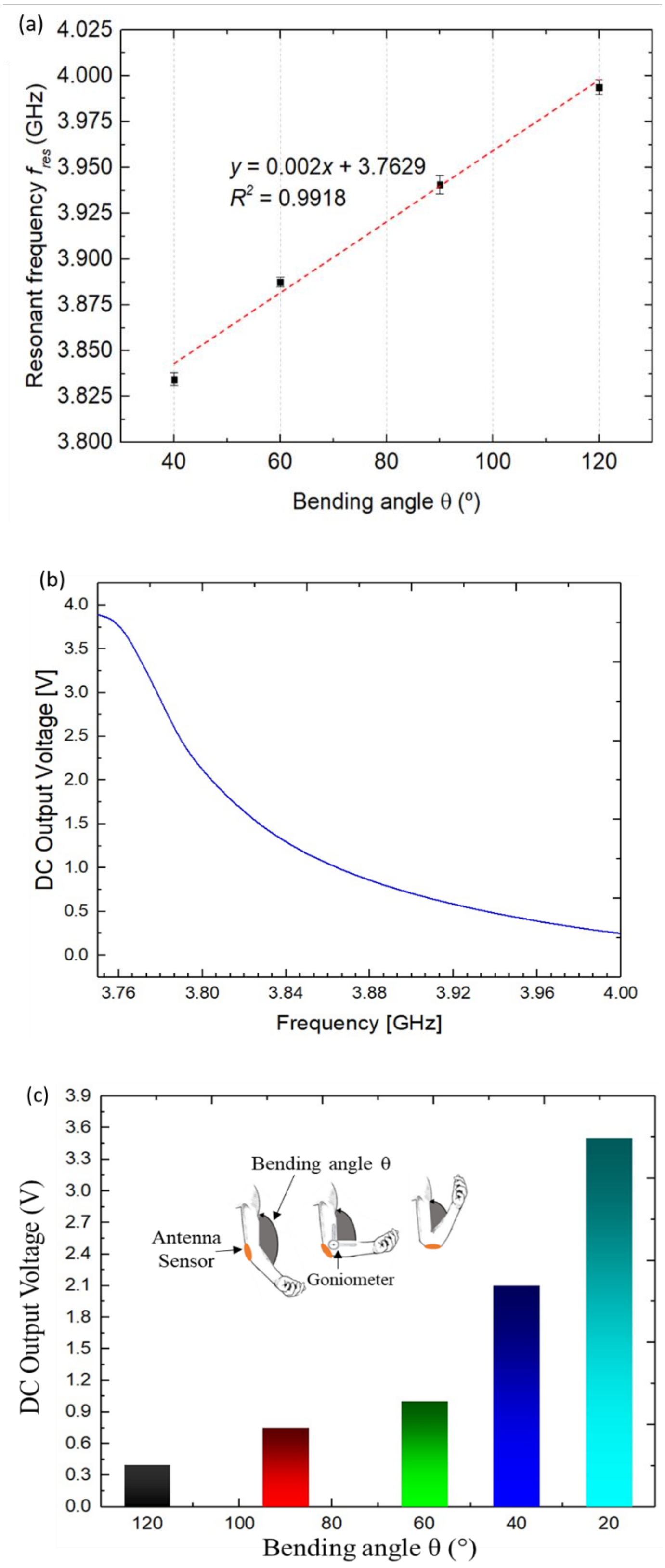

Figure 5-17 (a) Change in the resonant frequency of the antenna attached to the elbow for different bending angles. The variation in the resonant frequency follows a linear trend for the tested bending angles. (b) Simulated output DC voltage at input power of 0 dBm. (c) Variation of produced DC voltage associated with the change of bending angles.

5.2 Stretchable RFID sensor – taking advantage of intrinsic property of material

In the section 5.1 we explored embedding sensing capability in an antenna and results demonstrates that it is possible to encode sensing parameter in a characteristic of an antenna such as resonant frequency. In order to design an UHF RFID tag which has sensing capability similar to the one explained, here we present a UHF RFID strain sensor tag using stretchable textile in the main body of the antenna inlay. This method could add sensing capability along with conformability to RFID garment tags which are already used in clothing industry.

5.2.1 Integrating conductive textile to commercial UHF RFID

The commercial tag I have used for this purpose is Smartrac Dogbone sensor[8] which is a passive UHF single-chip sensor, operating at 860-960 MHz. To add stretchability to the tag, the body of the tag was cut as shown in **Figure 5-17** and a stretchable conductive textile was replaced to those sections using a conductive glue. The polyethylene coating layer of the tag was removed carefully using a scalpel in order to access the conductive body of the antenna tag. The two section of the antenna which was removed then was replaced by a stretchable commercial silver-plated knitted textile (MedTex, UK) using a silver paste. After the silver paste was cured, connections were secured using a conductive epoxy glue. A multimetre was used to check all sections are connected well. The realized tag was molded and Ecoflex was poured to cover the tag completely. After 30 mins, the tag was removed from the mold and the stretchability of the tag was checked. The tag was stretchable up to 25%.

---

[8] Thanks to Smartrac company for proving free RFID tags.

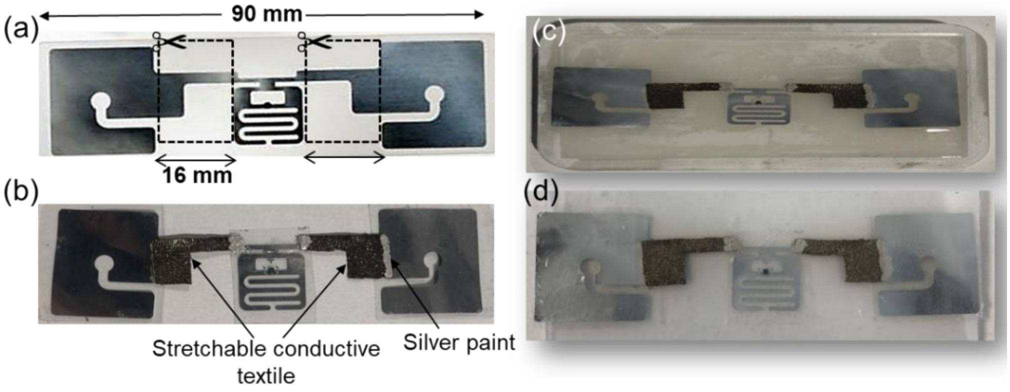

Figure 5-18 Fabrication steps to assemble stretchable textile to the Smartrac RFID tag.

5.2.2 Wireless readout

UHF RFID systems usually operates from 860 MHz to 960 MHz depends on regional regulations. For example, 866–869 MHz band is assigned to Europe, 940–943 MHz to China and 902–928 MHz to US. Tagformance Pro (Voyantic Ltd, Finland) is used to characterize the proposed tag in terms of backscattered power and reading range. **Figure 5-18** shows the measurement setup which consists Tagformance unit connected to a linear polarized antenna (reader antenna). The tag is placed on a foam spacer to maintain the fixed distance that setup was calibrated based on that, prior to the measurement.

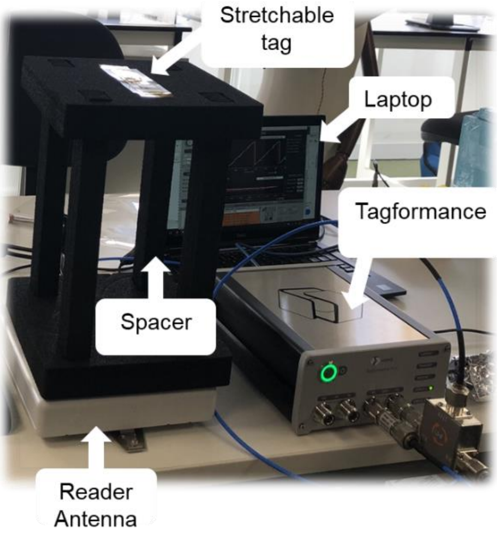

Figure 5-19 Tagformance Pro setup to characterize UHF RFID tags.

We measure the backscattered power of the stretchable tag to check whether the response is function of the antenna elongation. **Figure 5-19** shows the backscattered power is increasing when the uniaxial elongation increased up to 25%. This trend covers the entire band of UHF RFID (860-960 MHz) however, the relation is not linear with the tag elongation.

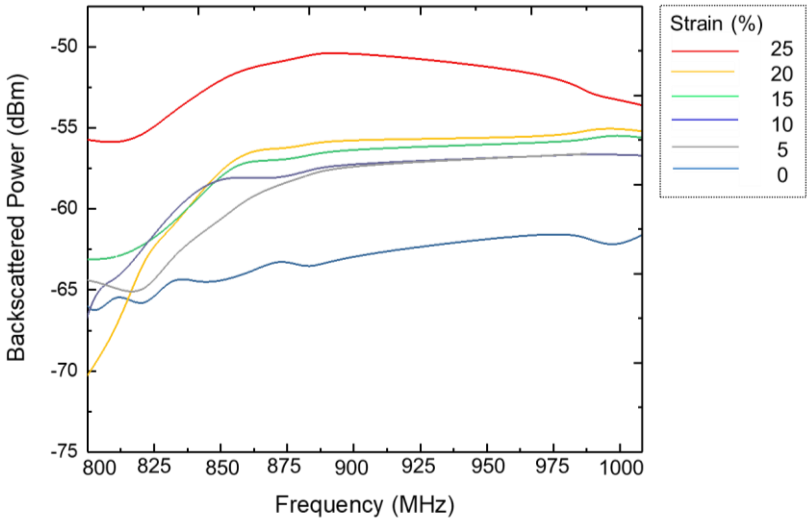

Figure 5-20 The backscattered power signal from the stretchable UHF tag corresponding to different uniaxial strains.

Reading range can be considered as a sensing indicator as well. In this regard, we measured the read range versus frequency. **Figure 5-20** shows that the maximum read range that occurs close to 900 MHz as the original (commercial) tag before tailoring, however the reading range drops by almost 4 m compared to the original tag. The reading range was increasing almost linear when the stretchable tag was elongated up to 25% by 50 cm at frequency range of 860-960 MHz.

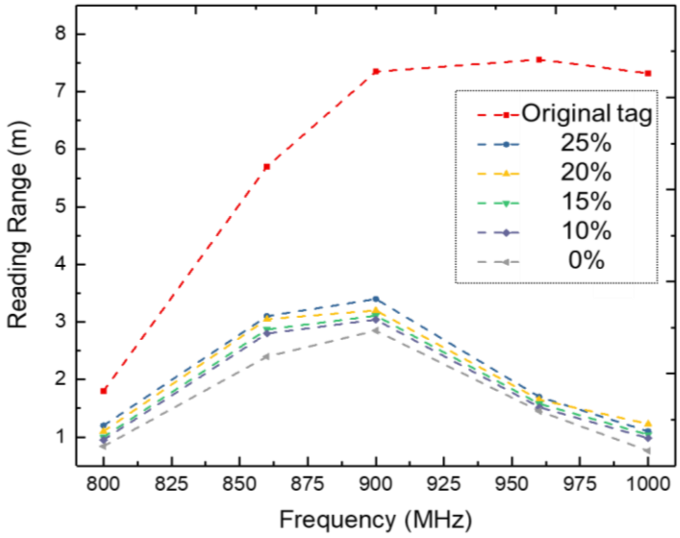

Figure 5-21 Reading range of the stretchable RFID tag corresponding to different uniaxial strains. The read range of the commercial tag is shown with red graph over the range of frequency of 800-1000 MHz.

Overall, the results show that it is possible to design a stretchable RFID tag with strain sensing capability, taking advantage of intrinsic property of the conductive textile. In this short study, we tailored the design of the commercial UHF RFID tag in a way to make it partially stretchable. These initial results suggest that designing a stretchable sensing RFID using a stretchable material for instance conductive textiles or stretchable inks/pastes could be a solution to manufacture sensing-enabled smart labels for garments and food monitoring applications.

5.3 Summary

In this work, three versions of textile-based microstrip antennas have been designed, fabricated, and characterized. The antenna patch has a mesh structure over meshed and unmeshed ground plane ground planes using conductive textile. The EM characteristics of the meshed patch antenna were compared with its metallic counterpart fabricated with lithography. The meshed patch over solid/meshed ground plane demonstrated high stretchability (up to 40% and 100%, respectively) upon the uniaxial tensile strain. Both antennas presented a linear trend of their resonant frequency shift in response to increasing elongation, with experimental sensitivities of 0.2 and 0.25, respectively. Radiation patterns were also characterized upon the uniaxial tensile strain. 2D DIC technique was implemented as a model for the deformed antennas to validate experimental results with FE simulation. As a proof-of-concept, the fully meshed antenna is shown to predict the joint angle of a human hand, which could potentially be extended to remotely control the robotic hand. Once the information is processed (i.e., the change in the resonance frequency is acquired and translated to a particular bending angle), it can be transferred to a robotic hand controller for the movement of a robotic arm. A rectifying circuit including two Schottky diodes (HSMS-2850) and an L-matching network is simulated in ADS to convert RF signal to DC voltage. The proposed design obtained a conversion efficiency of 71% at 10 dBm input power over the load resistor of 3 kΩ. The obtained results indicate that stretchable antennas can be designed and fabricated using conductive textile with several advantages such as low cost, easy integration into fashion garments, and self-strain sensing capabilities. In this way, the number of components attached to the garments can be reduced since the transmitting antenna is also used as a strain sensor.

Moreover, a short study also was conducted in order to evaluate the possibility of integrating stretchable conductive textile to a commercial UHF RFID tag, taking advantage of intrinsic property of the conductive textile. In this short study, we tailored the design of the commercial UHF RFID by replacing the main body of the antenna with a stretchable conductive textile. This insight suggests we can design stretchable sensing RFIDs with at desire frequency with optimized reading range to be a solution for sensing-enabled smart labels in garments industry and food monitoring applications.

Chapter 6. Conclusion

The increasing use of wearable systems for wellness and health monitoring applications have directed the attention of researchers towards wireless sensor networks (WSNs) for real-time measurement of physiological parameters such as heart rate, body temperature, strain, body motions, etc. Some of these wireless sensors also find application in humanoid robotics, prosthetics, and human-machine interactions, particularly to address the issue of wiring complexity. The flexibility, conformability and more and more functional device have been the trend in recent years to meet the key requirements of these applications. However, the wiring required to acquire the data is prone to damage, for example during bending in wearable systems, and may lead to interferences between parallel signals as well as time delays. Likewise, the increasing number of devices also raises integration challenges, in addition to traditional challenges such as higher cost and power requirements. Considering these challenges, a system with a similar level of functionality (as with many nodes and sensors) and yet less complexity is much needed. Multifunctionality (e.g. communication as well as sensing) with commonly used devices such as antennas could be an interesting way forward. This has been demonstrated using different approaches and various fabrication methods. The key findings and contributions in this thesis are summarized and future work based on the findings is suggested.

6.1 Key Findings

In the context of this thesis, three approaches of presented mechanisms are examined to develop different antennas with sensing capability. Antenna sensors are designed using flexible/stretchable materials to provide conformability to users in wearable applications.

In the first approach, the focus was on developing the NFC based sensing tag, using the capability of the NFC RFID chip to integrate an external sensor to achieve a complete battery-less sensing platform. The main purpose of this work is to fabricate a cost-effective NFC sensing tag which is suitable for green electronic applications as degradable substrate. Additive manufacturing technique (screen printing) was implemented to reduce material waste (e-waste) associated with conventional copper etching for standard PCBs. Moreover, paper as low cost, easy to recycle and biodegradable substrate was chosen to reduce the cost of each tag. Subsequently, two flexible resistive sensors developed in the group were integrated. The temperature and strain values of those flexible sensors were converted to voltage values and reading carried out by NFC enabled smartphone. The circuit components were tailored in order to demonstrate two potential applications for the developed sensing tag: smart bandage serving in wound monitoring and smart food packaging. With studies showing a body temperature of 35- 38 °C encourages wound healing, the bandage can also measure the patient's temperature and send readings to a healthcare provider via a smartphone app. Temperature and strain are also two parameters that are rarely combined for wound assessment, making smart bandages one of the most innovative wearable devices to enter the healthcare industry. Some of these key applications have been tested however collaboration with clinicians are needed to translate the device’s use into real practice, a process which takes a few years dependent on approvals. Video demonstration (115) shows that either the temperature or strain reading are not interfering the other one reading.

In the second approach, the focus was on realization of antenna sensor using functional materials. In the first study, a parallel inductor-capacitor resonant tank was developed on dielectric sensitive material and sensing method is based on the change in resonance frequency of the LC resonator when exposed to different level of pressure. The LC tank was screen-printed on electrospun Poly-L-lactide (PLLA) nanofibers-based flexible, biocompatible, and piezoelectric substrate. A pressure ranges from 0 to 16 kPa has been tested. The interdigitated capacitive sensor (part of LC tank) exhibited high sensitivity 0.035 kPa^{-1} (wire measurement characterizing the capacitor using LCR meter) and 1200 Hz/kPa in wireless measurement with excellent durability (over 1800 cycles). The LC tank-based sensor is integrated on a compression bandage to demonstrate its potential use in the monitoring of sub-bandage pressure, which could help regulate blood flow at wound site and hence accelerate the healing process. Subsequently, similar to the first study, that using functional material for realization of sensing antenna was explored a loop antenna as a temperature sensor was designed however instead of exploiting a dielectric material, the conductive body of the antenna itself has been considered as a functional material. In this regard, a small part of a loop antenna which originally was printed using sliver paste was replaced using Poly(3,4-ethylenedioxythiophene): polystyrene (PEDOT: PSS) which is one of the most stable conductive polymers. The sensing mechanism was based on study the resonant frequency of the antenna when the temperature changes from 25 ºC to 90 ºC.

In the third approach, the focus was on realization of antenna sensing exploiting geometry modifications. In this case the external stimuli (e.g., stretching or bending) can be mapped through studying properties of the antenna. To do so, several textile-based stretchable microstrip patch have been developed using rectangular serpentine units. The changes in the resonant frequency of the meshed antennas, as a result of stretching, have been exploited to demonstrate the intrinsic uniaxial strain sensing. The obtained results indicate that resonant frequency decreases linearly with increasing applied strain, suggesting that the designed antennas can also be used as strain sensors with stretchability up to 100% and a sensitivity of 0.25. The results were validated through full-wave electromagnetic simulations and a two-dimensional Digital Image Correlation (DIC) technique to model the antenna deformations during the tensile tests. In terms of stretchability, the meshed textile patch antenna on a solid ground plane showed more than a 2-fold improvement compared to a meshed gold patch antenna, showing linear frequency shift. As potential applications, we demonstrate the use of a highly deformable fully meshed textile antenna as a strain sensor capable of measuring joint angles of a human limb. To do that, a novel microwave readout circuit based on RF to DC rectifier was designed.

One important aspect for realisation of antenna sensor using smart materials with intrinsic sensing capability is that fractional change in resonant frequency is happening due to the variation of dielectric constant or magnetic permeability in response to the external stimuli. To avoid problem of selectivity, the material properties (permittivity or permeability) should not be sensitive to more than one stimulus or there must be a way to separate the responses due to multiple stimuli. The same applies to textile antenna sensor presented in this thesis. The properties of antenna (e.g. operation frequency, gain, etc.) are sensitive to backscattered signals from surrounding environment. These EM interferences can degrade the backscattered signal from the antenna sensor. Although change in resonant frequency due to desirable mechanical deformation can be observed but in real life application (e.g. using the antenna sensor for human-robot interaction) it is complicated to distinguish the subtle desirable stimulus from unwanted backscattered signals.

One drawback in using flexible materials to fabricate antennas is the flexibility of the wearable device can negatively affect the wireless communication, as the signal transmission and reception are achieved by antennas. The electromagnetic properties of the antennas are sensitive to the geometric deformations when the flexible device is attached to human body due to the curvilinear nature of the body. In addition, the motion of the human body will cause undesirable geometric modification of the antenna structure which results in a continuous alteration of the antenna profile where it can affect the directivity, gain and the operation frequency of the antenna (148, 222).

6.2 Future Research Directions

The focus of this thesis has been on analysing flexible/stretchable antennas acting as sensors exploiting the intrinsic properties of materials. Further improvements are possible in each individual work to improve the system in terms of communication charactristic of the antennas. The long-term future plan would be focused on increasing efficiency of the antenna sensors. However, as short-term plans to improve the presented antenna sensors, some suggestions are listed:

As for NFC based sensing RFID tag, presented in chapter 3, unlike conventional soldering method which bonds effectively SMD components on rigid and flexible PCBs, the paper as substrate cannot sustain high temperature required for soldering. Instead low-temperature solder paste was used, however, robust electrical bonding with stable mechanical attachment of the SMD components for long term stability needs to be further investigated. Thinning a bare die NFC chip to make the chip flexible could be a potential solution to improve mechanical stability of the fully flexible tag. Furthermore, the printed NFC tag can be encapsulated with thermoplastic polyurethane (TPU). Waterproof TPU protects the skin mounted tag against body fluids and moisture in wound monitoring application. Due to soft nature of TPU, the encapsulation also enhances the conformability of the tag. One important point is to replaced silver paste that was mainly used to print antenna sensors with new formulated inks/pastes to reduce the cost of each tag.

As for the printed LC resonator, presented in chapter 4, we can expand the application of such device towards wound healing as PLLA is biodegradable piezoelectric material. In that case, the patch will be in direct contact with open wound hence all materials should be biocompatible. Thus, the silver paste should be replaced by conductive biocompatible ink for instance PEDOT: PSS. For this scenario, miniaturization of the LC resonator is preliminary step. However, it should be considered that miniaturising the tag may not be the best choice as it effects the quality factor of the coil antenna.

As for the stretchable textile-based antenna sensor, one of the key advantages to design an antenna with ground plane for wearable applications is to eliminate the detuning effect of the host object (e.g., human body or metallic surface). The meshed ground plane used in fully meshed microstrip antenna helped to improve stretchability of the antenna strain sensor. This modification led to increase in back lobe radiation thus the antenna efficiency decreased. Introducing periodic metal patches on top of the ground plane (with optimum distance) can form a cavity-type high impedance surface (HIS). The properties of the HIS allows the reflected wave will be in phase with incident wave, so the back radiation reduces. Due to periodic nature of the HIS it does not limit the stretchability of the antenna but it significantly improves the detection probability due to higher back scattered power. Moreover, the properties of the HIS allows to further decrease the thickness of the polymeric substrate which is highly desirable for wearable applications.

Bibliography

1. Park S, Vosguerichian M, Bao Z. A review of fabrication and applications of carbon nanotube film-based flexible electronics. Nanoscale. 2013;5(5):1727-52.

2. Nathan A, Ahnood A, Cole MT, Lee S, Suzuki Y, Hiralal P, et al. Flexible electronics: the next ubiquitous platform. Proceedings of the IEEE. 2012;100(Special Centennial Issue):1486-517.

3. Xin Q, Meng S, Fengyu L, Yanlin S. Research progress in flexible wearable electronic sensors. 2016.

4. Stoppa M, Chiolerio A. Wearable electronics and smart textiles: A critical review. sensors. 2014;14(7):11957-92.

5. Ju H, Jeong J, Kwak P, Kwon M, Lee J. Robotic flexible electronics with self-bendable films. Soft robotics. 2018;5(6):710-7.

6. He H, Fu Y, Zang W, Wang Q, Xing L, Zhang Y, et al. A flexible self-powered T-ZnO/PVDF/fabric electronic-skin with multi-functions of tactile-perception, atmosphere-detection and self-clean. Nano Energy. 2017;31:37-48.

7. Velázquez R. Wearable assistive devices for the blind. Wearable and autonomous biomedical devices and systems for smart environment: Springer; 2010. p. 331-49.

8. Kim H, Kwon YT, Lim HR, Kim JH, Kim YS, Yeo WH. Recent Advances in Wearable Sensors and Integrated Functional Devices for Virtual and Augmented Reality Applications. Advanced Functional Materials. 2020:2005692.

9. Wang J, Coleman DC, Kanter J, Ummer B, Siminerio L. Connecting smartphone and wearable fitness tracker data with a nationally used electronic health record system for diabetes education to facilitate behavioral goal monitoring in diabetes care: protocol for a pragmatic multi-site randomized trial. JMIR research protocols. 2018;7(4):e10009.

10. Seesaard T, Lorwongtragool P, Kerdcharoen T. Development of fabric-based chemical gas sensors for use as wearable electronic noses. Sensors. 2015;15(1):1885-902.

11. Jeon J-Y, Ha T-J. Waterproof electronic-bandage with tunable sensitivity for wearable strain sensors. ACS applied materials & interfaces. 2016;8(4):2866-71.

12. Liu C, Huang N, Xu F, Tong J, Chen Z, Gui X, et al. 3D printing technologies for flexible tactile sensors toward wearable electronics and electronic skin. Polymers. 2018;10(6):629.

13. Silva AF, Tavakoli M. Domiciliary Hospitalization through Wearable Biomonitoring Patches: Recent Advances, Technical Challenges, and the Relation to Covid-19. Sensors. 2020;20(23):6835.

14. Heo SY, Kim J, Gutruf P, Banks A, Wei P, Pielak R, et al. Wireless, battery-free, flexible, miniaturized dosimeters monitor exposure to solar radiation and to light for phototherapy. Science translational medicine. 2018;10(470).

15. Han S, Kim J, Won SM, Ma Y, Kang D, Xie Z, et al. Battery-free, wireless sensors for full-body pressure and temperature mapping. Science translational medicine. 2018;10(435).

16. Dahiya R, Yogeswaran N, Liu F, Manjakkal L, Burdet E, Hayward V, et al. Large-area soft e-skin: The challenges beyond sensor designs. Proceedings of the IEEE.

2019;107(10):2016-33.

17. Chen K, Ren J, Chen C, Xu W, Zhang S. Safety and effectiveness evaluation of flexible electronic materials for next generation wearable and implantable medical devices. Nano Today. 2020;35:100939.

18. Zheng Y-L, Ding X-R, Poon CCY, Lo BPL, Zhang H, Zhou X-L, et al. Unobtrusive sensing and wearable devices for health informatics. IEEE Transactions on Biomedical Engineering. 2014;61(5):1538-54.

19. Li H, Xiao Y, Jin L. Recent Development of Wearable Electrochemical Sensors for Sweat Analysis. INTERNATIONAL JOURNAL OF ELECTROCHEMICAL SCIENCE. 2020;15(11):11997-2006.

20. Yu Y, Peng S, Blanloeuil P, Wu S, Wang CH. Wearable Temperature Sensors with Enhanced Sensitivity by Engineering Microcrack Morphology in PEDOT: PSS–PDMS Sensors. ACS Applied Materials & Interfaces. 2020;12(32):36578-88.

21. Yue N, Claes S. Wearable sensors for smart abnormal heart rate detection during skiing. Internet Technology Letters. 2021;4(3):e230.

22. Pimentel MA, Charlton PH, Clifton DA. Probabilistic estimation of respiratory rate from wearable sensors. Wearable electronics sensors: Springer; 2015. p. 241-62.

23. Wang S, Fang Y, He H, Zhang L, Li Ca, Ouyang J. Wearable Stretchable Dry and Self‐Adhesive Strain Sensors with Conformal Contact to Skin for High‐Quality Motion Monitoring. Advanced Functional Materials. 2021;31(5):2007495.

24. Amjadi M, Kyung KU, Park I, Sitti M. Stretchable, skin‐mountable, and wearable strain sensors and their potential applications: a review. Advanced Functional Materials. 2016;26(11):1678-98.

25. Manjakkal L, Dervin S, Dahiya R. Flexible potentiometric pH sensors for wearable systems. RSC Advances. 2020;10(15):8594-617.

26. Vogel RI, Nagler RH, Ahmed RL, Brown K, Luo X, Martinson BC, et al. UVR-sensor wearable device intervention to improve sun behaviors and reduce sunburns in melanoma survivors: study protocol of a parallel-group randomized controlled trial. Trials. 2020;21(1):1-12.

27. Deng Y, Chen C, Xian X, Tsow F, Verma G, McConnell R, et al. A novel wireless wearable volatile organic compound (VOC) monitoring device with disposable sensors. Sensors. 2016;16(12):2060.

28. Spirjakin D, Baranov A, Akbari S. Wearable wireless sensor system with RF remote activation for gas monitoring applications. IEEE Sensors Journal. 2018;18(7):2976-82.

29. Magno M, Brunelli D, Sigrist L, Andri R, Cavigelli L, Gomez A, et al. InfiniTime: Multi-sensor wearable bracelet with human body harvesting. Sustainable Computing: Informatics and Systems. 2016;11:38-49.

30. Dahiya R. E-skin: from humanoids to humans [point of view]. Proceedings of the IEEE. 2019;107(2):247-52.

31. Palmroth A, Salpavaara T, Vuoristo P, Karjalainen S, Kääriäinen T, Miettinen S, et al. Materials and Orthopedic Applications for Bioresorbable Inductively Coupled Resonance Sensors. ACS applied materials & interfaces. 2020;12(28):31148-61.

32. Stutzman WL, Thiele GA. Antenna theory and design: John Wiley & Sons; 2012.

33. Koulouridis S, Psychoudakis D, Volakis JL. Multiobjective optimal antenna design

based on volumetric material optimization. IEEE Transactions on antennas and propagation. 2007;55(3):594-603.

34. Balanis CA. Antenna theory: analysis and design: John wiley & sons; 2015.

35. Pozar DM. Microwave engineering: John wiley & sons; 2011.

36. Yang L, Zhang R, Staiculescu D, Wong C, Tentzeris MM. A novel conformal RFID-enabled module utilizing inkjet-printed antennas and carbon nanotubes for gas-detection applications. IEEE Antennas and Wireless Propagation Letters. 2009;8:653-6.

37. Nair RS, Perret E, Tedjini S, Baron T. A group-delay-based chipless RFID humidity tag sensor using silicon nanowires. IEEE Antennas and Wireless Propagation Letters. 2013;12:729-32.

38. Occhiuzzi C, Contri G, Marrocco G. Design of implanted RFID tags for passive sensing of human body: The STENTag. IEEE Transactions on Antennas and Propagation. 2012;60(7):3146-54.

39. Jun J, Oh J, Shin DH, Kim SG, Lee JS, Kim W, et al. Wireless, room temperature volatile organic compound sensor based on polypyrrole nanoparticle immobilized ultrahigh frequency radio frequency identification tag. ACS applied materials & interfaces. 2016;8(48):33139-47.

40. Gagnadre I, Gagnadre C, Fenelon J. Circular patch antenna sensor for moisture content measurement on dielectric material. Electronics Letters. 1995;31(14):1167-8.

41. Hasan MN, Tamanna S, Singh P, Nadeem MD, Rudramuni M, editors. Cylindrical dielectric resonator antenna sensor for non-invasive glucose sensing application. 2019 6th International Conference on Signal Processing and Integrated Networks (SPIN); 2019: IEEE.

42. Lui K, Murphy O, Toumazou C. A wearable wideband circularly polarized textile antenna for effective power transmission on a wirelessly-powered sensor platform. IEEE transactions on antennas and propagation. 2013;61(7):3873-6.

43. El Matbouly H, Tedjini S, Zannas K, Duroc Y. Compact multi bit slotted C-Scatterer for threshold sensitive chipless wireless temperature sensor. Technologies. 2018;6(3):59.

44. Ahmed S, Tahir FA, Shamim A, Cheema HM. A compact kapton-based inkjet-printed multiband antenna for flexible wireless devices. IEEE Antennas and Wireless Propagation Letters. 2015;14:1802-5.

45. Dahalan A, Aziz M, Othman M, Nornikman H, Ibrahim S. Kapton Based Antenna Simulation Analysis for Smart System. International Journal of Integrated Engineering. 2019;11(4).

46. Bhattacharjee M, Nikbakhtnasrabadi F, Dahiya R. Printed Chipless Antenna as Flexible Temperature Sensor. IEEE Internet of Things Journal. 2021;8(6):5101-10.

47. Groenendaal L, Jonas F, Freitag D, Pielartzik H, Reynolds JR. Poly (3, 4 ‐ ethylenedioxythiophene) and its derivatives: past, present, and future. Advanced materials. 2000;12(7):481-94.

48. Zahir H, Wojkiewicz JL, Alexander P, Kone L, Belkacem B, Bergheul S, et al. Design fabrication and characterisation of polyaniline and multiwall carbon nanotubes composites ‐ based patch antenna. IET Microwaves, Antennas & Propagation. 2016;10(1):88-93.

49. Son H-W, Jeon H-G, Cho J-H. Flexible wideband UHF RFID tag antenna for curved metal surfaces. Electronics letters. 2012;48(13):749-50.

50. Golda RA, Marikani A, Alex EJ. Effect of Ceramic Fillers on the Dielectric, Ferroelectric and Magnetic Properties of Polymer Nanocomposites for Flexible Electronics. Journal of Electronic Materials. 2021;50(6):3652-67.

51. Kroupa J, Fousek J, Ivanov N, Březina B, Lhotská V. Dielectric study of the phase transition in phenanthrene. Ferroelectrics. 1988;79(1):189-92.

52. Holden DA, Ng D, Guillet JE. Studies of the antenna effect in polymer molecules V. Determination of the extent of singlet energy migration in a phenanthrene—Containing polymer by fluorescence quenching. British Polymer Journal. 1982;14(4):159-62.

53. Honda H, Onoda‐Yamamuro N, Ishimaru SI, Ikeda R, Yamamuro O, Matsuo T. Dielectric study on ionic orientational disorder in the low‐temperature phases of ionic plastic crystal KNO2. Berichte der Bunsengesellschaft für physikalische Chemie. 1998;102(2):148-51.

54. Outaleb N, Pinel J, Drissi M, Bonnaud O. Microwave planar antenna with RF‐sputtered indium tin oxide films. Microwave and Optical Technology Letters. 2000;24(1):3-7.

55. Poliks MD, Sung Y-L, Lombardi J, Malay R, Dederick J, Westgate C, et al., editors. Transparent antennas for wireless systems based on patterned indium tin oxide and flexible glass. 2017 IEEE 67th Electronic Components and Technology Conference (ECTC); 2017: IEEE.

56. Awalludin M, Ali M, Mamat M, editors. Transparent antenna using aluminum doped zinc oxide for wireless application. 2015 IEEE Symposium on Computer Applications & Industrial Electronics (ISCAIE); 2015: IEEE.

57. Ellmer K, Mientus R. Carrier transport in polycrystalline transparent conductive oxides: A comparative study of zinc oxide and indium oxide. Thin solid films. 2008;516(14):4620-7.

58. Hotte D, Siragusa R, Duroc Y, Tedjini S, editors. A humidity sensor based on V-band slotted waveguide antenna array. 2017 IEEE MTT-S International Microwave Symposium (IMS); 2017: IEEE.

59. Chang K, Kim Y-H, Kim Y-J, Yoon YJ. Functional antenna integrated with relative humidity sensor using synthesised polyimide for passive RFID sensing. Electronics letters. 2007;43(5):259-60.

60. Amin Y, Feng Y, Chen Q, Zheng L-R, Tenhunen H. RFID antenna humidity sensor co-design for USN applications. IEICE Electronics Express. 2013;10(4):20130003-.

61. Carvajal MA, Escobedo P, Martinez-Olmos A, Palma AJ. Readout circuit with improved sensitivity for contactless LC sensing tags. IEEE Sensors Journal. 2019;20(2):885-91.

62. Mahendia S, Goyal PK, Tomar AK, Chahal RP, Kumar S. Study of dielectric behavior and charge conduction mechanism of Poly (Vinyl alcohol)(PVA)-Copper (Cu) and Gold (Au) nanocomposites as a bio-resorbable material for organic electronics. Journal of Electronic Materials. 2016;45(10):5418-26.

63. Sengwa R, Sankhla S. Dielectric dispersion study of coexisting phases of aqueous polymeric solution: Poly (vinyl alcohol)+ poly (vinyl pyrrolidone) two-phase systems. Polymer. 2007;48(9):2737-44.

64. Amin EM, Saha JK, Karmakar NC. Smart sensing materials for low-cost chipless RFID sensor. IEEE Sensors Journal. 2014;14(7):2198-207.

65. Sidek R, Yusof F, Yasin F, Wagiran R, Ahmadun F, editors. Electrical response of multi-walled carbon nanotubes to ammonia and carbon dioxide. 2010 IEEE International Conference on Semiconductor Electronics (ICSE2010); 2010: IEEE.

66. Yoo K-P, Kwon K-H, Min N-K, Lee MJ, Lee CJ. Effects of O2 plasma treatment on NH3 sensing characteristics of multiwall carbon nanotube/polyaniline composite films. Sensors and Actuators B: Chemical. 2009;143(1):333-40.

67. Maheswaran R, Shanmugavel BP. A Critical Review of the Role of Carbon Nanotubes in the Progress of Next-Generation Electronic Applications. Journal of Electronic Materials. 2022:1-15.

68. Hosseini Z, Mortezaali A. Room temperature H2S gas sensor based on rather aligned ZnO nanorods with flower-like structures. Sensors and Actuators B: Chemical. 2015;207:865-71.

69. Bie L-J, Yan X-N, Yin J, Duan Y-Q, Yuan Z-H. Nanopillar ZnO gas sensor for hydrogen and ethanol. Sensors and Actuators B: Chemical. 2007;126(2):604-8.

70. McLintock IS, Ritchie M. Reactions on titanium dioxide; photo-adsorption and oxidation of ethylene and propylene. Transactions of the Faraday Society. 1965;61:1007-16.

71. O'Callaghan S, Galvin P, O'Mahony C, Moore Z, Derwin R. ‘Smart’wound dressings for advanced wound care: a review. Journal of Wound Care. 2020;29(7):394-406.

72. Hosseini ES, Dervin S, Ganguly P, Dahiya R. Biodegradable Materials for Sustainable Health Monitoring Devices. ACS Applied Bio Materials. 2020.

73. Yoon S-D, Kwon Y-S, Lee K-S. Biodegradation and biocompatibility of poly L-lactic acid implantable mesh. International neurourology journal. 2017;21(Suppl 1):S48.

74. Molina-Lopez F, Kinkeldei T, Briand D, Tröster G, De Rooij NF. Theoretical and experimental study of the bending influence on the capacitance of interdigitated micro-electrodes patterned on flexible substrates. Journal of Applied Physics. 2013;114(17):174907.

75. Bilic HG, Buyukoztekin T, Ozdemir S, editors. The use of chipless sensors with rfid for condition monitoring. 2018 International Conference on Artificial Intelligence and Data Processing (IDAP); 2018: IEEE.

76. Zhou X, He Y, Zeng J. Liquid metal antenna-based pressure sensor. Smart Materials and Structures. 2019;28(2):025019.

77. Wan G, Kang W, Wang C, Li W, Li M, Xie L, et al. Separating strain sensor based on dual-resonant circular patch antenna with chipless RFID tag. Smart Materials and Structures. 2020;30(1):015007.

78. Yi X, Cho C, Cooper J, Wang Y, Tentzeris MM, Leon RT. Passive wireless antenna sensor for strain and crack sensing—Electromagnetic modeling, simulation, and testing. Smart Materials and Structures. 2013;22(8):085009.

79. Nikbakhtnasrabadi F, El Matbouly H, Ntagios M, Dahiya R. Textile-Based Stretchable Microstrip Antenna with Intrinsic Strain Sensing. ACS Applied Electronic Materials. 2021;3(5):2233-46.

80. Vaudon P, Aubreton T, Dufrane P, Jecko B. Influence of the ground plane structure on the radiation pattern of microstrip antennas. Annales Des Télécommunications.

1993;48(5):319-29.

81. Tata U, Huang H, Carter R, Chiao J. Exploiting a patch antenna for strain measurements. Measurement Science and Technology. 2008;20(1):015201.

82. Zhu J, Fox JJ, Yi N, Cheng H. Structural Design for Stretchable Microstrip Antennas. ACS applied materials & interfaces. 2019;11(9):8867-77.

83. Saberkari A, Ziabakhsh S, Martinez H, Alarcón E. Active inductor-based tunable impedance matching network for RF power amplifier application. Integration. 2016;52:301-8.

84. Tentzeris MM, Nikolaou S, editors. RFID-enabled ultrasensitive wireless sensors utilizing inkjet-printed antennas and carbon nanotubes for gas detection applications. 2009 IEEE International Conference on Microwaves, Communications, Antennas and Electronics Systems; 2009: IEEE.

85. Lee H, Shaker G, Naishadham K, Song X, McKinley M, Wagner B, et al. Carbon-nanotube loaded antenna-based ammonia gas sensor. IEEE Transactions on Microwave Theory and Techniques. 2011;59(10):2665-73.

86. Maskey BB, Sun J, Shrestha K, Kim S, Park M, Kim Y, et al. A smart food label utilizing roll-to-roll gravure printed NFC antenna and thermistor to replace existing "use-by" date system. IEEE Sensors Journal. 2019;20(4):2106-16.

87. Manzari S, Caizzone S, Rubini C, Marrocco G, editors. Feasibility of wireless temperature sensing by passive UHF-RFID tags in ground satellite test beds. 2014 IEEE International Conference on Wireless for Space and Extreme Environments (WiSEE); 2014: IEEE.

88. Zannas K. Développement de capteurs RFID passifs dédiés au monitoring des groupes alternateurs: Université Grenoble Alpes (ComUE); 2019.

89. Roh JJ, Kunnathur A, Tarafdar M. Classification of RFID adoption: An expected benefits approach. Information & Management. 2009;46(6):357-63.

90. Dastoori K, Makin B, Bappoo S. The effectiveness of passive RFID Tags in the presence of charged particles. Journal of Electrostatics. 2009;67(2-3):468-72.

91. Chen Y-L, Liu D, Wang S, Li Y-F, Zhang X-S. Self-powered smart active RFID tag integrated with wearable hybrid nanogenerator. Nano Energy. 2019;64:103911.

92. Yoon W-J, Chung S-H, Park S-J. An Efficient Tag Sleep Method for Improving Tag Collection Performance in Active RFID Systems. The Journal of Korean Institute of Communications and Information Sciences. 2009;34(7B):686-93.

93. Wenyi C, Shuo G, Xiao W, Tingwen X, Jingtian X, Xi T, et al. Analysis and design of power efficient semi-passive RFID tag. Journal of Semiconductors. 2010;31(7):075013.

94. Escobedo P, Carvajal MA, Capitan-Vallvey LF, Fernandez-Salmeron J, Martinez-Olmos A, Palma AJ. Passive UHF RFID Tag for Multispectral Assessment. Sensors (Basel). 2016;16(7):1085.

95. Cao Z, Chen P, Ma Z, Li S, Gao X, Wu RX, et al. Near-Field Communication Sensors. Sensors (Basel). 2019;19(18):3947.

96. Escobedo P, Erenas MM, Martínez-Olmos A, Carvajal MA, Gonzalez-Chocano S, Capitán-Vallvey LF, et al. General-purpose passive wireless point–of–care platform based on smartphone. Biosensors and Bioelectronics. 2019;141:111360.

97. Dang W, Manjakkal L, Navaraj WT, Lorenzelli L, Vinciguerra V, Dahiya R.

Stretchable wireless system for sweat pH monitoring. Biosens Bioelectron. 2018;107:192-202.

98. Escobedo P, Erenas MM, Lopez-Ruiz N, Carvajal MA, Gonzalez-Chocano S, de Orbe-Paya I, et al. Flexible Passive near Field Communication Tag for Multigas Sensing. Anal Chem. 2017;89(3):1697-703.

99. Nguyen TB, Tran VT, Chung WY. Pressure Measurement-Based Method for Battery-Free Food Monitoring Powered by NFC Energy Harvesting. Sci Rep. 2019;9(1):17556.

100. Marsh P, Manjakkal L, Yang X, Huerta M, Le T, Thiel L, et al. Flexible Iridium Oxide based pH sensor Integrated with Inductively Coupled Wireless Transmission System for Wearable Applications. IEEE Sensors Journal. 2020:1-.

101. Rahul A, Rao S, Raghu M. Near field communication (NFC) technology: a survey. International Journal on Cybernetics & Informatics (IJCI). 2015;4(2):133.

102. Al-Ofeishat HA, Al Rababah MA. Near field communication (NFC). International Journal of Computer Science and Network Security (IJCSNS). 2012;12(2):93.

103. Preradovic S, Karmakar NC, editors. Design of fully printable planar chipless RFID transponder with 35-bit data capacity. 2009 European Microwave Conference (EuMC); 2009: IEEE.

104. Nijas C, Dinesh R, Deepak U, Rasheed A, Mridula S, Vasudevan K, et al. Chipless RFID tag using multiple microstrip open stub resonators. IEEE Transactions on Antennas and Propagation. 2012;60(9):4429-32.

105. El Matbouly H, Tedjini S, Zannas K, Duroc Y. Chipless sensing system compliant with the standard radio frequency regulations. IEEE Journal of Radio Frequency Identification. 2019;3(2):83-90.

106. Bianco GM, Occhiuzzi C, Panunzio N, Marrocco G. A Survey on Radio Frequency Identification as a Scalable Technology to Face Pandemics. IEEE Journal of Radio Frequency Identification. 2021.

107. Landaluce H, Arjona L, Perallos A, Falcone F, Angulo I, Muralter F. A review of IoT sensing applications and challenges using RFID and wireless sensor networks. Sensors. 2020;20(9):2495.

108. Occhiuzzi C, Caizzone S, Marrocco G. Passive UHF RFID antennas for sensing applications: Principles, methods, and classifcations. IEEE Antennas and Propagation Magazine. 2013;55(6):14-34.

109. Kim S, Kawahara Y, Georgiadis A, Collado A, Tentzeris MM. Low-Cost Inkjet-Printed Fully Passive RFID Tags for Calibration-Free Capacitive/Haptic Sensor Applications. IEEE Sensors Journal. 2015;15(6):3135-45.

110. Zannas K, El Matbouly H, Duroc Y, Tedjini S. Self-tuning RFID tag: A new approach for temperature sensing. IEEE Transactions on Microwave Theory and Techniques. 2018;66(12):5885-93.

111. Manzari S, Marrocco G. Modeling and applications of a chemical-loaded UHF RFID sensing antenna with tuning capability. IEEE transactions on antennas and propagation. 2013;62(1):94-101.

112. Vera GA, Duroc Y, Tedjini S. Third harmonic exploitation in passive UHF RFID. IEEE Transactions on Microwave Theory and Techniques. 2015;63(9):2991-3004.

113. Mazzaracchio V, Fiore L, Nappi S, Marrocco G, Arduini F. Medium-distance

affordable, flexible and wireless epidermal sensor for pH monitoring in sweat. Talanta. 2021;222:121502.

114. Fernández-Salmerón J, Rivadeneyra A, Martínez-Martí F, Capitán-Vallvey LF, Palma AJ, Carvajal MA. Passive UHF RFID tag with multiple sensing capabilities. Sensors. 2015;15(10):26769-82.

115. .

116. Sample A, Yeager D, Smith J, Powledge P, Mamishev A, editors. Energy harvesting in RFID systems. 2006 International Conference on Actual Problems of Electron Devices Engineering; 2006: IEEE.

117. Agrawal T, Biswas P. Energy consumption evaluation framework for passive RFID tag anti-collision algorithms. International Journal of Radio Frequency Identification Technology and Applications. 2014;4(3):229-43.

118. Abugabah A, Nizamuddin N, Abuqabbeh A. A review of challenges and barriers implementing RFID technology in the Healthcare sector. Procedia Computer Science. 2020;170:1003-10.

119. Zhang J, Tian GY, Marindra AM, Sunny AI, Zhao AB. A review of passive RFID tag antenna-based sensors and systems for structural health monitoring applications. Sensors. 2017;17(2):265.

120. Matta LL, Karuppuswami S, Chahal P, Alocilja EC. AuNP-RF sensor: An innovative application of RF technology for sensing pathogens electrically in liquids (SPEL) within the food supply chain. Biosensors and Bioelectronics. 2018;111:152-8.

121. Ghaani M, Cozzolino CA, Castelli G, Farris S. An overview of the intelligent packaging technologies in the food sector. Trends in Food Science & Technology. 2016;51:1-11.

122. Kumari L, Narsaiah K, Grewal M, Anurag R. Application of RFID in agri-food sector. Trends in Food Science & Technology. 2015;43(2):144-61.

123. Pérez-Aloe R, Valverde JM, Lara A, Castaño F, Carrillo JM, González J, et al. Use of RFID tags for data storage on quality control in cheese industries. Data Storage IntechOpen. 2010:213-26.

124. Schumacher I, Wollenstein J, Kalbitzer J, editors. Low-power UHF-RFID sensor tags for a complete monitoring and traceability of the cold chain. Smart SysTech 2012; European Conference on Smart Objects, Systems and Technologies; 2012: VDE.

125. Achouri K, Caloz C. Design, concepts, and applications of electromagnetic metasurfaces. Nanophotonics. 2018;7(6):1095-116.

126. Li A, Luo Z, Wakatsuchi H, Kim S, Sievenpiper DF. Nonlinear, active, and tunable metasurfaces for advanced electromagnetics applications. IEEE Access. 2017;5:27439-52.

127. Henthorn S, O'Farrell T, Ford KL, editors. Metasurface Direct Antenna Modulators in non-Line of Sight Channels for the Internet of Things. 2020 IEEE 31st Annual International Symposium on Personal, Indoor and Mobile Radio Communications; 2020: IEEE.

128. Memon MU, Salim A, Jeong H, Lim S. Metamaterial inspired radio frequency-based touchpad sensor system. IEEE Transactions on Instrumentation and Measurement. 2019;69(4):1344-52.

129. Pandit N, Jaiswal RK, Pathak NP. Plasmonic metamaterial-based label-free microfluidic microwave sensor for aqueous biological applications. IEEE Sensors Journal.

2020;20(18):10582-90.

130. Del Hougne P, Imani MF, Sleasman T, Gollub JN, Fink M, Lerosey G, et al. Dynamic metasurface aperture as smart around-the-corner motion detector. Scientific reports. 2018;8(1):1-10.

131. Tripathi P, Kumar P, Raj S, Tripathi S, Tripathi V, editors. ANN based design of SRR loaded patch antenna for non-invasive blood glucose monitoring. 2019 4th International Conference on Information Systems and Computer Networks (ISCON); 2019: IEEE.

132. Bahramipour SS, Afrooz K, Honari MM, Mirzavand R, Mousavi P. Gradient and huygens' metasurface design and analysis based on transmission line theory. IEEE Transactions on Antennas and Propagation. 2020;68(9):6752-63.

133. Caloz C, Itoh T, editors. Novel microwave devices and structures based on the transmission line approach of meta-materials. IEEE MTT-S International Microwave Symposium Digest, 2003; 2003: IEEE.

134. Schueler M, Mandel C, Puentes M, Jakoby R. Metamaterial inspired microwave sensors. IEEE Microwave Magazine. 2012;13(2):57-68.

135. Kim Y, Lim S. Low Loss Substrate-Integrated Waveguide Using 3D-Printed Non-Uniform Honeycomb-Shaped Material. IEEE ACCESS. 2020;8:191090-9.

136. Sanders D, Sampayan S, Caporaso G, Rhodes M, Watson J, Slenes K, et al., editors. Development of a low loss, high dielectric strength microwave substrate. Conference Record of the 2006 Twenty-Seventh International Power Modulator Symposium; 2006: IEEE.

137. Kim T, Lim H, Lee Y, Kim B-J. Synthesis of BaTiO 3 nanoparticles as shape modified filler for high dielectric constant ceramic–polymer composite. RSC Advances. 2020;10(49):29278-86.

138. Liu C, Liu L, Yang D, Zhang L. A dipolar silicone dielectric elastomer and its composite with barium titanate nanoparticles. Journal of Materials Science: Materials in Electronics. 2020;31(14):11411-24.

139. Jiang L, Wang Y, Wen S, Zhou Y, Ma J, Chen S, et al. Fabrication of dielectric elastomers with improved electromechanical properties using silicone rubber and walnut polyphenols modified dielectric particles. Materials & Design. 2020;192:108674.

140. Hong S, Kang SH, Kim Y, Jung CW. Transparent and flexible antenna for wearable glasses applications. IEEE Transactions on Antennas and Propagation. 2016;64(7):2797-804.

141. Paracha KN, Rahim SKA, Soh PJ, Khalily M. Wearable antennas: A review of materials, structures, and innovative features for autonomous communication and sensing. IEEE Access. 2019;7:56694-712.

142. Castro AT, Sharma SK. Inkjet-printed wideband circularly polarized microstrip patch array antenna on a PET film flexible substrate material. IEEE Antennas and Wireless Propagation Letters. 2017;17(1):176-9.

143. Marasco I, Niro G, Rizzi F, De Vittorio M, D'Orazio A, Grande M, editors. Design of a PEN-Based Flexible PIFA Antenna Operating in the sub-6GHz Band for 5G Applications. 2020 22nd International Conference on Transparent Optical Networks (ICTON); 2020: IEEE.

144. Koul SK, Karthikeya G, editors. Polycarbonate based flexible antennas for

mmWave 5G devices. 2019 IEEE Asia-Pacific Microwave Conference (APMC); 2019: IEEE.

145. Khaleel HR, Al-Rizzo HM, Rucker DG, Mohan S. A compact polyimide-based UWB antenna for flexible electronics. IEEE Antennas and Wireless Propagation Letters. 2012;11:564-7.

146. Lin L, Ma M, Zhang F, Liu F, Liu Z, Li Y. Fabrications and performance of wireless LC pressure sensors through LTCC technology. Sensors. 2018;18(2):340.

147. Chen Z, Xi J, Huang W, Yuen MM. Stretchable conductive elastomer for wireless wearable communication applications. Scientific reports. 2017;7(1):10958.

148. Rai T, Dantes P, Bahreyni B, Kim WS. A stretchable RF antenna with silver nanowires. IEEE Electron Device Letters. 2013;34(4):544-6.

149. Song L, Myers AC, Adams JJ, Zhu Y. Stretchable and reversibly deformable radio frequency antennas based on silver nanowires. ACS applied materials & interfaces. 2014;6(6):4248-53.

150. Rogers JA, Ghaffari R, Kim D-H. Stretchable Bioelectronics for Medical Devices and Systems: Springer; 2016.

151. Cheng S, Wu Z, Hallbjorner P, Hjort K, Rydberg A. Foldable and stretchable liquid metal planar inverted cone antenna. IEEE Transactions on antennas and propagation. 2009;57(12):3765-71.

152. So JH, Thelen J, Qusba A, Hayes GJ, Lazzi G, Dickey MD. Reversibly deformable and mechanically tunable fluidic antennas. Advanced Functional Materials. 2009;19(22):3632-7.

153. Dey A, Guldiken R, Mumcu G. Microfluidically reconfigured wideband frequency-tunable liquid-metal monopole antenna. IEEE Transactions on Antennas and Propagation. 2016;64(6):2572-6.

154. Wang C, Takei K, Takahashi T, Javey A. Carbon nanotube electronics–moving forward. Chemical Society Reviews. 2013;42(7):2592-609.

155. Atwa Y, Maheshwari N, Goldthorpe IA. Silver nanowire coated threads for electrically conductive textiles. Journal of Materials Chemistry C. 2015;3(16):3908-12.

156. Nuzzo RG. The future of electronics manufacturing is revealed in the fine print. Proceedings of the National Academy of Sciences. 2001;98(9):4827-9.

157. Seung HK, Heng P, Costas PG, Christine KL, Jean MJF, Dimos P. All-inkjet-printed flexible electronics fabrication on a polymer substrate by low-temperature high-resolution selective laser sintering of metal nanoparticles. Nanotechnology. 2007;18(34):345202.

158. Amendola S, Palombi A, Marrocco G. Inkjet printing of epidermal RFID antennas by self-sintering conductive ink. IEEE Transactions on Microwave Theory and Techniques. 2017;66(3):1561-9.

159. Mota C, Camarero-Espinosa S, Baker MB, Wieringa P, Moroni L. Bioprinting: from tissue and organ development to in vitro models. Chemical reviews. 2020;120(19):10547-607.

160. Finkenzeller K. RFID handbook: fundamentals and applications in contactless smart cards, radio frequency identification and near-field communication: John wiley & sons; 2010.

161. Greenhouse HM. Design of Planar Rectangular Microelectronic Inductors. Ieee T

Parts Hyb Pac. 1974;Ph10(2):101-9.

162. STMicroelectronics. How to design a 13.56 MHz customized tag antenna. AN2866 Application Note2009.

163. Escobedo P, Bhattacharjee M, Nikbakhtnasrabadi F, Dahiya R. Flexible Strain and Temperature Sensing NFC Tag for Smart Food Packaging Applications. IEEE Sensors Journal. 2021.

164. Bhattacharjee M, Escobedo P, Nikbakhtnasrabadi F, Dahiya R, editors. Printed Flexible Temperature Sensor with NFC Interface. 2020 IEEE International Conference on Flexible and Printable Sensors and Systems (FLEPS); 2020: IEEE.

165. Escobedo P, Bhattacharjee M, Nikbakhtnasrabadi F, Dahiya R, editors. Flexible strain sensor with NFC tag for food packaging. 2020 IEEE International Conference on Flexible and Printable Sensors and Systems (FLEPS); 2020: IEEE.

166. Escobedo P, Bhattacharjee M, Nikbakhtnasrabadi F, Dahiya R. Smart Bandage With Wireless Strain and Temperature Sensors and Batteryless NFC Tag. IEEE Internet of Things Journal. 2020;8(6):5093-100.

167. Escobedo P, Bhattacharjee M, Nikbakhtnasrabadi F, Dahiya R. Flexible Strain and Temperature Sensing NFC Tag for Smart Food Packaging Applications. IEEE Sensors Journal. 2021;21(23):26406-14.

168. Balliu E, Andersson H, Engholm M, Öhlund T, Nilsson H-E, Olin H. Selective laser sintering of inkjet-printed silver nanoparticle inks on paper substrates to achieve highly conductive patterns. Scientific reports. 2018;8(1):1-9.

169. Sima K, Syrovy T, Pretl S, Freisleben J, Cesek D, Hamacek A, editors. Flexible smart tag for cold chain temperature monitoring. 2017 40th International Spring Seminar on Electronics Technology (ISSE); 2017: IEEE.

170. Luo S, Bimbo J, Dahiya R, Liu H. Robotic tactile perception of object properties: A review. Mechatronics. 2017;48:54-67.

171. Manjakkal L, Pullanchiyodan A, Yogeswaran N, Hosseini ES, Dahiya R. A wearable supercapacitor based on conductive PEDOT: PSS - coated cloth and a sweat electrolyte. Advanced Materials. 2020;32(24):1907254.

172. Yamada T, Hayamizu Y, Yamamoto Y, Yomogida Y, Izadi-Najafabadi A, Futaba DN, et al. A stretchable carbon nanotube strain sensor for human-motion detection. Nat Nanotechnol. 2011;6(5):296-301.

173. Yamamoto A, Nakamoto H, Bessho Y, Watanabe Y, Oki Y, Ono K, et al. Monitoring respiratory rates with a wearable system using a stretchable strain sensor during moderate exercise. Med Biol Eng Comput. 2019;57(12):2741-56.

174. Christou A, Ntagios M, Hart A, Dahiya R. GlasVent—The Rapidly Deployable Emergency Ventilator. Global Challenges. 2020;4(12).

175. de Vargas-Sansalvador IMP, Erenas MM, Martínez-Olmos A, Mirza-Montoro F, Diamond D, Capitan-Vallvey LF. Smartphone based meat freshness detection. Talanta. 2020;216:120985.

176. Fletcher B, Mullane K, Platts P, Todd E, Power A, Roberts J, et al. Advances in meat spoilage detection: A short focus on rapid methods and technologies. CyTA-Journal of Food. 2018;16(1):1037-44.

177. Doyle MP. Compendium of the microbiological spoilage of foods and beverages:

Springer; 2009.

178. Brecht JK, Sargent SA, Brecht PE, Saenz J, Rodowick L. Protecting Perishable Foods During Transport by Truck and Rail: HS1328, 4/2019. EDIS. 2019;2019(2).

179. Vanderroost M, Ragaert P, Devlieghere F, De Meulenaer B. Intelligent food packaging: The next generation. Trends in food science & technology. 2014;39(1):47-62.

180. Escobedo P, Erenas M, Lopez-Ruiz N, Carvajal M, Gonzalez-Chocano S, de Orbe-Paya I, et al. Flexible passive near field communication tag for multigas sensing. Analytical chemistry. 2017;89(3):1697-703.

181. Lin R, Kim H-J, Achavananthadith S, Kurt SA, Tan SC, Yao H, et al. Wireless battery-free body sensor networks using near-field-enabled clothing. Nature communications. 2020;11(1):1-10.

182. Ke SH, Guo PW, Pang CY, Tian B, Luo CS, Zhu HP, et al. Screen‐Printed Flexible Strain Sensors with Ag Nanowires for Intelligent and Tamper‐Evident Packaging Applications. Advanced Materials Technologies. 2020;5(5):1901097.

183. Kuhn V, Lahuec C, Seguin F, Person C. A multi-band stacked RF energy harvester with RF-to-DC efficiency up to 84%. IEEE transactions on microwave theory and techniques. 2015;63(5):1768-78.

184. Stannard C, Williams A, Gibbs P. Temperature/growth relationships for psychrotrophic food-spoilage bacteria. Food Microbiology. 1985;2(2):115-22.

185. Sutono A, Heo D, Chen Y-JE, Laskar J. High-Q LTCC-based passive library for wireless system-on-package (SOP) module development. IEEE transactions on microwave theory and techniques. 2001;49(10):1715-24.

186. Núñez CG, Navaraj WT, Polat EO, Dahiya R. Energy‐autonomous, flexible, and transparent tactile skin. Advanced Functional Materials. 2017;27(18):1606287.

187. Cuong NT, Barrau S, Dufay M, Tabary N, Da Costa A, Ferri A, et al. On the nanoscale mapping of the mechanical and piezoelectric properties of poly (L-lactic acid) electrospun nanofibers. Applied Sciences. 2020;10(2):652.

188. Curry EJ, Ke K, Chorsi MT, Wrobel KS, Miller AN, Patel A, et al. Biodegradable piezoelectric force sensor. Proceedings of the National Academy of Sciences. 2018;115(5):909-14.

189. [07 Sep. 2021]. Available from: https://voyantic.com/products/tagformance-pro.

190. Nikbakhtnasrabadi F, Hosseini ES, Dahiya R, editors. Flexible Strain Sensor based on Printed LC Tank on Electrospun Piezoelectric Nanofibers. 2021 IEEE International Conference on Flexible and Printable Sensors and Systems (FLEPS); 2021: IEEE.

191. Deng W-J, Wang L-F, Dong L, Huang Q-A. LC wireless sensitive pressure sensors with microstructured PDMS dielectric layers for wound monitoring. IEEE Sensors Journal. 2018;18(12):4886-92.

192. Akar O, Akin T, Najafi K. A wireless batch sealed absolute capacitive pressure sensor. Sensors and Actuators A: Physical. 2001;95(1):29-38.

193. Yoon SG, Park BJ, Chang ST. Highly sensitive piezocapacitive sensor for detecting static and dynamic pressure using ion-gel thin films and conductive elastomeric composites. ACS applied materials & interfaces. 2017;9(41):36206-19.

194. Mikkonen R, Koivikko A, Vuorinen T, Sariola V, Mäntysalo M. Inkjet-printed, nanofiber-based soft capacitive pressure sensors for tactile sensing. IEEE Sensors Journal.

2021.

195. Yang X, Wang Y, Qing X. A flexible capacitive sensor based on the electrospun PVDF nanofiber membrane with carbon nanotubes. Sensors and Actuators A: Physical. 2019;299:111579.

196. Huang C, Leavitt T, Bayer LR, Orgill DP. Effect of negative pressure wound therapy on wound healing. Current problems in surgery. 2014;51(7):301-31.

197. Hafner J, Lüthi W, Hänssle H, Kammerlander G, Burg G. Instruction of compression therapy by means of interface pressure measurement. Dermatologic surgery. 2000;26(5):481-8.

198. Thomas S. The production and measurement of sub-bandage pressure: Laplace's Law revisited. Journal of wound care. 2014;23(5):234-46.

199. Bhattacharjee M, Soni M, Escobedo P, Dahiya R. PEDOT: PSS Microchannel‐Based Highly Sensitive Stretchable Strain Sensor. Advanced Electronic Materials. 2020;6(8):2000445.

200. Miyazaki H, Kinoshita M, Saito A, Fujie T, Kabata K, Hara E, et al. An ultrathin poly (l‐lactic acid) nanosheet as a burn wound dressing for protection against bacterial infection. Wound Repair and Regeneration. 2012;20(4):573-9.

201. Won Y, Kim A, Yang W, Jeong S, Moon J. A highly stretchable, helical copper nanowire conductor exhibiting a stretchability of 700%. NPG Asia Materials. 2014;6(9):e132.

202. Hester JG, Kim S, Bito J, Le T, Kimionis J, Revier D, et al. Additively manufactured nanotechnology and origami-enabled flexible microwave electronics. Proceedings of the IEEE. 2015;103(4):583-606.

203. Nauroze SA, Novelino L, Tentzeris MM, Paulino GH, editors. Inkjet-printed “4D” tunable spatial filters using on-demand foldable surfaces. 2017 IEEE MTT-S International Microwave Symposium (IMS); 2017: IEEE.

204. Saintsing CD, Cook BS, Tentzeris MM, editors. An origami inspired reconfigurable spiral antenna. ASME 2014 International Design Engineering Technical Conferences and Computers and Information in Engineering Conference; 2015: American Society of Mechanical Engineers Digital Collection.

205. Hussain AM, Ghaffar FA, Park SI, Rogers JA, Shamim A, Hussain MM. Metal/polymer based stretchable antenna for constant frequency far‐field communication in wearable electronics. Advanced Functional Materials. 2015;25(42):6565-75.

206. Dang W, Manjakkal L, Navaraj WT, Lorenzelli L, Vinciguerra V, Dahiya R. Stretchable wireless system for sweat pH monitoring. Biosensors and Bioelectronics. 2018;107:192-202.

207. Angeli MAC, Nikbakhtnasrabadi F, Vena P, Dahiya R, editors. Geometry dependent application of stretchable printed antenna. 2019 IEEE International Conference on Flexible and Printable Sensors and Systems (FLEPS); 2019: IEEE.

208. Dang W, Vinciguerra V, Lorenzelli L, Dahiya R. Printable stretchable interconnects. Flexible and Printed Electronics. 2017;2(1):013003.

209. Chang T, Tanabe Y, Wojcik CC, Barksdale AC, Doshay S, Dong Z, et al. A General Strategy for Stretchable Microwave Antenna Systems using Serpentine Mesh Layouts. Advanced Functional Materials. 2017;27(46):1703059.

210. Ofcom. Enabling wireless innovation through local licensing. Shared access to spectrum supporting mobile technology 2019 [Available from: https://www.ofcom.org.uk/__data/assets/pdf_file/0033/157884/enabling-wireless-innovation-through-local-licensing.pdf.

211. Johnson RC, Jasik H. Antenna engineering handbook. New York, McGraw-Hill Book Company, 1984, 1356 p No individual items are abstracted in this volume. 1984.

212. Jiang S, Newton E, Yuen C, Kan C. Chemical silver plating on cotton and polyester fabrics and its application on fabric design. Textile research journal. 2006;76(1):57-65.

213. Eom S, Lim S. Stretchable complementary split ring resonator (CSRR)-based radio frequency (RF) sensor for strain direction and level detection. Sensors. 2016;16(10):1667.

214. Chang T, Fan JA, Lee TH, editors. Evaluating the Microwave Performance of Epidermal Electronics with Equivalent Transmission Line Modeling. 2018 IEEE International Microwave Biomedical Conference (IMBioC); 2018: IEEE.

215. Núñez CG, Liu F, Navaraj WT, Christou A, Shakthivel D, Dahiya R. Heterogeneous integration of contact-printed semiconductor nanowires for high-performance devices on large areas. Microsystems & nanoengineering. 2018;4(1):1-15.

216. McCormick N, Lord J. Digital image correlation. Materials today. 2010;13(12):52-4.

217. Costantini R, Lennard F, Alsayednoor J, Harrison P. Investigating mechanical damage mechanisms of tapestries displayed at different angles using 2D DIC. The European Physical Journal Plus. 2020;135(6):1-17.

218. Alsayednoor J, Harrison P, Dobbie M, Costantini R, Lennard F. Evaluating the use of digital image correlation for strain measurement in historic tapestries using representative deformation fields. Strain. 2019;55(2):e12308.

219. Chang T, Tanabe Y, Wojcik CC, Barksdale AC, Doshay S, Dong Z, et al. A General Strategy for Stretchable Microwave Antenna Systems using Serpentine Mesh Layouts. Advanced Functional Materials. 2017;27(46):1703059.

220. Pozar DM. Microstrip antennas. Proceedings of the IEEE. 1992;80(1):79-91.

221. Shen S, Chiu C-Y, Murch RD. A dual-port triple-band L-probe microstrip patch rectenna for ambient RF energy harvesting. IEEE Antennas and Wireless Propagation Letters. 2017;16:3071-4.

222. Zhu J, Cheng H. Recent development of flexible and stretchable antennas for bio-integrated electronics. Sensors. 2018;18(12):4364.